Super-resolution mapping of receptor engagement during HIV entry

A dissertation submitted in partial fulfilment

of the requirements for the degree of

Doctor of Philosophy

Of

University College London

October 2021

Yue Yuan

MRC Laboratory for Molecular Cell Biology

and

BBSRC London Interdisciplinary Biosciences PhD Consortium
(LIDo)

University College London

Declaration

I, Yue Yuan, confirm that the work presented in this thesis is my own. Where information has been derived from other sources, I confirm that this has been indicated in the thesis.

Yue Yuan

October 2021

Abstract

The plasma membrane (PM) serves as a major interface between the cell and extracellular stimuli. Studies indicate that the spatial organisation and dynamics of receptors correlate with the regulation of cellular responses. However, the nanoscale spatial organisation of specific receptor molecules on the surface of cells is not well understood primarily because these spatial events are beyond the resolving power of available tools. With the development in super-resolution microscopy and quantitative analysis approaches, it optimally poises me to address some of these questions.

The human immunodeficiency virus type-1 (HIV-1) entry process is an ideal model for studying the functional correlation of the spatial organisation of receptors. The molecular interactions between HIV envelope glycoprotein (Env) and key receptors, CD4 and co-receptor CCR5/CXCR4, on the PM of target cells have been well characterised. However, the spatial organisation that receptors undergo upon HIV-1 binding remains unclear.

In this project, I established a Single Molecule Localisation Microscopy (SMLM) based visualisation and quantitative analysis pipeline to characterise CD4 membrane organisation in CD4$^+$ T cells, the main host cell target for HIV-1 infection. I found that prior to HIV engagement, CD4 and CCR5 molecules are organised in small distinct clusters across the PM. Upon HIV-1 engagement, I observed dynamic congregation and subsequent dispersal of virus-associated CD4 clusters within 10min. I further incorporated statistical modelling to show that this reorganisation is not random.

This thesis provides one of the first nanoscale imaging and quantitative pipelines for visualising and quantifying membrane receptors. I showed that this quantitative approach provides a robust methodology for understanding the recruitment of HIV-1 receptors before the formation of a fusion pore. This methodology can be applied to the analyses of the nanoscale organisation of PM receptors to link the spatial organisation to function.

Impact Statement

The HIV-1 pandemic has had a significant impact on human health and economy. The most advanced stage of HIV infection, acquired immune deficiency syndrome (AIDS), remains one of the leading causes of death worldwide. The development of HIV highly active antiretroviral therapy (HAART) has been the most impressive scientific advance in HIV research. However, the poor availability of HAART in developing countries and the current failure for effective vaccines development has hindered control of the HIV pandemic. Attempts to understand HIV-host cell fusion, one of the first steps in HIV infection, may provide new opportunities for intervention to aid the fight against HIV.

This project contributes impact in many ways. It first provides a nanoscale visualisation and quantitative analysis pipeline to study virus-receptor engagement and receptor spatial organisation in general. It is a pipeline with customisable capability that is easily accessible for other researchers. To demonstrate its efficacy, I used it to characterise HIV-CD4 engagement and furthered our understanding of this process. The insights have implications for the membrane fusion of other viruses, such as SARS-CoV-2.

This work has already had a significant impact in academia. A manuscript detailing the analytical pipeline and discovery of CD4 clustering at 1min post-HIV binding was first released on *bioRxiv* in early 2021, which sparked discussion on Twitter with over 50 retweets. In addition, a manuscript entitled 'Single-Molecule Super-Resolution Imaging of T-Cell Plasma Membrane CD4 Redistribution upon HIV-1 Binding' was published in *Viruses* (doi:10.3390/v13010142) in January, 2021; this paper has been downloaded >1500 times.

In establishing the visualisation methodology, the know-how I gained in sample preparation contributed to a review entitled 'Between Life and death: strategies to reduce phototoxicity in super-resolution microscopy'

([doi:10.1088/1361-6463/ab6b95](doi:10.1088/1361-6463/ab6b95)) published in February, 2020 in the Journal of Physics D: Applied Physics. This review has been cited 20 times to date with >4500 downloads.

In the future, I expect this work will lead to further impact on receptor nanoscale spatial organisation studies in general. The pipeline will continue to be used in Marsh and Henriques labs to investigate HIV entry, with the characterisation of CD4/CCR5 organisation during HIV binding presenting new research avenues. I also anticipate that the application of the methodology described in this thesis will be used to bring new understanding of the biology underlying the functions of other cell surface molecules.

Acknowledgements

I don't think I can adequately thank all the people involved in the course of my PhD, but here I go,

Firstly, thank you to my supervisors, Ricardo and Mark. To Ricardo, the support, guidance and training that I have received from you are immeasurable. Thanks for believing in me even when I said 'I knew nothing about SR imaging, I just found your work so cool', the first time we chatted. Thank you for always being supportive and encouraging, especially in the disappointments. You might never know how thankful I am for the 'shall we chat in 10min?' email that comes every time without fail when I feel overwhelmed and 'screamed' at you in emails. Mark, thank you so much for stimulating discussion about this project, for inspiring me to try new possibilities in the project and for catching and explaining the mistakes I made in English. Thanks for challenging me to push myself.

Thank you to all the members from both Henriques lab and Marsh lab. Pedro, you introduced Elyra to me, although I still have a love-hate relationship with 'her'. Thanks for your endless help, your smile, words of encouragement. Caron, without you, the project might not even exist. Thanks for being always so understanding. The inter-continental paper writing marathon with you is one of the highlights of my PhD. Thanks for making it so enjoyable. Romain, thanks so much for being so generous with your time. Thanks for challenging me to expand the analysis pipeline and to sit side by side with me for hours during late nights to go through data and modify codes. Thanks for reminding me of the excitement of science with sparkles in your eye full of passion for science every time experiments roasted me. To Scott, thank you for all the experimental support and the lunch chats. Thanks for tirelessly reviewing every document I need to submit throughout my PhD. Farrell, thanks for all the constructs and experimental chats. Siân, thank you for constantly checking in on me and reassuring me that I can do it. Kalina, Laure and Naureen, thank

9

you so much for your company during all the ups and downs. You are always there whenever I need a rant, whether it is in the lab, TC room, or microscopy room.

Thanks to my thesis committee, Sophie, Jason, Julie and Joe. Thanks for all the constructive feedback and valuable guidance throughout the project. Without you, the project would not take shape in such a short time.

Thanks to everyone in LIDo for making it a vibrant and fun environment. Nadine, thanks for always being so responsive and understanding. Thank you for making it such a healthy and supportive community; I know I can fall back on LIDo whenever I feel stuck. Farhan, thanks for sorting out PIPS paperwork for me and checking in on me throughout the way. Laura and Marta, I can't imagine finishing my PhD thesis without you; thanks for the walks, food and virtual study room.

The LMCB and POG BSL3 lab has been an excellent and inclusive environment to work. Ki, thanks for always coming down within 10min after receiving my 'help' message in the microscopy room. Clare, thanks for making the returning to BSL3 after the pandemic so smooth and organised. Heena and Julio, thank you for making the refreshing induction to BSL3 so insightful. Thank you for always keeping an eye on the 'high-maintenance' autoclave.

Thanks to Liang for always cheering me on, for all your help, for being there for me. I don't think I can do this without you. Thank you for everything. Thanks to all my friends outside science, thank you for the dinners, the laughter, the weekend walks and the gin.

Finally, and most importantly, thank you to all my family and especially to my parents Li and Ying, without whom I honestly could and would not have contemplated this PhD. Thank you for your love and unconditional support. Thanks for always being there for me and cheering me on, even from far away when we have only seen each other 2 times in person during my whole PhD. 我爱你们！

Acknowledgements of work done

All work in this thesis was carried out by myself, Y Yuan with the exception of the following:

Chapter 3:

- Section 3.2.8 was carried out by Dr Caron Jacobs, University of Cape Town.
- The code used in Section 3.2.9 was provided by Dr Isabel Llorente Garcia, Department of Physics and Astronomy, UCL.

Chapter 4:

- The code used in Section 4.2.6 was provided by Dr Isabel Llorente Garcia, Department of Physics and Astronomy, UCL.

Table of Content

List of Figures

List of Tables

List of Abbreviations

(4α-) PMA	(4α-) Phorbol-12-myristate13-acetate
ACE2	Angiotensin converting enzyme 2
AIDS	Acquired immune deficiency syndrome
CBC	Coordinate-based colocalisation
CFM	Conventional fluorescence microscopy
CT	Cytoplasmic tail
DBSCAN	Density-based spatial clustering of applications with noise
DHPR	Dihydropyridine receptor
EM	Electron microscopy
EMCCD	Electron multiplying charge coupled device
Env	Envelope glycoprotein
FOV	Field of view
FWHM	Full-width half maximum
GA	Glutaraldehyde

GPI-APs	Glycosylphosphatidylinositol-anchored proteins
HAART	Highly active antiretroviral therapy
HEK	Human embryonic kidney
HIV-1	Human immunodeficiency virus type-1
hpi	Hours post-infection
HR	Heptad repeat
IC	Infected cells
IS	Immunological synapse
MOI	Multiplicity of infection
N&B	Number & brightness
NA	Numerical Aperture
NNA	Nearest neighbour analysis
PALM	Photoactivated localisation microscopy
PBSC	Photobleaching step counting
PCF	Pair-correlation function
PEM	Cytoskeleton-preserving buffer

PFA	Paraformaldehyde
PLL	Poly-L-lysine
PM	Plasma membrane
qPAINT	(Quantitative) Point accumulation in nanoscale topology
qSMLM	(Quantitative) Single molecule localisation microscopy
ROI	Regions of interest
RPMI	Roswell park memorial institute
RyR2	Ryanodine receptor 2
SD	Standard deviation
SEM	Standard error of the mean
SIM	Structured illumination microscopy
SMAC	Supramacromolecular activation cnetres
SMLM	Single molecule localisation microscopy
SRM	Super-resolution microscopy
STED	Stimulated emission depletion
TAS	Temperature arrested state

TCR	T cell receptor
TIRFM	Total internal reflection fluorescence microscopy
TMD	Transmembrane domain
TMPRSS2	Transmembrane protease serine 2
ToMATo	Topological mode analysis tool

Chapter 1 Introduction

1.1 Plasma membrane organisation

1.1.1 The plasma membrane structure

The plasma membrane (PM) acts as a cell's primary interface with surrounding cells and extracellular stimuli and serves as a communicator while projecting the cell's state to the intracellular compartments [1]. It also poses a barrier to intracellular pathogens, such as viruses. Membranes provide essential docks for protein localisation [1–3]. Nevertheless, the presence of proteins on the PM alone is not always sufficient for their function. Meanwhile, the nanoscopic localisation, oligomerisation and/or clustering of membrane proteins can affect the efficiency of cellular processes [4–6]. Therefore, it is important to understand the molecular details of the membrane structure and mechanisms corresponding to dynamic organisations of proteins. In this section, I will summarise PM properties and models of membrane organisation and dynamics.

The basis of PM is a lipid bilayer, a lamellar structure with a hydrophobic core and a polar headgroup region on both sides [7]. Cholesterol is the most abundant lipid in PM and comprises up to 40% of its total lipid constitution [8]. Meanwhile, proteins constitute around half of the total plasma membrane mass [9], these membrane proteins can anchorage into either a lipid bilayer via transmembrane domains or a lipid moiety, or as membrane associated proteins, which may associate with the membrane via electrostatic interactions with lipid headgroups, a variety of protein-protein or protein-glycan interactions [10]. Extracellular compartment of these lipids and proteins are mostly glycosylated and glycans form a dense structure at the outer surface of the PM [11]. These molecular complexity of PM is proposed to serve as a selective barrier and organising centre with a high fidelity and robustness [4].

1.1.2 Plasma membrane lateral organisation models

In this section, the models that intend to describe PM organisation will be discussed. It is worth noting that there is no universal mechanism underlying the organisation of the PM. Evidence suggests that several components of the PM are highly interconnected and can occur spontaneously or sequentially during signalling transduction [7]. A combination of these models is potentially the best to describe the organisation of molecules on the PM at a full spectrum.

1.1.2.1 Fluid Mosaic Model

The Fluid Mosaic Model [12] has for many years provided the most widely accepted model for understanding PM structure, protein organisation, and signal transduction. In this model, fluidity is one of the most critical membrane features, which forms the basis for the highly dynamic character of membrane-associated processes. Membrane fluidity allows the majority of molecules to diffuse freely over long distance within the PM [12]. The word 'mosaic' in the model was used primarily to accentuate the heterogeneity of membrane components, including the coexistence of diverse lipids and proteins. Although membranes are fluid, they obtain a higher rigidity than the cytosol, its membrane fluidity can further be modified by lipid composition or other factors [13], such as the presence of protein or change in temperature. In addition, the presence of integral membrane proteins further increases the local viscosity in their surrounding environment, which reduces the mobility of membrane constituents in general [14–17]. An increase in lipid-lipid and lipid-protein interactions, or heterogeneities, can further contribute to a reduction in mobility. Therefore, changes in intrinsic properties, especially viscosity, can be attributed to the reduction in long-range diffusion for lipids and proteins in PM.

1.1.2.2 Hydrodynamic model

Hydrodynamic model was primarily used to define the mobility of transmembrane proteins and their aggregates in PM [18]. This model proposes that molecular diffusion rates are highly dependent on membrane thickness

and viscosity. The size of proteins and aggregates has little impact on the diffusion rate. Obviously, it applies only for freely moving molecules with no interactive objects and do not co-diffuse as a single entity. Another limitation of this model is that it ignores the density of objects and their lipid environment. Therefore, the application of hydrodynamic model is not ideal to be used as a general model of the PM organisation, considering the heterogeneity of cell membranes. Nevertheless, it can be a useful alternative to describe local changes such as those in the nanoscale.

1.1.2.3 Mattress model

The hydrophobic thickness of a lipid bilayer is defined by the length and saturation of acyl chains and the presence of sterols. Lipids in the bilayer interact with transmembrane domains of integral proteins in a non-specific and transient manner [19]. The mismatch between hydrophobic thickness and the hydrophobic length of transmembrane domains is referred to as hydrophobic mismatch. In the mattress model, a hydrophobic mismatch was proposed to induce the formation of lipid/protein aggregation in PM [20–22]. However, whether hydrophobic mismatch contributes to nanoscale organisation of the plasma membrane in living cells has yet to be experimentally proven, primarily due to the lack of approaches that reach the desired spatial and temporal resolution [7].

1.1.2.4 Self-assemblies of lipids and lipid ordered domains

With the observation of protein clusters [23], lipid segregations [24] and heterogeneous distribution of certain lipids and proteins between apical and basal membranes [25], it is proposed that lipids and their self-assemblies can determine the fate of newly synthesised/recycled membrane molecules [26]. Simons and Ikonen described this model by defining 'lipid rafts' as platforms on the PM for signalling proteins to selectively interact with effector molecules [27]. This platform is predominantly small (10-200 nm) [28] and contains high molecular order enriched in cholesterol and sphingolipids. Meanwhile,

detergent treatment experiments revealed that not all membrane proteins and lipids are soluble in mild detergents, referring to these lipid-ordered domains also as detergent resistant domains. However, the existence of spontaneously formed lipid raft/detergent resistant domains in living cells remains controversial [29–33]. Certain lipids alone (such as gangliosides) were found to self-aggregate and form fluid nanoclusters both *in silico*, in model membranes, and in living cells [34–37] (Figure 1.2).
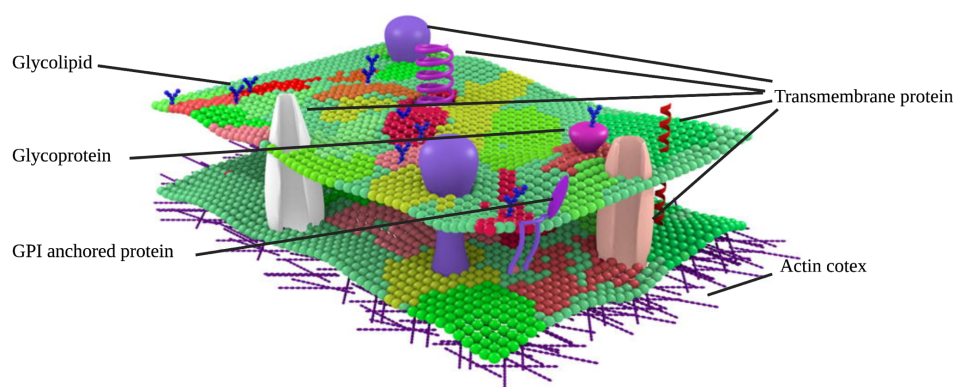
Figure 1.1 The PM fluid mosaic model.

Schematic of the fluid mosaic model as an asymmetric phospholipid bilayer with associated transmembrane and peripheral proteins. Lipid, transmembrane proteins and membrane-associated proteins can be organised into microcompartments with dense actin cortex nearby. Adapted from [38].

1.1.2.5 Cortical actin skeleton and nanoclusters

The cortical actin skeleton positions in the proximal regions of the membrane and is directly associated with PM via actin-binding proteins or signaling complexes. The close association makes it the structure to impact the mobility of plasma membrane molecules and their lateral organisation. The effect of the actin skeleton on membrane molecules has been demonstrated in many studies (For example [39–41]).

Nanoclusters of membrane proteins interacting with lipids or/and actin skeleton have emerged as a dominant theme in the lateral organisation of membranes on the sub 100nm length scale. Plausible proposals exist regarding the functional significance of such clusters, especially during immune responses [42], EGF signalling [43] and Ras signalling [44]. Glycosyl phosphatidylinositol-anchored proteins (GPI-APs) are a broad group of lipid linked proteins that often see in these protein nanoclusters [45,46]. Therefore, it is proposed that lipid-protein interactions might contribute to the formation of these nanoclusters [47]. In addition, Gowrishankar group suggested that F-actin asters located beneath the PM also drive lipid-anchored proteins into nanoclusters [48]. Nevertheless, the nature of the *in vivo* coupling between inner leaflet and actin, including possible adaptor proteins, remains to be studied [38] (Figure 1.2).

Such fluctuations in membrane domains potentially contribute to the overall heterogeneity of the PM and restricted certain lipids and proteins within small nanodomains. However, this model remains difficult to elucidate because of the spatial and temporal resolution required to disclose information at the molecular scale.
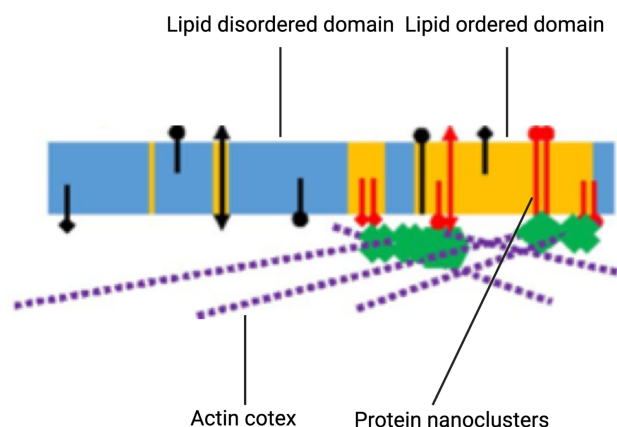
Figure 1.2 Schematics of PM lipid ordered domains, cortical actin skeleton, and protein nanoclusters

Lipid ordered domains enrich in saturated phospholipids, sphingolipids, glycolipids, cholesterol, lipidated proteins and GPI-anchored proteins.

Enrichment of these hydrophobic components endows these lipid domains with distinct physical properties. Adapted from [49]

1.1.3 Regulation of lateral mobility in the PM

1.1.3.1.1 The picket fence model and hop diffusion

The picket fence model has been the most prominent explanations for the regulation of molecules dynamic in the PM. The picket fence model explains the restriction of transmembrane proteins into membrane compartments [50]. Whereby transmembrane proteins directly or indirectly linked to the actin cortex, act as anchors. These anchored proteins also act as a physical barrier, hindering the diffusion of phospholipids, transmembrane proteins, and membrane proteins [51] (Figure 1.3).

The 'fence' was hypothesised to cover the entire cell surface with a network of corrals. Electron microscopy observed that apparent corrals(fence) bounded by cytoskeletal filaments had a size distribution similar to that determined by single particle tracking studies [50,52]. Within the corrals, diffusion (measured at submillisecond time scales) was measured to be ultrafast, approaching or even exceeding values for membrane proteins and lipids in pure bilayers. In comparison, diffusion over a larger spatiotemporal scale ('hop diffusion', from a few tens to over a hundred nm and to tens of milliseconds) was about 20-fold slower due to the fence barriers [47].

Taking into account that lipids also show hop diffusion [53], the model further stated that a subpopulation of transmembrane proteins is attached to the membrane skeleton fence and formed 'pickets'. While picket proteins potentially bind to lipid, the fluidity of the inter-picket space would be less than other parts of the membrane, which further contributes to the barrier function [47].

Recent studies on transmembrane protein have provided further insight for this model. Using Quantum dot tracking, the Sadegh group showed that the

potassium channel is obstructed by interactions with the subjacent and compartmentalised actin cytoskeleton [54]. In the confined compartment trajectories, diffusate was observed to hop to an adjacent compartment visualised by Photoactivation localisation microscopy [54]. Furthermore, actin disruption did not affect corral size; rather, it increased hop rate [55].
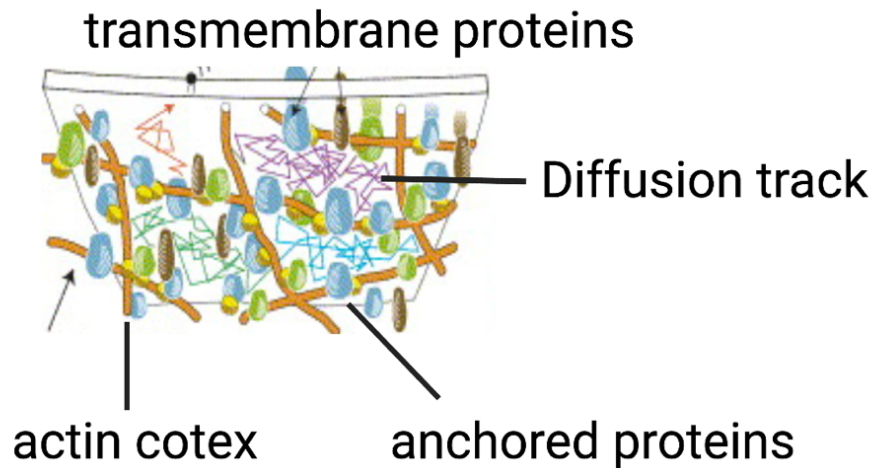
Figure 1.3 Schematics of the picket fence model

In the Picket-fence model, transmembrane proteins that bind the actin cortex restrict the movement of other membrane-associated proteins, transmembrane proteins, and lipids. Lines indicates the diffusion track. Adapted from [56]

1.1.3.1.2 Transient anchorage

The lateral diffusion of complexed in the PM maybe transiently immobilised, likely to be prepared for a signal transduction event. Suzuki's group observed that a small degree of clustering (<10 molecules) of the outer leaflet GPI-AP CD59 induces a transient association with the inner leaflet Lyn kinase. Giα2 also briefly associates with the cluster and further activates Lyn and a simulation-induced temporary arrest of lateral diffusion event, whereby the cluster is transiently immobilised [33]. This event thereafter leads to calcium signalling [57].

1.1.3.1.3 Channelled diffusion

Diffusing molecules undergo one-dimensional diffusion retained by parallel barriers [58]. Under single-molecule tracking, there has been seen that a fraction of CD36 population was potentially channelled by microtubules proximate to the inner leaflet of the PM [59].

1.1.3.1.4 Directed movement

Directed lateral movement appears to be a more efficient way than lateral diffusion. An example of rapid directed movement is the movement of T cell receptor (TCR) during T cell activation. After T cells recognise foreign peptides displayed by major histocompatibility complexes on the antigen presenting cells, the T cell receptor moves rapidly towards the centre of the immune synapse, directed along microtubule tracks, and driven by the microtubule motor, dynein [60]. However, it is unclear how rapid directed movement occur with the presence of the underlying membrane skeleton fence.

1.1.4 T cell activation: an example of nanoscale organisational dynamics of PM proteins and their functional correlation

To gain further insight into the interplay between compartmentalisation of signalling components, local signalling activity, and molecular recruitment, imaging techniques with high spatial resolution. To combine super-resolution microscopy with quantitative readouts function is useful in advancing the understanding how signalling molecule organisation at the nanoscale correlates with cellular functions. The T cell activation process is one of the leading examples in which such studies have been advanced using these techniques.

The initial contact between T cell and antigen-presenting cell evolves to a stable interaction that can last from minutes to hours, termed immunological synapse (IS) formation. The IS is a typical example of molecule spatial

organisational changes and its functional correlation. The most commonly studied bull's eye-like structure IS is formed between CD4+ T cells interacting with lymphoma B cells or cytotoxic T cells, consisting of three concentrically arranged rings (supramacromolecular activation centres (SMACs)). The cSMAC is located in the center of SMAC, surrounded by pSMAC and the dSMAC, in the distal area of the synapse [61]. The dSMAC develops from an actin ring that first expands and later retracts as a nonmuscular myosin IIA dependent process [62–64].

Signaling molecules are sorted into different SMAC regions during the IS maturation process. After initial triggering, TCRs at the PM travel laterally across the membrane and aggregate, forming multiple nanoclusters [65]. These nanoclusters are commonly surrounded by an LFA-1 ring to form more stable synapses. Since then, TCR clusters move from the periphery to the centre of the newly formed IS while CD45 is excluded from TCR nanoclusters and segregates to pSMAC [66,67]. Translocation of TCR nanoclusters to cSMAC along with signaling proteins, such as CD3, CD4, and CD28, was interpreted as a way of accumulating signaling in the central area [68] (Figure 1.4).

| Expansion | Contraction | Immunologicall synapse |

TCR-CD28 nanocluster   TCR-CD28 nanocluster
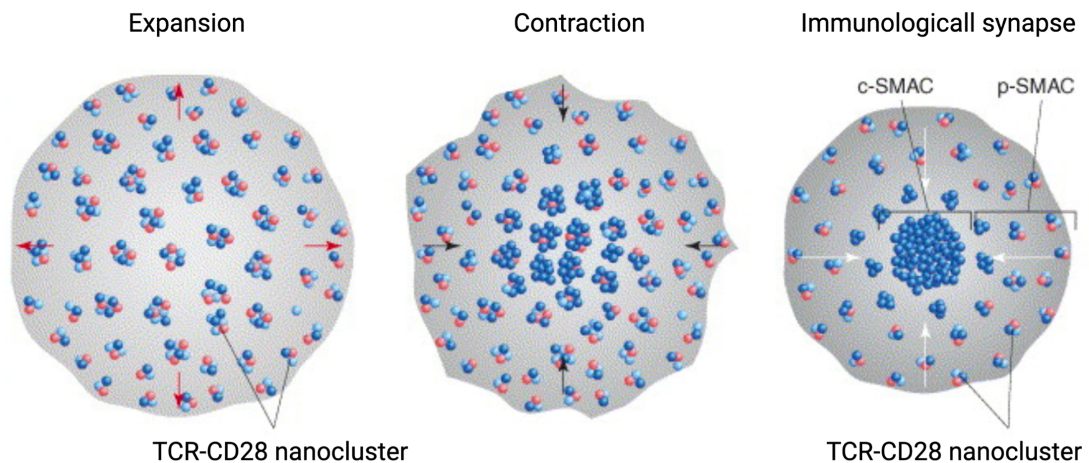
Figure 1.4 Schematics of nanocluster dynamics and IS formation in T cells

After the initial contact between the T cell and the antigen presenting cell, the T cell spread on the bilayer accompanied by TCR-CD28 kinase-adaptor

nanoclusters. Upon full spreading, the T cell begin to contract and TCR-CD28-kinases-adaptors nanoclusters accumulate at the central region of the interface. Meanwhile, TCR-CD28 nanoclusters merged with surrounding complexes to form larger clusters while disassociated with kinases and adaptors. TCRs further accumulate at the cSMAC and CD45 and other signalling molecules move to the pSMAC region. Adapted from [69].

The organisation of other molecules including ZAP-70, Grb2, and SLP-76 in nanoclusters has also been studied [70–75]. During T cell activation, ZAP-70 is mixed uniformly with TCR but only partially with LAT. A later study showed that the LAT-SLP nanostructure forms during the actin expansion stage [76]. LAT clusters recruit Grb2 regardless of LAT cluster size, indicating that even small nanoclusters contain phosphorylated LAT and participate in T cell activation. In the SLP-76 and LAT clusters, LAT tends to be in the centre, while SLP-76 is surrounded on the outside [73].

More recent studies in live T cells using advanced imaging techniques have examined the organisation of TCR clusters and their kinetics upon T cell activation [77]. Authors distinguished two segregated domains within TCR clusters. TCR and ZAP-70 colocalised in the 'receptor domain' while LAT with its associated adaptor protein (Grb2, GADS and SLP-76) and signalling proteins (ADAP, NCK, etc) to form the 'signalling domain'. It is further showed that LAT was located adjacent to, rather than colocalised to the receptor domain. Similarly, adaptor and signalling proteins colocalised with each other but segregated from the receptor domain.

1.2 Super-resolution microscopy: a tool to quantitatively understand cellular organisation at the nanoscale

Conventional fluorescence microscopy (CFM) is an invaluable tool in cell and molecular biology studies. Although CFM allows non-invasive visualisation of

specific proteins and multiple types of proteins in specimens, the limited spatial resolution hinders the ability to accurately discriminate molecular species at the nanoscale. In the context of this thesis, research on PM receptor organisation and ligand engagement has been restricted as they interact within a subdiffraction size.

Optical and mathematical characterisation of CFM resolution was first calculated by Ernst Abbe [78,79]. The resolution of a fluorescence microscope system is defined as the minimum observable separation between two objects (Δd). It is formulated as $\Delta d = \lambda/2NA$ (λ represents the wavelength of the emitted fluorescence; NA represents the numerical aperture of the objective). The Rayleigh criterion defines the optical resolution as the minimal distance between two point sources of light that could still be distinguished as separate objects [80]. Generally, the resolution can be estimated by half the wavelength of the emitting fluorescence used [81]. For CFM imaging with visible wavelengths, the optimal lateral diffraction-limited resolution is ~200-300 nm, and the axial resolution is worse, ranging ~500-800 nm [82,83].

By contrast, electron microscopy (EM) irradiates samples with a beam of electrons instead of illuminating samples with visible light. The wavelength of an electron beam is much smaller than that of photons; thereby, a resolution of ~0.1 nm can be achieved [84]. However, EM generally requires a sophisticated imaging setup and loses the labelling specificity and sensitivity of fluorescence microscopy and the live cell compatibility. Therefore, an optical imaging technique with nanoscale resolution offers significant advantages in studying the interactions between molecular species. Super-resolution microscopy (SRM) has emerged to fulfil this need and bridged molecule nanoscale organisation, quantitative characterisation, and cellular biology studies.

1.2.1 Super-resolution microscopy and SMLM

The mainstream SRM methods available include Structured Illumination Microscopy (SIM), Stimulated Emission Depletion (STED), and Single Molecule Localisation Microscopy (SMLM). Each of these techniques use different methods for overcoming the diffraction limit, thereby, has inherent advantages and limitations to consider when applying to different biological systems.

1.2.1.1 SIM and STED microscopy

To overcome the diffraction limit, SIM [85] utilises a structured pattern of illumination light to excite the whole field. When a grid with high spatial frequency is projected onto a simple, it blurs fluorophore emission. An interference pattern named a moiré fringe is produced by mixing the excitation pattern with the spatial pattern of the sample. Several images were taken with different orientations of the grid. Subdiffraction-limited structure information can be resolved by analysing the signal variations. SIM allows resolutions of around 100 nm in *x*, *y* and *z* [86].

The physical basis for STED microscopy is to generate an illumination beam with an effective diameter that is smaller than the diffraction limit [87]. This technique uses the conventional focused laser beam to stimulate an area of fluorescent molecules that covers hundreds of nanometers in diameter. Meanwhile, a second doughnut-shaped beam illuminates the sample, depleting the emission of the fluorophore outside the central region. The second depletion beam forces probed molecules from their excited electronic state back to their ground state, therefore, only photons from molecules within the centre of the doughnut shape are collected. When the two beams are overlapped, a subset of fluorophores is switched off and a smaller exciting focal spot is generated, resulting in higher resolution. This technique requires laser powers around 1000 times higher than used in CFM. Although, theoretically, there is no resolution limit to STED images. Practically,

photodamage caused to biological samples by high laser intensities usually sets the intensity limit on the depletion beam during biological application [88].

1.2.1.2 SMLM technique

SMLM involves Stochastic Optical Reconstruction Microscopy (STORM), utilises fluorophores as visualisation agency [89], and Photoactivated Localisation Microscopy (PALM), to visualise fluorescent protein tagged molecules [90]. The principle of SMLM is to manipulate the activation state of labelling fluorophores to switch between fluorescent and 'dark' states with high-intensity laser illumination and controlled chemical conditions, a process called photoswitching or 'blinking'.

In this case, instead of fluorophores all emitting in a single frame as in CFM, images are acquired from sequential frames, each containing a small number of transiently emitting fluorophores that are then localised to a point source. By acquiring a series of many thousands of frames, most fluorophores can be accurately localised. An SR image can then be reconstructed from these accurately measured molecule coordinates, with resolutions typically down to ~20 nm [87] (Figure 1.2).
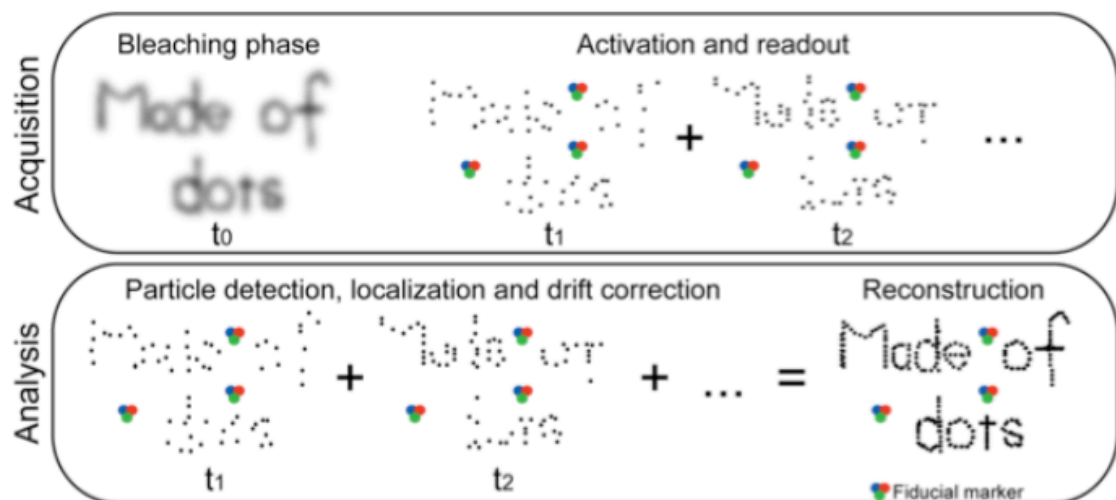
Figure 1.2 Representation of the STORM imaging process.

Unlike imaging using a CFM, in which all fluorophores are excited altogether, STORM imaging acquires a sequence of images in which only a small subset of spatially spaced fluorophores is switched on at each frame. The first frames will have a high amount of naturally active photoswitchable fluorophores. Therefore, a bleaching step (t_0) is performed, followed by the sequential acquisition (Acquisition $t_1+t_2+\ldots$).fT These frames are then analysed using localisation algorithms, which results in accurate fluorophore detection and localisation (Analysis $t_1+t_2+\ldots$). Finally, after drift and chromatic shift correction (the latter for multi-colour acquisitions), an SR reconstruction is obtained from all the localisations (Analysis Reconstruction). Adapted from [91].

1.2.1.3 Comparison among SIM, STED, and SMLM

1.2.1.3.1 Acquisition Speed

SMLM techniques show one of the most pronounced trade-off between speed and resolution. This is because two molecules cannot be turned on within the same PSF at any given time, thereby thousands of rounds of acquisition are essential to generate a high-quality super-resolution picture. As such, live-cell imaging is largely impossible with SMLM techniques.

The speed of SIM is also limited by the need of recording multiple frames with oriented grids to generate a super-resolved image. However, physical improvement accelerated the movement of grating itself, achieving live-SIM [92].

1.2.1.3.2 Fluorescent Probes

SIM is the only super-resolution method that no special fluorescent probes are required. The same fluorescent proteins, antibodies, and probes used in CFM are applicable to the technique. Considering most commercially available systems, not all conventional fluorophores are applicable in STED. Thereby, multi-colour imaging is hard to achieve due to the restrictions of applicable probes [88]. SMLM requires photoswitchable proteins and probes, which must

be as bright as possible to acquire a high contrast ratio between the on and off states.

1.2.1.3.3 Spatial resolution

SIM offers the least improvement in spatial resolution among all the super-resolution techniques [86]. For STED, the practical achievable resolution is strongly dependent on the photostability of a sample, generally achieving 50-100 nm without sample damage [88]. For SMLM, an SR image can achieve a resolution typically down to ~20 nm [87].

Overall, SMLM provides a higher resolution image of the molecule organisation and detailed information on localisation coordinates, photon count, and signal-to-noise ratio of every individual point localisation mapped by the technique. Furthermore, by incorporating statistical analysis into the acquired information in SMLM, in-depth quantitative analysis can be done on nanoscale specimens of interest, such as characterising the size of clusters, the number of molecules, etc. These advantages make SMLM stand out from other SRM techniques in quantitatively studying nanoscale protein-receptor interactions.

1.2.2 Using Total internal reflection fluorescence microscopy (TIRFM) to study protein organisation on the PM

TIRFM is an optical technique that constrains the excitation of fluorophores to an extremely thin optical section (~200nm) at the surface of the coverslip [93,94]. The method generates an evanescent wave in the liquid at the solid-liquid interface when excitation light is internally reflected from a transparent solid (e.g., coverslip). The intensity of the evanescent wave exponentially decays away from the solid [95]. In this case, only fluorescent molecules within ~200 nm are efficiently excited, making it an effective tool for studying membrane proteins [43,96–98] (Figure 1.3). Combining TIRF and STORM to obtain nanoscale resolution information on a molecule of interest within 200nm of the plasma

membrane allows for in-depth statistical analysis of the PM receptor organisation at the near-single molecule level [99].
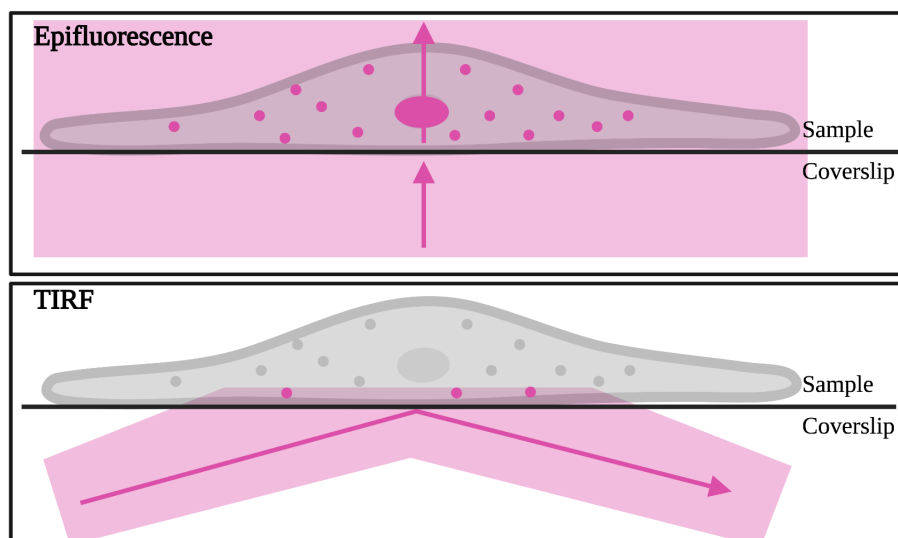
Figure 1.3 Schematics of Epifluorescence and TIRF microscopy.

In epifluorescence microscopy, the light beam excites all fluorescent molecules in a sample. In TIRF microscopy, the light beam is reflected from the coverslip, resulting in evanescent wave illuminates only fluorochromes in a thin optical section close to the coverslip and eliminating out-of-focus background fluorescence.

1.2.3 SR cluster analysis approaches

Approaches based on spatial statistics are well suited to analysing data generated from SMLM and reveal information on the nanoscale spatial organisation of specific molecules. Broadly, three types of clustering analysis methods can be applied to SMLM data analysis, including correlation-based, threshold-based, and geometric-based approaches [100].

1.2.3.1 Correlation-based analysis

Correlation-based analysis provides a global description of the organisation in SMLM data, including nearest neighbour analysis (NNA) [101], Ripley's function [102–104] and Pair-correlation function (PCF) [105–107]. NNA calculates the distance

between target localisation and its nearest neighbour. This distance is compared to that of a completely random distribution of all the localisations. The discrepancies between measured distance and distance obtained from random distribution indicate clustering or dispersion within the data. NNA has previously been used to investigate the syntaxin distribution in the PM [108]. This study revealed that syntaxin 1 is organised as both small and large clusters; in the small clusters, molecule density decreases from the cluster core to the periphery, while in the large clusters, several density gradients are detected, indicating that these clusters may form by the merging of small clusters [108].

Ripley's function detects the number of neighbouring localisations within a pre-defined search radius around a single localisation (Figure 1.4). Within the analysis circle, the searching radius increases while the molecules are counted again. The number of neighbours is then compared with what would be expected in a random distribution. Deviation from randomness indicates clustering or dispersion. Unlike NNA, which looks at the distance from each point to its closest neighbour, Ripley's K investigates deviations from an expected random distribution along a gradient of small to large spatial scales, given a global description of cluster sizes. Ripley's function is widely used to study protein organisation in T cell immune synapses. For example, Ripley's analysis showed that T cell signalling adaptor protein, Lat, and a T cell kinase, p56[Lck], are clustered on the T cell membrane [74,109]. Upon T cell activation, p56[Lck] engages and clusters with TCR [74].

For PCF, instead of using a circle centred on each point, PCF uses a ring structure (Figure 1.4). During analysis, the width of the rings is fixed but the radius increases. As a result, the number of neighbours in the experimental data is compared with a completely spatially random distribution for defining cluster and dispersion. PCF provides higher sensitivity in detecting changes in localisation organisation than Ripley's function. However, the results from PCF can be noisier than Ripley's function, as fewer localisations are counted at each radius step. PCF was first applied to SMLM data to characterise the reorganisation of glycosylphosphatidylinositol (GPI) anchored proteins in PM

[105]. PCF has also been used in study T cell immune synapses. For example, one study found that TCR and a phosphatase, CD45, organised as separate clusters about 50-100 nm apart in untreated T cells. With cell spreading following TCR engaging with antigen-presenting cells and TCR activation, the distance between CD45 and TCR increased to ~230 nm and was enriched at high local curvature membrane, indicating that CD45 segregates from TCR at tight contacts [110].

The above methods provide a global description of the molecular organisation from SMLM data. These functions are most informative when clustering is uniform and homogeneous (i.e. clusters have similar size and densities) [111]. However, the sensitivity of these methods is largely dependent on the availability of an accurate *priori* model for cluster shape [112]. Furthermore, it is impossible to identify and segment clustered localisations and is unsuitable for extracting information at the single cluster level.
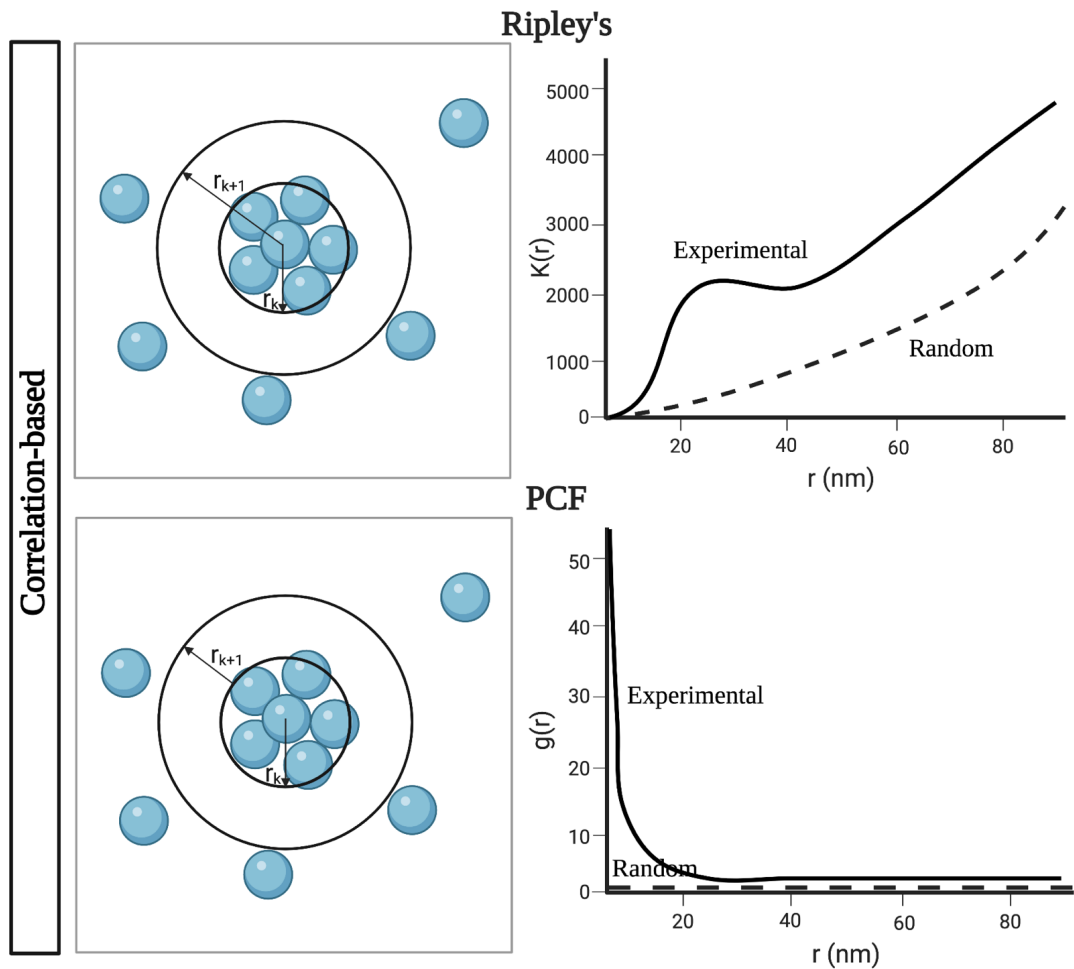
Figure 1.4 The principle of Ripley's function and PCF analysis.

In Ripley's function algorithm (left), the number of neighbouring localisations (blue) within a specified search radius (r_k, inner black ring) is counted. This radius is then increased (r_{k+1}, outer black ring), and the number of localisations is counted again until the maximal radius is reached. Ripley's algorithm (right), the estimated number is plotted (black line) and compared with entirely spatially random data (black dashed). PCF algorithm (left), rings of fixed r are used as searching regions. The inner diameter of the ring increases by r for each search step. PCF algorithm (right), the counted number is plotted (black line) and compared with the random distribution (black dashed).

1.2.3.2 Threshold-based analysis

Threshold-based analysis allows the organisation of molecules to be characterised at a single cluster level. Density-based spatial clustering of applications with noise (DBSCAN) is a well-established cluster analysis approach applied to SMLM data [113] (Figure 1.5). DBSCAN analysis requires two inputs: the radius of search (r) and the minimum number of points to determine a cluster (minPts). It takes the coordinates of the molecule and classifies them on the basis of its minPts within r. If a localisation satisfies the minPts within r, it is considered to be organised within a cluster. If a localisation does not meet the minPts but has cluster points within r, it is categorised as an edge point. Localisations that do not have minPts surrounded and do not have other coordinates within r are classified as noise (Figure 1.5). DBSCAN-based analysis has been used to define how TCR organisation impacts T cell signalling during immune synapse formation and T cell activation [114,115]. This method has been further extended to study the interaction of CD3 and phosphorylated CD3 by characterising the spatial colocalisation of these two types of proteins during T cell activation [114,115].

A limitation of DBSCAN based analysis has been observed in Mollazade *et al.* It was found that DBSCAN struggles to segment clusters separated by ~20nm, the limit of the data precision [112]. However, it performs well when clusters are spaced =/> 50 nm apart [112]. The practical application of DBSCAN to SMLM data can be challenging because the analysis sensitivity strongly depends on the choice of user-defined parameters [111,116,117]. Therefore, model-based approaches have been developed to select optimal parameters by testing and scoring an extensive range of r and minPts in the same experimental setting [118,119].

An alternative threshold-based analysis is ToMATo (topological mode analysis tool) [120]. ToMATo connects localisations to their neighbour with the highest density. By iterating the connecting process throughout all localisations with decreasing density, localisations are connected to individual candidate

clusters, further merged based on the persistence across different density scales. ToMATo showed better performance when distinguishing close clusters (~60nm separation) [120,121].

1.2.3.3 Geometric-based analysis

Geometric-based analysis can also be applied to SMLM data, such as Delaunay triangulation or Voronoï tessellation. A triangulated/tessellated surface is where geometric shapes are generated from localisations acquired in SMLM (Figure 1.5). In Delaunay triangulation, localisations make up the corners of triangular tiles. For Voronoï tessellation, molecule positions mark the centre of the geometric shapes with the edges drawn from the equidistant bisectors between points. In both cases, the clustered regions are determined by the features of geometric shapes. For example, smaller shapes represent regions with denser localisations, i.e. clusters (Figure 1.5). However, Voronoi tessellation methods are different from the Delaunay triangulation regarding the former's ability to provide a direct estimation of the region of influence, therefore, is preferable for analysing SMLM data [122,123]. Moreover, the Voronoï-based method are able to emit edge effect as the border molecules have infinite areas preventing them from contributing to the clustering [122,123].

Delaunay triangulation is implemented in segmenting DNA nucleoids clustering in mitochondrial cristae [124]. Open-source algorithms incorporating Voronoï tessellation, such as ClusterVisu [125] and SR-Tessler [126], are available to analyse SMLM data quantitatively. SR-Tessler was used to probe the distribution of the ryanodine receptor 2 (RyR2) and dihydropyridine receptor (DHPR) in cardiac myocytes [127]. It found that RyR1 and DHPR clusters decrease in density in pressure-overload cardiac hypertrophy [127].
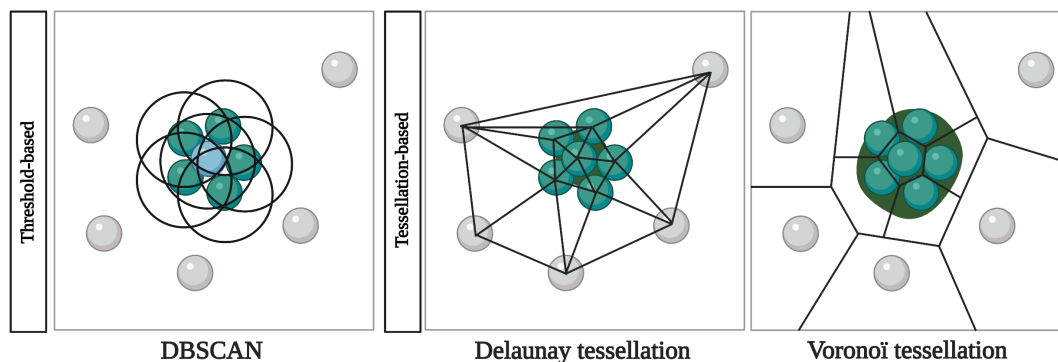
Figure 1.5 The principle of DBSCAN and geometric-based cluster analysis.

DBSCAN searches the area around the target localisation (blue), with the defined search radius r and a minimum number of neighbours (minPts). Localisations don't have surrounded minPts but within the search r is defined as edges (green). Localisations don't have sufficient minPts and are outside searching r are defined as edge point (grey). Delaunay triangulation and Voronoï tessellation represent the schematics of triangulation, and tessellation correspond to the localisations. Clustered points (green) are presented in the region with denser geometric shapes compared to the noise points (grey).

1.2.4 Molecular counting

Besides spatial features, the copy number of a protein in a complex is also a key quantifiable parameter that aids functional analysis. Before super-resolution methods became available, fluorescence intensity quantification methods were widely implemented for quantifying labelled molecules from CFM [128]. It is a straightforward estimation for the number of fluorochromes generated by comparing the intensity of targeted complexes with a unitary fluorescence intensity [129–131]. This section will focus on an overview of molecular counting methods and their application to SMLM.

1.2.4.1 Photobleaching step counting (PBSC)

A single decrease in the intensity trace indicates the photobleaching of a single fluorescent label. Counting the number of bleached molecules in a complex during continuous illumination can estimate the number of fluorophores in a complex [132]. The challenge of this method is to reliably distinguish between actual photobleaching and noise from transient fluorescence. The PBSC method requires an optimal signal-to-noise ratio and restricts the counting to complexes with a low number of subunits (typically <10) [133]. An excessive number will be recorded when the noise ratio increases. Increasing the number of labelled molecules also levels up the likelihood of mis-recording bleaching events. Recently, Bayesian algorithms [134–136] and deep learning-based approaches [137] have been developed to count more photobleaching events (>50) and improve the PBSC further. With open-source algorithms available, this method is relatively easy to implement with a high-quality single-molecule microscope setup. However, it destroys the fluorescent labels and prevents their application to time-resolved studies.

1.2.4.2 Quantitative single-molecule localisation microscopy (qSMLM)

Reconstructed data from SMLM yields a coordinates table of all detected localisations. However, the translation between localisations and the number of subunits per complex remains challenging due to the complex behaviour of fluorophores. For example, individual labels may undergo more than one switching cycle (multi-blinking) and result in over-counting. By contrast, not activated labels or nearby labels simultaneously activated within a diffraction-limited volume will not be registered as localisations, leading to under-counting [138].

The general strategy for dealing with over-counting is to perform a calibration experiment. This calibration experiment is to extract the average number of localisations detected per blinking event. The most widely used method for calibrating *in vitro* is to immobilise organic fluorophores (used in STORM) or

fluorescent proteins (used in PALM) and characterise their photoswitching behaviors [139,140]. It is crucial to perform calibration experiments in the same cellular microenvironment because otherwise the photophysic of the fluorophore might change [133]. A particularly versatile target of *in vitro* calibration is DNA nanostructures, also called DNA origami [141,142]. This DNA scaffold is highly customisable and can be used to immobilise predefined numbers of fluorophores. DNA origami is constructed with a single GFP with reference number of fluorophores of choice to number of target proteins [143]. A GFP antibody and AlexaFluor 647 labelled secondary antibody are used for calibration. The blinking statistics corresponding to the pre-defined number of target proteins are characterised and modelled [143]. After calibration, the number of localisations detected can be referenced as the number of fluorophores. Authors has tested this method on the nuclear pore complex subunit Nup133 and Nup107 fused to GFP, In calibrated data, the maximum and mean stoichiometry is consistent with the expected stoichiometry [144].

SMLM-based quantification can tolerate higher densities within investigated complexes and provide contextual information. The counting range, in the meantime, appears to be unrestricted when enough time is given for imaging fluorophores. However, the number of molecules obtained still need to be considered as estimates.

1.2.4.3 Quantitative point accumulation in nanoscale topology (qPAINT)

Point accumulation in nanoscale topology (PAINT) is an SMLM variant that exploits transient binding of dye-labelled probes to achieve blinking [145]. It circumvents stochastic photoswitching and resistance to photobleaching by using an unlimited source of free-floating probes. The DNA-PAINT technique adopted this principle through dye-labelled 'imager' strands and complementary target-bound 'docking' strands [146]. Quantitative PAINT (qPAINT) achieves molecular counting through analysis of the predictable DNA binding kinetics [147]. qPAINT counts the number of 'docking' strands, equals to the number of binding sites. DNA hybridisation and disassociation

can be precisely modelled through association and dissociation rate. Therefore, the binding frequency in the intensity time trace can be obtained through the calculatable factors, the rate constants, 'imager' strand concentration and the number of binding sites. qPAINT decouples molecular counting from calibration and photobleaching. However, the increase in accuracy comes at the cost of drastically increased imaging time. Moreover, like other SMLM approaches, it remains live-cell incompatible.

1.2.5 Quantitative colocalisation analysis

A close localisation between two molecules within a cell is generally interpreted as a suggestion for their functional correlation. Suppose that two interacting molecules are most likely to be within the resolution limit, thereby localised within the same pixels. In that case, the colocalisation can be quantified by computing the correlation coefficients (such as Manders and Spearman's coefficients) based on the pixel intensity [121]. However, with an increase in resolution in SMLM, it is almost impossible for two molecules to occupy the same position. Therefore, instead of pixel-based analysis, several coordinate-based techniques and a tessellation-based method have been implemented in quantitative colocalisation analysis for SMLM data.

1.2.5.1 Coordinate-based techniques

Lagache et al. have combined Ripley's function [102] and nearest neighbour-based analysis; the distance between two molecules most likely to be interacting is computed to characterise the average degree of colocalisation between two labelled species [148,149]. The combined univariate and bivariate Getis and Franklin's local point pattern analysis [150] and the coordinate-based colocalisation (CBC) [151] has been implemented into colocalisation characterisation [152]. With a user-defined searching radius, the number of species A and B is counted, and the level of colocalisation around each detected localisation is calculated via Getis and Franklin's function or the Spearman rank correlation, respectively. Generally, assigned colocalisation

scores range from -1 (dispersion) via 0 (randomly distributed) to 1 (colocalisation). CBC is later combined with DBSCAN to calculate the level of colocalisation at an individual cluster level [115]. These methods appear to be robust for determining the local molecular density. Furthermore, incorporating cluster analysis methods with colocalisation analysis allows for a detailed output of spatial and quantitative features for each channel and enriches the biological interpretations. However, the accuracy depends largely on finely tuned model-dependent parameters.

1.2.5.2 Tessellation-based approach

A tessellation-based approach can be applied to colocalisation analysis in SMLM [153], namely Coloc-Tesseler. Based on the orthogonal density of individual channels after tessellation, localisations can be categorised as 2 high-density classes (one for each channel) and 1 background class. Then, considering both channels, localisations in the 2 high-density classes are regrouped and segmented into two additional categories for each channel, such as orthogons in channel A that colocalise with channel B also in high-density types, orthogons in channel A in high-density classes that do not colocalise with channel B. This method has been extended to do 3D SMLM colocalisation analysis. It is also straightforward to use as it is parameter-free Spearman's rank correlation analysis. However, the lack of interplay between SR-Tesseler and Coloc-Tesseler partly restricts its ability to characterise quantitative features in spatially correlated localisations, such as cluster size and shape changes in both colocalised and non-colocalised areas.

1.3 How SRM advanced studies on HIV fusion and what is still missing?

The viral life cycle requires several steps to fulfil the synthesis of new viral particles. The viral particle that resides in the environment interacts with target cells by receptor-ligand interaction, followed by the internalisation of the virus

to replicate the genetic material and transcribe into viral proteins. Newly produced viral particles are then assembled using the machinery of the host cell. Understanding each step in detail helps to develop antivirals and channels to control pandemics [154]. Because of the subdiffraction size, viruses are ideal candidates for super-resolution studies. Among viruses, HIV is to date the most SR studied virus. This is primarily due to the fact that decades of studies provide us with a detailed understanding of HIV replication cycle [155]. In turn, this supplies guidance and well characterised toolbox for the design of SRM studies to fill the knowledge gap. In this chapter, I will first focus on summarise the findings of SRM-based HIV-1 on the process of HIV fusion, and what remains to be learned. Further detailed discussion will then be given on the HIV entry process with an emphasis on the HIV envelope protein and the CD4 receptor.

1.3.1 Brief overview of HIV

There are two main types of the HIV retrovirus, HIV-1 and HIV-2, and further divided into distinct subtypes [156]. Among those, HIV-1 group M is the most widely spread and infectious strain responsible for the widespread AIDS pandemic [156,157]. In the following discussion, I will focus on HIV-1.

HIV-1 belongs to the genus Lentivirus in the retroviridae family [158]. A complete HIV-1 virus particle is a spherical particle (~120 nm in diameter), comprised of two copies of single stranded RNA genome, packaged inside the core capsid structure. This core capsid is surrounded by the matrix protein p17 and the outermost envelope proteins (Env).

Based on the chemokine receptor required, HIV-1s are grouped into R5-tropism and X4-tropism, according to their coreceptor CCR5 and CXCR4 usage. R5-tropism dominates the early stages of infections regardless of the transmission routes (sexual, vertical, or parenteral) [159]. On the contrary, progression from the asymptomatic stages of HIV infection to AIDS is

associated with a change in viral coreceptor use from CCR5 to CXCR4 in more than 50% of patients [160].

Briefly, there are seven stages of the HIV-1 infection cycle, a. virus attachment, initial adhesion tends to be nonspecific and receptor independent. Although this nonspecific binding appears not to be essential for infection, it has been suggested that this initial adhesion brings Env molecules closer to the CD4 receptor and the CCR5 or CXCR4 [161], initiating receptor engagement. B. membrane fusion, after interaction between Env and receptors on the host cell membrane, the HIV-1 membrane fuse with the host cell membrane to enter and release HIV-1 RNA and enzymes. C. reverse transcription from RNA to DNA. D. Integration, viral DNA integrates into host cell genetic material. E. Replication, viral DNA is replicated to generate building blocks for virion formation. F. Assembly, viral components form immature virus particles using newly synthesised HIV-1 RNA. G. Budding, assembled immature virus from host cell buds from host cell and generate mature virions [157,162]. In a later section, I will focus on the HIV-1 fusion process.

1.3.2 Env structure and conformational dynamics of Env on the viral membrane

The HIV-1 membrane contains high levels of sphingolipids and cholesterol, similar to lipid ordered domains but different from host cell membranes [163]. Env glycoproteins are located in the virion membrane. 7-14 copies of the trimeric Env are incorporated into the viral membrane [164–166]. Looking at Env organisation on the viral membrane, previous EM study displayed an irregular Env distribution on mature virus surface [166]. Further STED microscopy experiments imaged the Env distribution on an individual virus particle level. Images showed consistent result that mature HIV-1 particles contains Env clusters [167].

The Env proteins, gp120 and gp41, are key for receptor CD4/coreceptor CCR5/CXCR4 interaction on the target cell membrane and for entry of HIV

(Figure 1.6 B and C). The transmembrane protein gp41 anchors Env to the HIV-1 membrane, while the surface glycoprotein gp120 is exposed on the outer surface of the HIV-1 membrane [168].

The gp120 monomer contains five conserved domains (C1-C5) and five variable surface-displayed loops, V1-V5. These surface loops are crucial for receptor and coreceptor binding [169]. Except for V5, the other variable surface loops are stabilised by disulphide bonds at their base. There are 3 domains in the gp41 glycoprotein, an ectodomain, a transmembrane domain (TMD) and a cytoplasmic tail (CT). The ectodomain contains two heptad repeats (N-HR and C-HR) that fold back to form a six-helix bundle during fusion [170–172]. The atomic structure of TMD assembles a lipid bilayer [173] and TMD forms a well-ordered trimer that protects three conserved arginines in the middle of the membrane, indicating its critical role in Env stability (Figure 1.7).

The Env trimer on the surface of HIV-1 is structurally flexible, transiting from closed, open, and intermediate conformations [174]. Pre-fusion Env trimers are thought to be in the close conformations to bury the fusion peptide at the interface between gp41 and gp120, allowing HIV-1 to evade the host cells [175,169]. Upon Env binds to CD4, the closed structure transits towards an open conformation that exposes the co-receptor binding site [176–181]. However, unliganded Env trimers can also spontaneously transition between these three conformations [174].
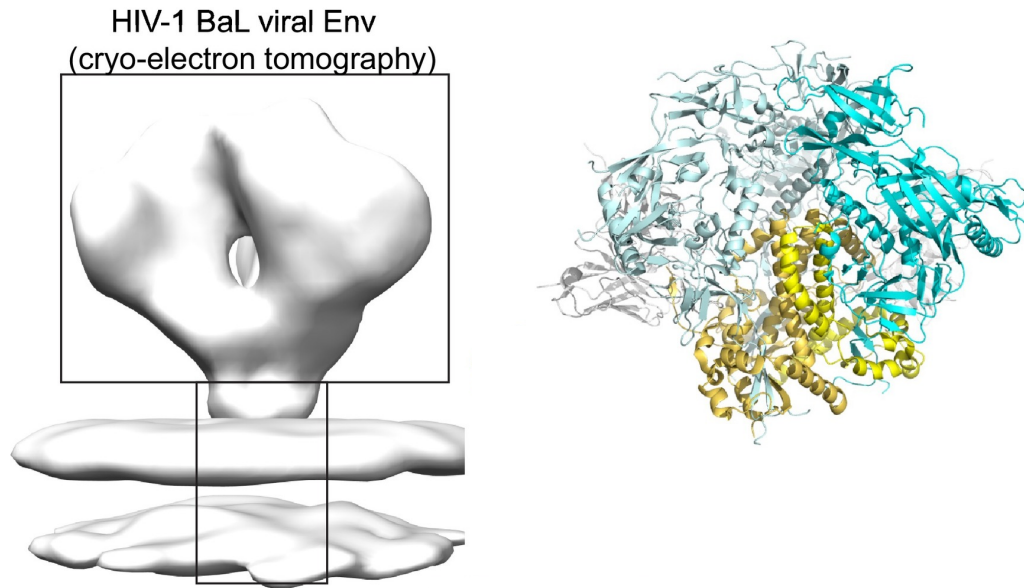
Figure 1.7 Structures of Env.

Left: Cryo-electron tomography reconstruction of HIV-1 Env spike on the surface of the virion (EMDB ID: EMD-5019 (Env portion); EMD-5022 (membrane portion)). Right: The single particle cry-EM structure of HIV-1 JR-FL Env without CT (pdb ID:5FUU [182]). Cyan: gp120, yellow:gp41.

1.3.3 HIV-1 receptor: CD4 structure and organisation

CD4, a member of the immunoglobulin superfamily, is a 51.1kDa cell surface transmembrane glycoprotein. CD4 is primarily expressed on subsets of immune cells, such as CD4+ T cells, macrophages, and microglia. Measuring by FACS, on untreated primary CD4+ T cells express 5-7 x 10^4 CD4 molecules per cell [183,184]. However, the number varies in T cell lines; for example, SupT1, a lymphoblastic lymphoma cell line used in this study, expresses approximately 1.2x10^5 molecules per cell [183].

1.3.3.1 CD4 structure

CD4 is a type 1 integral membrane protein; it contains an extracellular domain, a transmembrane domain, and a highly positively charged cytoplasmic tail with a Src kinase p56Lck-binding domain. The extracellular domain comprises four

immunoglobulin-like domains (D1-D4) [185], in which D1 contains the HIV Env gp120 binding site [186–189]. Based on the crystal structure, D1 and D2 are joined to D3 and D4 via a hinge region [190] (Figure 1.8).
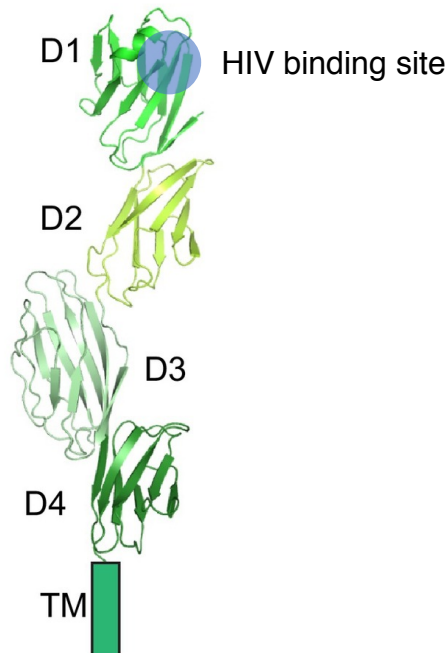
Figure 1.8 Crystal structure of soluble 4 domains CD4.

D1-D4 and the location of the transmembrane segment are indicated (pdb ID: 1WIO; [182]).

1.3.3.2 CD4 organisation

Most CD4 molecules are present on the PM of lymphoid cells [191]. In untreated T cells, the organisation of CD4 was seen as nanoclusters with a diameter of 200-500 nm in radius [192]. CD4 is enriched in the lipid ordered domains of plasma membrane [193–195]. Several studies revealed that CD4 exists as various naturally occurring oligomeric states, which display distinct functions in the binding of Env gp120 and the binding of TCR [196–200]. Through redox-dependent isomerisation on the CD4 D2 disulfide, CD4 can exist as an oxidised or reduced monomer or as a disulfide-linked dimer on the PM [201]. The organisational changes of CD4 are functionally significant. The cleavage of the D2 disulfide bond is likely to be involved in the conformational change

during HIV entry [199]. Using mutated CD4 and biochemical assays, studies suggested that reduced monomeric CD4 is the favourable form for gp120 binding, while dimeric CD4 is preferable for antigen-presenting cell binding [199]. Meanwhile, gp120 fails to bind oxidised CD4 monomer [200].

1.3.4 HIV membrane fusion

1.3.4.1 Structural study of HIV-1 membrane fusion

Env interacts with key cell surface receptors is one of the first steps in HIV-1 fusion. The CD4 binding site on gp120 is at the interface between the inner and outer domain [185,202]. This gp120-CD4 interaction stabilises an open quaternary conformation in gp120 V1/V2 and forms a 4-stranded β-sheet to bridge V1, V2 and V3 [181,202,203]. This 4-stranded β-sheet allows the open conformation V3 loop to further interact with a coreceptor, CCR5 or CXCR4. This induces further conformational changes that expose the gp41 fusion peptide. The gp41 fusion peptide then inserts into the target cell membrane and the N-HR and C-HR of gp41 form a 6-helix bundle by folding in the hinge region [204,205]. Formation of the 6-helix bundle pulls together the viral and host cell membranes, which leads to reorganisation of the lipid bilayers to form a fusion pore for delivering the viral core into the host cytoplasm [206] (Figure 1.6).

I. gp120-CD4 binding   II. gp41 insertion   III. 6-helix bundle formation
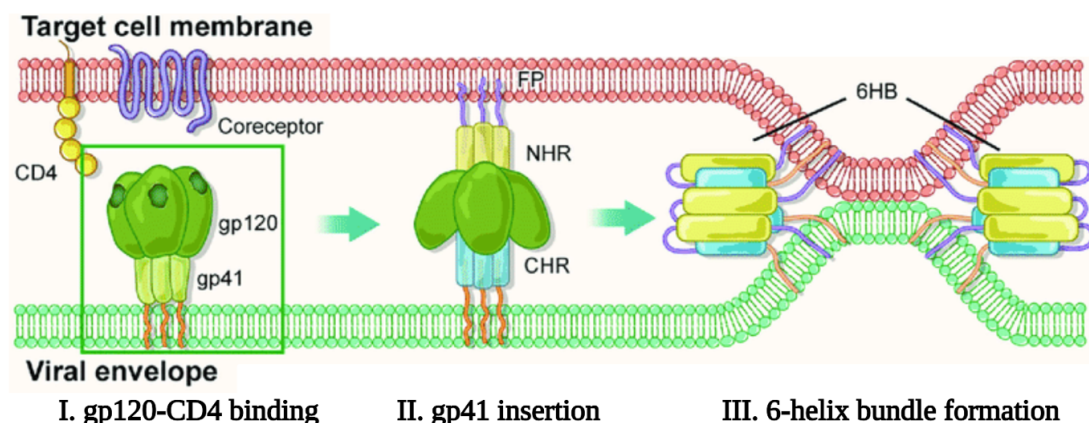
Figure 1.6 Schematic of the HIV-1 membrane fusion process.

I. gp120-CD4 binding. gp120 engages with the cell-surface receptor CD4, triggering a conformational change in V3. II. gp41 insertion. The gp120 conformational change allows gp120 to bind to the coreceptor and activate further conformational changes to expose the fusion peptide on gp41 that inserts into the target cell membrane. III. 6-helix bundle formation. Following insertion of the gp41 fusion peptide, the N-HR and C-HR of gp41 refold to form a six-helix bundle and force close apposition of the viral and target cell membranes. Adapted from [207].

1.3.4.2 SRM studies of HIV-1 fusion

Under dual-colour STED microscopy of HIV-1 particles attached to SupT1-R5 cells, it observed a clear polarisation of Env foci toward the CD4 patches, visualising direct receptor engagement [167]. This study also showed that this cell contact induces redistribution of Env molecules on the virus surface, presumably through progressive capture of individual Env trimers by nearby CD4 molecules. This finding is in agreement with a cryo-EM study that proposed the appearance of an 'entry claw' structure that interconnecting HIV and cell membranes [208].

SRM has also been used to study the rearrangements of viral components during attachment and fusion. Visualise through STORM and quantified via Ripley's K-function, the cluster size of matrix protein and capsid protein in virus particles increases after cellular internalisation, indicating that the internal structure of virus undergo rearrangements during HIV entry [209]. A subsequent study combining EM and SRM imaging suggested that, compare to immature HIV-1 particles, mature HIV-1 particles increase in size, this increase can solely be triggered by CD4-Env interaction and independent of virus fusion [210]. Hypothetically, the virus expansion may be an indication of an unknown mechanism that primes HIV-1 for fusion, which requires further study of the role of Env-CD4 interaction during viral membrane remodelling.

Few studies have been carried out to characterise receptor remodelling on the host cell membrane. A recent study combining fluorescence fluctuation spectroscopy imaging and number & brightness (N&B) analysis showed that, from the perspective of single Env protein, Env-CD4 interaction generates an asymmetric Env pre-hairpin intermediate that can further bind to two additional CD4 molecules. This leads to the formation of a final fusion-competent complex containing around 4 CD4 molecules binds to Env [211].

1.3.5 Env-CD4 interactions

The above studies indicate that SRM approaches are particularly suitable to visualise and quantify the dynamic behaviours of individual components on viral and host cell membrane as well as their interactions, such as to characterise both Env and receptor reorganisation on the host cell from Env binding to membrane fusion. Knowledge of the role of Env-CD4 interaction in these remodelling events could advance our understanding of the HIV-1 fusion process and the development of novel antiviral procedures.

1.3.5.1 Structural studies

A 3D reconstruction of the intact Env spike on the surface of the virion with CD4 by cryo-EM showed a CD4 orientation that was almost perpendicular to the Env trimer, probably in parallel with the viral membrane plane [179]. Compared with the unliganded Env trimer, CD4 binding induces major structural rearrangements, leading to an outward rotation and displacement of the gp120 protomers, along with the rearrangement of gp41 along the membrane plane [179].

More recent studies showed that CD4 induced Env conformational changes, including V1-V2 flip, V3 exposure, bridging sheet formation, fusion peptide repositioning and gp41 rearrangements. The exposed V3 loop and the bridge sheet are likely to become the binding site for coreceptor [212,213]. Further study compared the structural of single CD4 bounded Env complex and three CD4s bounded Env complex, single bounded CD4 has an orientation almost parallel

to the trimer axis, distinct from three CD4s bounded Env complex. This result indicates that single-CD4 bounded complex may represent the initial contact between Env and CD4 [214]. Similarly, characterised by smFRET, distinct conformational states have been assigned to the gp120 conformation of one CD4 bounded and three CD4 bounded Env trimer [215] (Figure 1.9). However, it is still unknown how stable the single CD4-bounded Env complex is and whether a single CD4 can induce the opening of the Env trimer and the formation of the coreceptor binding site. Alternatively, if multiple molecules and multiple coreceptors are required to activate one Env in the Env cluster, then the fusion process would be highly inefficient. Therefore, answer questions such as is there a specific number of Env and CD4 needed for a successful entry? If so, what is the minimal number requirements? It will not only guide the development of vaccines and therapeutics, but will also have important implications for viral entry of other enveloped viruses as well as other cellular events involving membrane fusion [170].
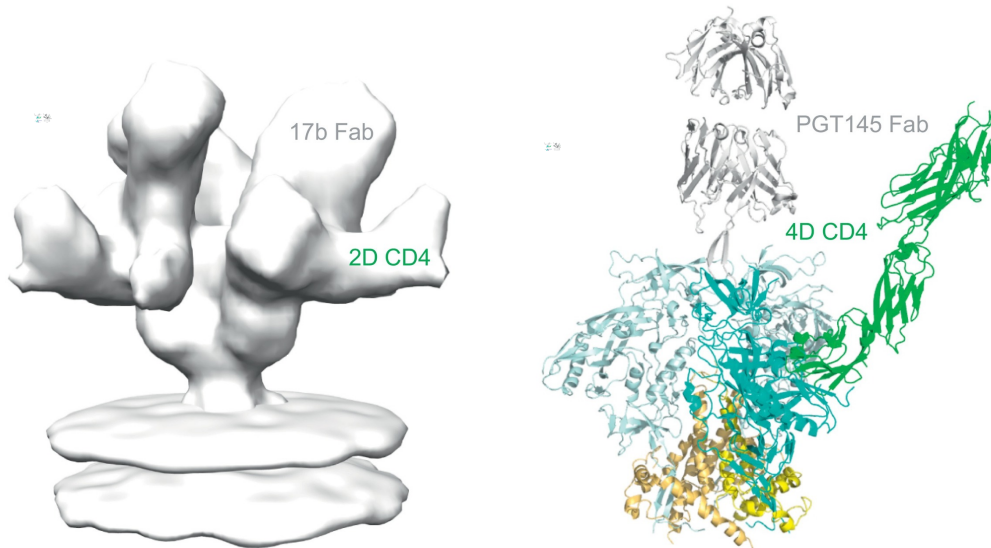
Figure 1.9 Env-CD4 interaction.

Left: 3D reconstruction of the HIV-1 Env spike on the viral membrane in complex with D1-D2 domains of CD4 (EMDB ID: EMD-5020 (Env portion); EMD-5023 membrane portion)). Right: The cryo-EM structure of Env trimer in

complex with CD4 D1-D4 domains (pdb ID: 5U1F [214]). Cyan: gp120, yellow: gp41, green: CD4.

1.3.5.2 Membrane domains for Env-CD4 interaction

Early stage studies showed that blocking biosynthesis of either cholesterol or sphingolipid in virus-producing cells, or cholesterol depletion from viral or target cell membranes, substantially reduces virus infectivity [216–218]. Furthermore, cholesterol depletion of the cell membrane has been shown to impact the association between gp120 and CD4, suggesting that the cholesterol and lipid ordered domain could be essential for the formation of Env-CD4 complex [219]. As CD4 has been found to associate with lipid ordered domains, it has been proposed that cholesterol- and sphingomyelin-rich lipid ordered domains are platforms for HIV fusion [220,221]. However, these sites seem energetically unfavourable for the fusion as they are more tightly packed and more ordered than surrounding membrane. A recent study using giant plasma membrane vesicles that contains both cholesterol-rich ordered and cholesterol-poor fluid lipid domains, authors demonstrated that CD4 is indeed substantially sequestered into ordered domains, while HIV fused from the boundaries between ordered and fluid lipid domains. This observation seems more convincing that can potentially explained by that HIV-1 exploit membrane discontinuities to gain entry into cells [222].

1.4 Thesis objectives

In this PhD, I aimed to establish a pipeline that could visualise and quantitative analyse ligand-receptor engagement on the PM. Using this pipeline, I can further study the organisational changes of the CD4 receptor during the HIV fusion process to answer questions, such as how many molecules are required from initial attachment to successful fusion? If a dynamic number of CD4 molecules is observed, further studies could focus on how CD4 is transported across the membrane and its association with other membrane domains and underneath actin cortex.

As previous known that multiple CD4 molecules are likely necessary for the initial gp120-CD4 interaction [223] and CD4 primarily exists as monomers or dimmers. I hypothesis that, post initial formation of Env-CD4 complex, surrounding CD4 molecules will travel towards Env clusters. Only those with the number of Env-CD4 complexes that meet the minimal requirement could undergo subsequent conformational changes to expose the coreceptor bining domain, leading to successful fusion. Furthermore, since these CD4 proteins are likely to be located between fences, actin-mediated hop diffusion could be responsible for this CD4 reorganisation.

Specifically, this project has the following aims,

1. To set up a well-characterised imaging and quantitative analysis pipeline to characterise the nanoscale organisation of CD4 on the PM of CD4+ T cells.
2. To explore the effect of HIV binding on the nanoscale organisation of CD4.

Chapter 2 Materials & Methods

2.1 Biochemical Methods

2.1.1 Details of antibodies used

Name	Recognised target	Species	Working concentration	Conjugated Fluorophore	Source
Q4120	Human CD4	Mouse	IF: 6 µg/ml	AlexaFluor 647	NIBSC centre for AIDS Reagents, NIH ARP 318
OKT4	Human CD4	Mouse	IF: 6 µg/ml	AlexaFluor 647 AlexaFluor 568	NIBSC centre for AIDS Reagents, NIH ARP 356
MC5	Human CCR5	Mouse	IF: 5 µg/ml Binding inhibition: 20 µg/ml	AlexaFluor 647 AlexaFluor 568	NIBSC centre for AIDS Reagents, NIH ARP 3114

Anti-p24/p55	HIV Gag	Rabbit	IF: 1:500	-	NIBSC centre for AIDS Reagents, ARP 432
Anti-mouse	Mouse	Goat	IF: 1:500	AlexaFluor 647	Life Technologies, A-21241
Anti-rabbit	Rabbit	Goat	IF: 1:500	AlexaFluor 568	Life Technologies, A-11036
Anti-rabbit	Rabbit	Goat	IF: 1:500	AlexaFluor 488	Life Technologies, A-11008

Table 2.1 Details of antibodies used in the thesis

2.1.2 Antibody conjugation

The monoclonal antibodies OKT4 (anti-CD4) and MC5 (anti-CCR5) were conjugated with AlexaFluor fluorophores using NHS-ester chemistry Lightning Link Kits (Innova Biosciences, Cambridge, UK). AlexaFluor 647 NHS Ester (A20106, Thermo Fisher Scientific, Waltham, United States) and AlexaFluor 568 NHS Ester (A20003, Thermo Fisher Scientific, Waltham, United States) were used. First, 10 μl of the IgG-PBS solution (1 mg/ml) was mixed with 1 μl of LL-Modifier reagent and 2-3 molar equivalents of NHS ester-functionalised fluorophore (10 mg/ml stocks in DMSO), and incubated at room temperature (RT, 23 °C) for 3-4 hours. Next, 1 μl LL-Quencher was added to terminate the reaction. Finally, unreacted fluorophore was washed out by dilution of the reaction volume to 500 μl and centrifugation through 3 kDa MWCO Amicon Ultra centrifugal filter columns (Z677094, Merck Group, Darmstadt, Germany) at 14,000 revolutions per minute (RPM) for 15 min. After the wash steps were repeated three more times, a 20 μl antibody-fluorophore conjugate solution was collected.

2.1.3 Protein concentration and dye to protein ratio measurement

Protein concentration was measured by spectrophotometrically by absorbance at 280 nm using an Eppendorf BioSpectrometer and μCuvette (6135000906, Eppendorf, Hamburg, Germany). If initial absorbance measurements exceeded 2.0, the antibody-fluorophore conjugate solution was diluted to obtain absorbance values less than 2.0.

The molarity of the protein was calculated as follows:

$$\text{Protein concentration (M)} = \frac{A_{280} - (A_{max} \times CF)}{\varepsilon} \times \text{Dilution factor (if available)}$$

in which ε = protein molar extinction coefficient; the ε of IgG is 210000 $M^{-1}cm^{-1}$. A_{max} = Absorbance of the dye solution measured at the peak excitation

wavelength for the dye molecule. CF = Correction Factor, an adjustment for the absorbance at 280nm caused by the dye; $CF_{AlexaFluor\ 647} = 0.03$, $CF_{AlexaFluor\ 568} = 0.46$.

The dye to mole ratio was calculated as follows:

$$dye\ to\ mole\ ratio = \frac{A_{max}\ of\ the\ labeled\ protein}{\varepsilon' \times M} \times Dilution\ factor\ (if\ available)$$

in which ε' = molar extinction coefficient of the dye. $\varepsilon'_{AlexaFluor\ 647} = 239000\ M^{-1}cm^{-1}$, $\varepsilon'_{AlexaFluor\ 568} = 91300\ M^{-1}cm^{-1}$.

2.2 Cell biology Methods

2.2.1 Cell culture

Human embryonic kidney (HEK) 293T cells (ATCC® CRL-3216) were maintained in Dulbecco's Modified Eagle Medium (DMEM, 31053-028, Life Technologies, Paisley, UK), supplemented with 10% (v/v) Fetal Bovine Serum (FBS, F9665, Merck Group, Darmstadt, Germany), 2 nM GlutaMAX supplement (35050061, Thermo Fisher Scientific, Waltham, United States), 50 U/ml penicillin and 50 µg/ml streptomycin (15140122, Thermo Fisher Scientific, Waltham, United States). HeLa-TZM-bl cells (NIBSC centre for AIDS Reagents, NIH ARP 5011) were maintained in DMEM, supplemented with 10% FBS (v/v) and 2 nM GlutaMAX.

SupT1 ([VB] ATCC® CRL-1942) is a CD4+/CCR5− cell line derived from T-cell lymphoblastic lymphoma. SupT1-R5 is a stable CCR5+ derivative of SupT1 kindly provided by James A. Hoxie (University of Pennsylvania). SupT1 and SupT1-R5 cells were cultured at a density of $1x10^5 - 1x10^6$ cells/ml in phenol red-free Roswell Park Memorial Institute (RPMI) 1640 medium (32404-014, Thermo Fisher Scientific, Waltham, United States), supplemented with 10% (v/v) FBS, 2 nM GlutaMAX, 50 U/ml penicillin and 50 µg/ml streptomycin.

All cells were incubated at 37 °C with 5% CO_2.

2.2.2 Phorbol Ester stimulation

SupT1-R5 cells were resuspended at a density of $1x10^4$ cells per sample in 20 μl cold RPMI 1640 with 0.4% (v/v) FBS and 6 μg/ml OKT4-AlexaFlour 647. The cell mixture was incubated on ice for 1hour before washing. The cell suspension was diluted to 10 ml using cold RPMI 1640 and centrifuged at 300xg for 6min at 4 °C. Next, the supernatant was aspirated and the cell wash repeated 2 times. After the final wash step, the cells were resuspended in 60 μl of cold RPMI 1640 and deposited on Poly-L-lysine (PLL)-coated coverslips (0.0025% (w/v) in ddH2O, P8920, Sigma-Aldrich, Dorset, UK) at 4 °C for 40 min.

Untreated control cells were directly transferred to cold 4% (w/v) paraformaldehyde (PFA) in PBS for 10min at 4 °C. Next, experimental and control samples were transferred to 37 °C RPMI 1640 supplemented with 0.4% (v/v) FBS, with 2 mg/ml Phorbol-12-myristate-13-acetate (PMA) or 4-α-Phorbol-12-myristate-13-acetate (4α-PMA), respectively. Cells were incubated for 15min before being returned to cold RPMI 1640 for 5min, and subsequently fixed by ice-cold 4% PFA in PBS for 10min. Finally, samples in cold the PFA solution were warmed to RT for 20min, followed by 3 washes with PBS. Samples were stored in PBS until imaging.

2.3 Virological Methods

2.3.1 Virus Preparation

HEK 293T cells were seeded at the density of $2.25x10^6$ cells per T75 culture flask to achieve <50% cell confluency the following day. The transfection mixture of 1.5ml OptiMEM (31985062, Thermo Fisher Scientific, Waltham, United States) and 15 μg HIV$_{JR-CSF}$ proviral DNA was incubated at RT for 5min, followed by gently mixing with 45 μl Fugene 6 transfection reagent (E2691, Promega, Madison, United States) until equilibrated to RT. Cell medium was

replaced with 15 ml antibiotic-free DMEM with 10% (v/v) FBS, followed by addition of the transfection mixture with gentle mixing. Cells were incubated at 37 °C with 5% CO_2 for 48hours. The culture medium was collected by centrifugation at 500 RCF for 10min to pellet cell debris. Next, the supernatant was transferred to Beckman ultracentrifuge tubes (355631, Beckman Coulter Inc, Brea, United States) and underlaid with a 5 ml sterile 20% sucrose cushion (diluted in PBS). The tubes were then topped up with DMEM supplemented with 10% (v/v) FBS and 2 nM GlutaMAX and HIV particles were pelleted by ultracentrifugation at 98,000 RCF for 2hours at 4 °C. The supernatant was gently aspirated to protect the viral pellet. The pellet was then resuspended in 2-5 ml RPMI 1640, aliquoted and stored in liquid nitrogen.

2.3.2 Virus Titration

Hela-TZM-bl cells were seeded at $1x10^3$ cells per well in a 96 well microtiter plate and incubated for 12-18hours at 37 °C with 5% CO_2. The cells were then infected with HIV in a series of two-fold dilutions from 1 in 2 to 1 in 256, at a final volume of 400 µl. In addition, 8 µg anti-CD4 Q4120 was added to each well to prevent syncytia formation at 6 hours post-infection (hpi). At 36 hpi, cells were washed in PBS 3 times and fixed in 4% (w/v) PFA in PBS for 30min at RT, followed by 0.1% PFA in PBS overnight at 4 °C. Next day, the cells were washed three times in PBS at RT and quenched in 50 mM NH_4Cl for 10min, followed by blocking and permeabilisation in 1% (v/v) FBS, 0.1% (v/v) Triton in PBS for 15min at RT. Samples were washed with 1% (v/v) FBS in PBS and incubated with rabbit antiserum to HIV p24/p55 Gag at 1:500 in 1% (v/v) FBS containing PBS for 1hour at RT, then washed 3 times with 1% (v/v) FBS diluted in PBS. Cells were incubated with the secondary antibody goat anti-rabbit IgG-AlexaFluor 488 and DAPI (1 µg/ml) for 20-30min at RT. Before imaging, cells were washed in PBS 3 times. Plates were imaged using a Perkin Elmer Opera Phenix high-throughput plate reader with a 20x air objective. Images (9 per well) were analysed using Columbus Image Analysis software.

The infection ratio for each well was calculated as

$$Infection\ ratio = \frac{the\ number\ of\ Gag^+ cells}{the\ total\ number\ of\ cells} \times 100\%$$

A line graph was plotted as Log10 of dilution rate (X) and the average infection ratio at each dilution (Y) and the standard derivation of the number of infected cells (IC) was then extracted. In this study, it was assumed that only one infectious particle was required to infect a cell, the multiplicity of infection (MOI) was calculated as IC / Total volume x dilution factor (total volume = area size of images/0.32 cm^2 (the size of a well in 96 well plates)).

2.3.3 HIV binding

SupT1 and SupT1-R5 cells at a density of 1x10^4 cells per sample were pre-incubated with 6 µg/ml OKT4-AlexaFluor 647 in a total volume of 20 µl RPMI 1640 with 0.4% FBS for 15min at RT. Cells with Env-CD4 binding inhibition were incubated with OKT4-AlexaFluor 647 and 20 µg/ml Q4120 for 15min at RT. The cells were equilibrated to 4 °C for 5min. To test the optimal amount of virus required for HIV-binding assays, multiplicities of infection (MOIs) of 15, 30 and 50 infectious units per cell were used. For the samples in the experimental groups, HIV-cell pre-binding was done at 4 °C for 1hour. Unbound virus particles were removed by diluting the HIV-cell mixture in 10 ml cold RPMI 1640 and centrifugation at 500 rpm for 10min.

For control samples, without warm-up, cell pellets were resuspended in 300 µl cold RPMI 1640 and deposited onto PLL-coated µ-Slide 8 Well dishes (Ibidi GmbH, Gräfelfing, Germany) for 40min. For experimental samples with the warming up process, the cells were resuspended in 50 µl cold serum-free RPMI 1640 and topped up with 3 ml pre-warmed (37 °C) serum-free RPMI-1640. Cells were immediately transferred to a 37 °C water bath for 1min, 2 min, 5min and 10min before adding 10 ml of ice-cold RPMI 1640 to the sample tube. Cells were then centrifuged at 500 rpm for 10min for washing. Next, the cell pellets were resuspended in 300 µl serum-free RPMI 1640 and allowed to settle onto PLL-coated µ-Slide 8 Well dishes for 40min.

Settled cells were fixed directly by incubation with 4% (w/v) PFA in PBS for 30min at RT. After fixation, cells were washed three times with PBS and permeabilised in 0.1% (v/v) Tween-20 in PBS for 5min, before being blocked in 4% (w/v) BSA in PBS for 20min. HIV p24 was labelled with rabbit antiserum to HIV p24/p55 Gag at 1:500 in 1% (v/v) FBS containing PBS for 1hour at RT, followed by three wash steps with PBS. The samples were then incubated with secondary antibody Goat-anti-AlexaFluor at 1:500 for 1hour at RT and washed 5 times in PBS. A second round of fixation was done with 4% (w/v) PFA in PBS for 30min at RT, before 5 PBS washes. Prepared samples were stored in PBS at 4 ^{o}C before imaging.

2.4 Imaging related Methods

2.4.1 Imaging dish cleaning and coating

μ-Slide 8 Well dishes were prepared a day before use by washing with 100% ethanol and ddH$_2$O wash for 2 times each. After the dishes were dried, 0.0025% (w/v) PLL in ddH$_2$O was added to cover the glass bottom of each well and incubated overnight at 37 ^{o}C. The PLL solution was removed by aspiration the next day and dishes were rewashed in ddH$_2$O 2 times. For fiducial bead coating, TetraSpeck microspheres (T7279, Thermo Fisher Scientific, Waltham, United States) were used. The bead suspension was diluted at 1:1000 in PBS, added to corresponding wells and incubated at RT for 30min before washing twice in ddH$_2$O. All dishes were then dried at 37 ^{o}C for 30min.

2.4.2 Mounting Media

SMLM buffer was prepared from two pre-mixed solutions: a base buffer and a Glox mix. The base buffer consists of 150nM Tris, pH 8.0, 1% (v/v) glycerol, 1% (w/v) glucose and 10 nM NaCl. The Glox mix consists of 0.5 mg/ml glucose oxidase and 40 mg/ml catalase in ddH$_2$O.

The SMLM buffer was freshly prepared just before imaging from the pre-mixed base buffer and Glox mix, with an additional 1% (v/v) beta-mercaptoethanol.

Finally, the sample wells were filled with STORM buffer, and the lid was sealed with High-Performance Black Masking Tape (Thorlabs, UK).

2.4.3 TIRF-STORM imaging

Imaging was carried out on a Zeiss Elyra PS.1 at a pixel size of 100 nm, with an alpha Plan-Apochromat DIC M27 Elyra 100x 1.46 numerical Aperture (NA) oil objective, additional 1.6x optovar magnification and Andor iXon 897 electron multiplying charge coupled device (EMCCD) camera. For each STORM dataset, 15000 sequential frames were acquired in TIRF configuration (TIRF angle ~70°), using 33 ms exposure time and 300 EM camera gain with 642 nm or 561 nm excitation at maximum power output (Laser power were ~3.98 kW/cm^2 and ~3.71 kW/cm^2 on the sample, respectively). Fluorophore photoswitching was dynamically controlled using periodic 405 nm illumination at an intensity of approximately 0 - 0.0586 kW/cm^2 (on-sample fluorescent intensity). The Zeiss Definite Focus autofocus function was used throughout all acquisitions.

2.4.4 On sample fluorescent intensity measurement

The laser power at sample (P) was measured using a power meter with the probe placed at the sample plane on the microscope, and the laser at the same percentage power as used during imaging. The imaging field of view area was calculated based on the size of the camera chip and magnification used. The on sample fluorescent intensity is calculated as P / A.

2.5 Imaging analysis methods

2.5.1 Localisation detection and image reconstruction algorithm

SMLM imaging datasets were processed using the ThunderSTORM analysis plugin [224]. First, initial localisation detection was performed using the local maximum method, followed by sub-pixel localisation using the integrated

Gaussian model and fitting by Maximal Likelihood Estimation. Then, in post-localisation processing, drift correction was performed by cross-correlation with the number of bins set as 5. Finally, each image reconstruction was rendered by a normalised 20 nm Gaussian.

2.5.2 Channel registration

Channel registration was performed using a chromatic aberration correction plugin generated by the Jalink lab (https://jalink-lab.github.io/). Fiducial bead-coated coverslips were imaged under 647 nm and 568 nm channels before each imaging session. Fiducial bead images were used as references for estimating the transformation between channels and correction parameters were obtained. Finally, these parameters were applied to localisation data of the experimental samples.

2.5.3 Cluster manual annotation

The manual annotation of clusters in SMLM data was carried out in Fiji [225]. Cross-sections of identified clusters were drawn individually in Fiji. Their intensity profiles were plotted and fit with a Gaussian distribution of standard deviation σ. The diameter of each cluster was estimated by the Full-Width Half Maximum (FWHM) as d = 2.35 σ.

2.5.4 Ripley's function analysis

The Ripley's K function was carried out using Ripley's K analysis integrated into SR-Tesseler [126]. The min radius, step radius and max radius were set as 10, 10, and 200, respectively. The principle of Ripley's K function is defined as:

$$K(r) = \frac{1}{n} \sum_{i=1}^{n} Np_i(r) \div \lambda$$

$Np_i(r)$ is the number of points in the vicinity of the ith detection at a 10 nm distance. λ is the localisation density.

Ripley's H function is a variation of the K function with an additional normalisation step such that the expected value is 0.

$$H(r) = \sqrt{K(r) \div \pi} - r$$

The cluster radius is retrieved by the value of r maximising H(r), representing the maximum aggregation radius.

2.5.5 Voronoï based cluster analysis

The Voronoï diagram-based cluster analysis was processed by SR-Tesseler [126]. Regions of interest (ROIs) were manually selected to include as much of the plasma membrane as possible while avoiding cell-edge effects. A density factor of 0.5-1.5 was tested on input images during the first round for segmenting the regions of interest as a single object. For cluster identification in the second round of density-based segmentation, a density factor of 0.1-4 was tested. Cluster diameter, the cluster density per ROI (number of clusters detected/ROI area (μm^2)) and the number of localisations per cluster were obtained for each cluster.

2.5.6 DBSCAN based cluster analysis

DBSCAN-based cluster analysis, was implemented using the Clus-DoC [226] software package, in which 30 nm Epsilon and 1 minimum point parameters were chosen throughout the study. ROIs were manually selected to avoid cell-edge effects while maintaining as much plasma membrane as possible. Parameters acquired were area size and corresponding diameter, the cluster density per ROI and the number of localisations for each cluster.

2.5.7 Colocalisation analysis

Channel registered fiducial bead coated dishes were used to determine the colocalisation threshold in Clus-DoC [226]. The optimised threshold was set to 0.4 when the majority (>99%) of colocalisation events displayed a peak DoC distribution, indicating high colocalisation. Aside from the DoC score,

information, such as the percentage of colocalisation between channels, the mean cluster diameter in the colocalised and non-colocalised areas, were obtained.

2.5.8 Molecular counting

Molecular counting used in this study was adopted from Sieben et al. [227]. Briefly, grouping parameters calibration values were determined using dishes coated with 1 µg/ml dye-conjugated OKT4 for 15min at RT. The dishes were washed once in PBS and imaged under the same experimental conditions as those used for other experimental samples. Imaging of the isolated fluorophore-conjugated antibodies was carried out and processed as described in 2.4.6 and 2.5.1. Localisations within 30nm were merged as one localisation frame by frame to form a new coordinates map and temporally binned to extract calibration parameters for molecular counting. All localisation processing was performed using custom-written MATLAB (MathWorks) scripts kindly provided by Dr. Christian Sieben (Helmholtz Centre for Infection Research, Braunschweig, Germany). The alignment of localisations from individual molecules also allowed for the estimation of the localisation precision.

2.5.9 Theoretical Poisson statistical model

The number of molecules per cluster was used to generate a Poisson probability distribution, which simulates a random distribution of receptors. Considering a CD4 density of approximately 100000 molecules/cell on SupT1-R5 cells and typical T-cell shapes with a radius of approximately 10 µm [183,191], cells were thus approximated as a flat disk with a total surface area of 630 µm^2.

The expected probability of observing a number of receptors k in a given area A of the cell surface was provided by the discrete Poisson probability distribution, $P(k; \lambda)$, where $k \geq 0$ and $\lambda = nA$ is the mean receptor count

expected when counting receptors on a patch of area A (λ is also the mean of the distribution). This model was built assuming independence of receptor-counting events; no interactions between receptors, signalling, or active processes or receptor mobility were considered. Therefore, counting multiple CD4 receptors in a given area was considered to be by chance (to random statistical fluctuations).

CD4 clusters identified in untreated cells in this study ranged from 10-100 nm. The corresponding mean λ_i is in the range 0.1-6. The Poisson distribution has significantly different shapes for these different values of its mean parameter and is asymmetric for decreasing values of λ_i below 5. For the larger λ_i, the distribution mean and peak position shifted to the higher k and the probability of counting a larger number of molecules per cluster increases. For these reasons, the model used in this study considered the different sizes of all the measured clusters to calculate the overall probability distribution of numbers of molecules per cluster observed when counting receptor numbers in circular cluster areas equivalent to those occupied in the measured CD4 clusters.

The expected overall distribution of numbers of molecules per cluster is the average of the Poisson distributions corresponding to all the observed cluster sizes. The overall probability of counting k receptor is,

$$P(K) = \frac{1}{N} \sum_{i=1}^{N} P(k; \lambda_I)$$

In which *i* is the cluster index, N is the total number of clusters measured. Therefore, it summed over all the different clusters, $P(k; \lambda_I)$ is the Poisson distribution for a given cluster *i* with radius r_i that occupies a surface area $A_i = \pi r2_i$), and $\lambda_i = nA_i = \pi r_i 2n$ is the corresponding mean value of the Poisson distribution for cluster *i*.

The model is normalised by excluding and dividing by the sum of the remaining counts to compare expected and measured distribution. This is because areas with zero receptors were not measured in our experiments. Calculations were

performed using custom-written Python scripts kindly provided by Dr Isabel Llorente Garcia (UCL).

2.5.10 Statistical Analysis

In data with two objects to compare, data is presented as means ± standard deviation (SD) from a minimum of three independent experiments. N is indicated in each figure separately. Student t-tests were performed using GraphPad Prism (GraphPad Prism version 9.1.2 for Windows, GraphPad Software, San Diego, California USA). In data with more than two objects to compare, data is presented as means ± Standard error of the mean (SEM) from a minimum of three independent experiments, two-way ANOVA were performed using GraphPad Prism (GraphPad Prism version 9.1.2 for Windows, GraphPad Software, San Diego, California USA).

Chapter 3 Nanoscale visualisation and quantitative analysis of CD4 on CD4⁺ T cells

3.1 Introduction

3.1.1 The definition of a cluster in SMLM

STORM has made it possible to image and measure complex biological structures in cells with a nanoscale precision [228]. This is achieved by producing a coordinate table with tens of thousands of localisations. Before characterising receptor organisation, the terminology used to describe membrane organisation in SMLM requires clarification. In CFM, it is reasonable to use the term 'cluster' to describe foci or 'island' of molecules in a particular region observed in diffraction-limited images, representing a location that likely contains more than one molecule of the same type. However, when the resolution is increased to near molecule level in SMLM, the term 'cluster' could be confusing when only one protein (monomer) may be detected in a particular region. In SMLM studies, various terminologies have been adopted, including protein islands (35-70 nm) [70], nanoclusters/clusters (~50 nm [74]; 200 nm -700 nm [73,229]) and oligomers (ranging from 1-15 TCRs [230–232]). Rather than trying to incorporate these different but overlapping terms, in this SMLM study I use 'cluster' to describe localisation(s) grouped within a 250nm (sub-diffraction-limit) scale. Furthermore, this grouping would not be expected in a random distribution' [112]. Thus, I place minimal restrictions on cluster features, such as shape, size, density, number of proteins per cluster and cell status (e.g. activated *vs* resting).

3.1.2 Sample preparation and receptor labelling optimisation in STORM imaging

Immunofluorescence labelling for SMLM is essentially the same as for CFM. STORM generates images reconstructed from localisation coordinate maps composed of the detected blinking events of fluorescent molecules labelling the samples. With such an increase in resolution and detection sensitivity, potential artefacts associated with specimen preparation would be exaggerated in SR while remaining innocuous in CFM. Although STORM configurations are becoming standardised in commercial systems, the sample preparation protocols are largely validated on a case-by-case basis and mostly on widely studied structures, such as the cytoskeletons. Thus, STORM application to SR studies of the native organisation of receptors in the PM is potentially prone to artefacts. This chapter describes my analysis of each of these variables to establish a faithful SR visualisation pipeline for studying CD4 distribution on CD4$^+$ T cells using STORM. Furthermore, a validated SR visualisation pipeline is also crucial for precise quantitative analysis.

3.1.2.1 Chemical fixation for membrane-associated components in SR

Chemical fixation, a critical early step in specimen preparation, is to immobilise cell components and preserve the microscopic integrity. However, it is known from EM and other studies that fixation efficacy can vary for different subcellular domains and fixative reagents and buffer [233–235]. Fixative reagents, such as paraformaldehyde (PFA), glutaraldehyde (GA) or a mixture of both, are commonly used in cell fixation [236]. PFA preserves the majority of the epitopes recognisability for specific antibodies [237,238]. GA destroys some of tertiary protein structures and make them unrecognisable for antibodies but tending to give better structural preservation [238,239]. Furthermore, the penetration of GA into cells is slower than PFA. Therefore, sample permeabilisation is sometimes required during/before GA fixation if a rapid fixation is essential [238,239]. GA can also be problematic when employed in STORM due to its potential to introduce sample autofluorescence [240]. However, when comparing fixatives for visualising microtubules, mitochondria and actin in SR in COS7 cells, one study suggested a consecutive of 1.5min 0.4% GA + 0.25% Triton X100 and 15min 3% GA fixation is optimal, with minimal nonspecific stain and structure perturbations [241]. For observing PM receptors in lymphocytes, one previous study showed that 1% PFA fixation alone for 10min at RT is insufficient in CD44 and CD31 immobilisation, with clustering observed after addition of a secondary crosslinking antibody [10]. Therefore, 1% PFA + 0.2% GA fixative mixture for 10min at RT was recommended [242].

Besides the fixative reagent, the buffer was also considered for reducing fixation artefacts. The cytoskeleton-preserving buffer (PEM), consisting of 0.1M PIPES, 0.5mM $MgCl_2$ and EDTA [243], is a well-known buffer for stabilising the cytoskeleton during fixation. This buffer was first tested in STORM by labelling actin cytoskeleton and its associated protein in HeLa and COS7 cells with GA fixation [239]. When labelling cell surface antigens, a recent study from our lab showed that, for STORM imaging of CD4 expressed in COS7 cells, there was no detectable difference between PFA/PBS fixation and PFA/PMEM

fixation [244]. Previous validations from our lab using single-particle tracking also compared 4% PFA fixation alone with 4% PFA + 0.01% GA. The results suggested that PFA alone was sufficient to immobilise CD4 and CCR5 ectopically expressed in CHO cells. Also, the fluorescence signal reduced drastically in 4% PFA + 0.01% GA samples [81]. Considering the effectiveness of 4% PFA fixation in both CD4 expressing COS7 and CHO cells, I used 4% PFA as the fixative and PBS as the buffer for the work described in this chapter.

3.1.2.2 Sample permeabilisation in SR

Antibodies can access extracellular epitopes without cell permeabilisation, but to access intracellular antigens cells must be permeabilised. However, sample permeabilisation post-fixation has the potential to disrupt membrane receptor organisation [239,245]. Permeabilisation could be avoided in most of the experiments carried out in this study, however, permeabilisation was necessary for localising membrane-protected intraviral antigens such as HIV p24 and potentially impact on the cells. Previous studies showed that permeabilisation with non-ionic detergents (Triton X100 and Tween-20) yielded preservation in cytoskeleton structure [241] and membrane receptor organisation [81]. Thus, in this study, I employed Tween-20 when permeabilisation was necessary.

3.1.3 From localisation to super-resolution images: STORM imaging analysis optimisation

3.1.3.1 Cluster analysis methods, parameters measured, and their application to characterising membrane receptors

With the localisation maps produced in SMLM many cluster-associated attributes can now be measured quantitatively, and their potential biological links can be uncovered. For example, for individual labelled protein, cluster size, shape, molecular density per cluster, comparison of cluster density between regions, and intercellular comparisons of these features can all be

determined. For dual colour labelled proteins, spatial correlations can also be used to characterise molecular interactions. Several cluster analysis approaches have been developed. The theoretical basis of these approaches has been summarised in Chapter 1.2.3. As with other steps in SMLM, the cluster analysis algorithm of choice differs from study to study, depending on the nature of the observed clusters, the availability of models to use, and the information that is extracted. While most published works are proof-of-concept studies validating custom-developed algorithms, there has been some application of these methods to HIV and/or T cells. These studies and their biological applications are summarised in Table 3.1.

Reference	Protein of interests	Organisms	Imaging technique	Data size (cells per condition)	Cluster analysis methods	Parameter measured
Owen et al. [103]	Lck and Src	HeLa and Jurkat T cell	PALM and STORM	NR	Ripley	Size; cluster density
Lillemeier et al. [70]	TCR and Lat	Primary T cells from mice	PALM	5-10	Ripley	Radius; Molecular density per cluster, Cluster density
Williamson et al. [109]	Lat	Jurkat T cell and primary T cell from mice	PALM and STORM	3-25	Ripley	Diameter; Molecular density per cluster, Cluster density
Martin et al. [246]	HIV IN, CA, MA and Env Tetherin	HeLa	PALM and STORM	5-6	Ripley	Size; molecules per cluster; degree of colocalisation

Pereira et al. [209]	HIV matrix HIV capsid	HIV$_{NL4-3}$ MT-2 cell	STORM	NR	Ripley	Diameter;
Rossy et al. [247]	Lck and CD45	Jurkat T cell	PALM and STORM	NR	G&F	Degree of colocalisation
Roh et al. [192]	CD4	Primary T cells from mice	PALM STORM	15-33	Ripley	Radius; molecules per cluster; degree of colocalisation
Peters et al. [248]	Lat and F-actin	Jurkat T cell	iPALM and STORM	NR	angular Ripley	Degree of colocalisation
Rubin-Delanchy et al. [249]	CD3	Primary T cell from Human	PALM and STORM	30 ROIs	Bayesian Ripley	Radius; Localisation density per cluster, Cluster density

Griffié et al. [250]	Lfa-1	Primary T cell from Human	STORM	10	Ripley, G&F, Bayesian	Radius; Localisation density per cluster, Cluster density; Degree of colocalisation
Griffié et al. [118]	Zap-70	Primary T cell from Human	PALM and STORM	12	Bayesian	Radius; localisation density per cluster, Cluster density;
Griffié et al.	CD4	Primary T cell from Human	Live-cell PALM	6	Ripley, Bayesian	Radius; Number of clusters
Pageon et al. [115]	TCR, CD45	Jurkat T cell	STORM	NR	Ripley, DBSCAN	Diameter; Degree of colocalisation; Diameter in colocalised area vs non-colocalised area

Pageon et al. [251]	TCR, CD3, pZap70, pLat	Jurkat T cell, Primary T cell from mice	PALM and STORM	3-13	Ripley, DBSCAN	Diameter; Molecular density per cluster; Diameter in colocalised area vs non-colocalised area
Peters et al. [252]	F-actin, Microtubule network	Jurkat T cell, HeLa cell	STORM	3-5	Voronoï, angular Ripley	Number of fibres; Fiber length, Enclosed area; Angle of branching

Table 3.1 Summarises of quantitative methods used in published SMLM studies on HIV or T cell biology.

NR represents Not Related. Modified and expanded from [123].

In this study, I intended to characterise the organisational changes of CD4 clusters on SupT1-R5 cells during HIV binding by first looking at changes in the cluster diameter of receptors. As indicated in Table 3.1, DBSCAN and Voronoï-based analysis are both widely available approaches to characterise receptor organisation at a single cluster level. Therefore, I first validated the performance of these most frequently used open-source algorithms.

3.1.3.2 Estimating the number of molecules per cluster

With near molecular resolution imaging techniques, it is possible to quantitatively characterise molecule organisation by estimating the number of molecules. However, molecular counting, i.e the translation of the number of detected localisations to the number of molecules, remains challenging. As discussed in Chapter 1.2.4, the most significant hurdle is the potential for overcounting. This overcounting can be brought in from labelling as well as the photo-switching kinetics of an individual fluorophore.

3.1.3.2.1 Controlling probe density in localisation identification

Ideally, to precisely localise a target molecule, the one fluorophore attached to the target molecule is only detected once during an acquisition. Although a secondary antibody is recommended in the immunolabelling process to amplify the detected signal and improve assay sensitivity, additional fluorophores can be problematic. When multiple secondary antibodies attach to a single target molecule, multi-emission events are likely to be detected, resulting in multi- localisations. These events are hard to correct post-processing and will introduce more artefacts in the follow-up quantification procedure. Moreover, the information on dye-to-protein molar ratio of commercial secondary antibodies is often obscure. This inevitably brings in another layer of uncertainty for localisation, detection and identification.

Experimentally, the dye-to-protein ratio can be measured spectrophotometrically (Chapter 2.1.2). This number can be interpreted as a mean ratio of the number of dye molecules per antibody molecule. Thus,

primary antibody labelling with one dye conjugated per antibody molecule is ideal for STORM imaging when labelling efficiency is not compromised. The conjugated dye-to-protein ratio and CD4 labelling efficacy of dye conjugated primary antibody are validated and quantitatively analysed in this chapter.

3.1.3.2.2 Photo-switching properties of fluorophores in localisation identification

The number of times an individual fluorophore undergoes a switching cycle and blinks is uncertain. Therefore, one fluorophore might blink multiple times during an acquisition period. As a result, multiple localisations are recorded for a molecule, leading to overcounting. To minimalise overcounting, a calibration experiment is essential to estimate the average dark gap within an acquisition cycle. This average dark gap is then used to calibrate the experiment data. The reference data must be acquired with the same labelling method and experimental conditions to constitute a faithful correction coefficient [140].

The biological applications of molecular counting relating to T cell and virus biology have been summarised in Table 3.2. The biological application is still limited. Most of them are used as supplementary information to back up cluster analysis described in 3.1.2, especially in STORM studies. For this study, I adopted the algorithm used previously to characterise EGFR and Sialic Acid behaviour in Influenza A virus entry, which has a similar experimental setting using fluorophore-conjugated antibody labelling and STORM imaging [227].

Reference	Protein of interest	Organisms	Imaging technique	Molecule counting method
Williamson et al. [109]	Lat	Jurkat T cell and primary T cell from mice	PALM and STORM	Switching cycle calibration with gap time = 50
Roh et al. [192]	CD4	Primary T cells from mice	PALM and STORM	Estimated detection efficiency
Hu et al. [253]	TCR	Primary T cells from mice	Light-sheet STORM	Estimated detection efficiency
Iliopoulou et al. [211]	CD4 and CCR5	COS7 cell and	Fluorescence fluctuation spectroscopy and STORM	N&B

Sieben et al. [227]	EGFR and SA	A549 cells	STORM STED	Switching cycle calibration with antibody image
Patel et al. [254]	LAT	Jurkat T cell	STORM	Switching cycle calibration with experiment training data (Markov model [255])

Table 3.2 Summary of the molecular counting methods used in published SMLM

3.1.3.3 Quantitative colocalisation analysis and their biological interpretation in SMLM

3.1.3.3.1 Channel alignment

In the context of multicolour STORM, channel alignment includes drift correction and chromatic aberrations. Drift correction is routinely performed and typically implemented in imaging processing algorithms based on cross-correlation. However, chromatic aberration can be neglected in conventional fluorescence microscopy as it occurs on a sub-diffraction scale. Still, it is an essential consideration for SR imaging when visualising nanoscale structures [256–259]. The primary source of chromatic aberration are motion artefacts, such as mechanical movements and inevitable optical imperfections. Thus, it remains consistent with a specific imaging setting. For STORM, chromatic correction must be done at the localisation coordinates level. Chromatic aberration is generally assessed using fiducial bead-coated coverslips under both channels by custom scripts. The information is then used as the aberration correction reference for aligning localisation data for the molecules imaged. The performance of the chosen algorithm is validated by comparing the pre- and post-processing images in this chapter.

3.1.3.3.2 Quantitative colocalisation analysis interpretation

Several studies have linked protein spatial reorganisation and colocalisation with their function using SMLM in the context of T cell immunological synapses [115,118,152,192,251]. Multi-colour SMLM has allowed us to measure spatial organisation at the level of individual molecules, and to extend this approach to look at cellular responses to molecule network interactions. The term 'degree of colocalisation' has been brought in to quantitatively describe the spatial relationship between molecules. However, this parameter should be interpreted cautiously as spatial relationship and size must both be considered (Figure 4.1). Therefore, choosing a quantitative colocalisation analysis

approach with single-molecule analytical capability is essential when target molecules have distinct size differences.

As discussed in Chapter 1.2.5, widely adopted colocalisation analysis approaches in SMLM are coordinate-based approaches. I adopted Clus-DoC [115], an SMLM data analysis platform that incorporates CBC [151] for cluster colocalisation analysis at the individual localisation level. This platform quantifies a DoC score on a per-molecule basis. The DoC score for each localisation of protein A and protein B, respectively, is calculated using a rank correlation coefficient (detail explanation in Chapter 1.2.5.1) from -1 (segregated), via 0 (non-colocalised) to 1 (colocalised). Clus-DoC SMLM data analysis platform takes a step further to eliminate potential artefacts by introducing a customisable DoC threshold. The threshold is set initially as 0.4, assuming that a 10 nm shift is inevitable in any SMLM method, as the best imaging precision is 10 nm. The threshold is calculated based on two identical SMLM datasets, except one is shifted in a set direction by 10 nm. Comparing these two datasets, >90% of localisations have a DoC score > 0.4, with the DoC distribution peak at 1. Thus, the colocalisation average diameter in colocalised regions *vs* non-colocalised regions (expressed as a percentage) can be extracted with confidence.
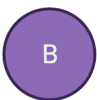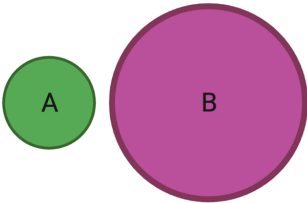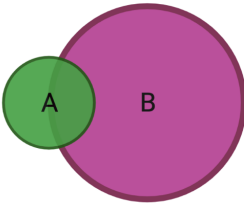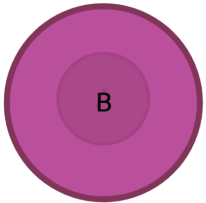
A => B	0%	50%	100%
B => A	0%	50%	100%
A => B	0%	50%	100%
B => A	0%	10%	20%

Figure 3.1 Schematic of the degree of colocalisation in SMLM colocalisation analysis.

A represents a cluster of protein A. B represents a cluster of protein B. A => B represents the degree of cluster A colocalised with cluster B. B => A represents the degree of cluster B with cluster A.

3.1.3.4 Statistical simulation analysis to evaluate the randomness of receptor distribution

The range of quantitative analysis methods applied to spatial organisation has brought the concept of a cluster to a scale of just a couple of molecules. This has led to another interesting question in molecular biology, whether the spatial distribution observed is random. Therefore, statistical methods to validate 'randomness' are essential when building a quantitative analysis pipeline. For example, discrete Poisson probability distribution has been used in a previous study, the possibility of random distribution of clusters detected under TIRF imaging has been estimated using the cluster radius produced by Ripley's function [148]. In this study, Lagache et al. found that clathrin (assumed to be the site for clathrin-dependent endocytosis) were randomly distributed, whereas interleukin-2 (assumed to be the site for clathrin-independent endocytosis) spots were organised into clusters, suggesting distinct physical mechanisms and cellular functions for each pathway.

3.1.4 Objectives

The work described in this chapter aimed to establish a reproducible and reliable pipeline to visualise and quantitative analyse plasma membrane nanoscale distribution of CD4. As most of the factors mentioned above are not standardised, careful assessment at each step was essential.

- Validate commonly used cluster analysis approaches and use molecular counting to determine CD4 nanoscale distribution on untreated SupT1-R5 cells.

- Observe the effect of pre/post-fixation labelling on PM CD4 and CCR5 organisation.
- Assess the effect of 4°C incubation before returning to 37°C incubation for different time points on CD4 and CCR5 organisation.
- Examine the dual colour STORM fluorophore choice and channel alignment protocol.
- Evaluate the visualisation pipeline of CD4 and CCR5 organisational changes post chemical and agonist treatment.
- Build a statistical model to feature CD4 random membrane organisation using Poisson distribution.

3.2 Results

3.2.1 Comparison of methods for quantitatively analyse CD4 clusters

This study aims to characterise the nanoscale organisation of HIV receptor during virus binding. Therefore, a non-neutralising labelling antibody is required for this purpose. To this end, I used the well characterised anti-human CD4 antibody OKT4 [260], which interacts with an epitope in the D3 domain of the human CD4 molecule. SupT1-R5 cells, a human non-Hodgkin lymphoma CD4+ T-cell line with stable CCR5 expression, were co-incubated with 6 µg/ml OKT4 at 4°C for 1hour before fixation with 4% PFA. In addition to using a low temperature for labelling, antibody-induced receptor dimerisation was further minimised by using an excess amount of antibody which should favour monovalent binding [81]. Cells were then incubated with the fluorophore conjugated secondary antibody and imaged (Figure 3.1). Based on reconstructed images, CD4 was seen in numerous clusters homogeneously distributed across the field of view (FOV) (Figure 3.1). However, detailed quantitative analysis is essential for comparison for data at this scale.
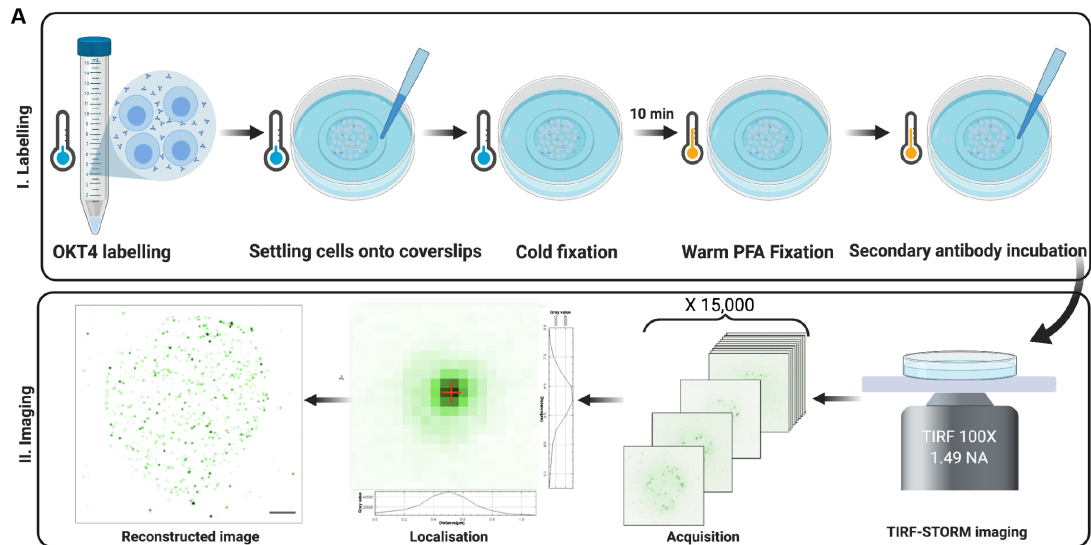
Figure 3.2 Schematic of the labelling and imaging pipeline used.

A. (I) Labelling. SupT1-R5 cells were pre-incubated at 4°C with Q4120 or PFA fixed before being incubation with Q4120 at 4°C. (II) Imaging. Cells deposited on imaging surfaces were imaged using standard TIRF-STORM acquisition. Scale bar = 2 μm.

Clus-DoC (DBSCAN) and SR-Tesseler (Voronoï) have all been used to quantitatively characterise membrane receptors (Chapter 1.2.3, Chapter 3.1.3.1, Table 3.1). However, these methods haven't been used as quantitative analysis of CD4 on CD4+ T cells. To quantitatively characterise CD4 spatial relationship on CD4+ T cells, I started by comparing CD4 cluster diameters using Clus-DoC (DBSCAN) and SR-Tesseler (Voronoï) on untreated SupT1-R5 cells.

By looking at the output images after processing, I saw that SR-Tesseler tended to miss identifying clusters regardless of the parameters used (Figure 3.3 A). Quantitatively, SR-Tesseler identified fewer clusters per ROIs with smaller diameters; 253 ± 86 clusters with diameters of 26 ± 0.28 nm were identified in the same set of ROIs. By contrast, outputs from Clus-DoC displayed results closest to the manual annotation. It identified 643 ± 92 clusters per ROI with diameters of 55 ± 0.25 nm (Figure 3.2 B). Therefore, I chose Clus-DoC for subsequent analyses.

The number of clusters and diameters identified in each method varied. To choose an optimal cluster analysis approach for further characterisation, I decided to manually annotated CD4 in Fiji [261] and reference it as a ground truth. Cross-sections of identified clusters were drawn individually. The cluster diameter was estimated using the Full-Width Half Maximum (FWHM). From manual annotation, 688 $\pm$ 136 clusters per ROIs were identified with diameters of 65 $\pm$ 0.27 nm (Figure 3.2 B). By comparison, outputs from Clus-DoC displayed results closest to the manual annotation. Therefore, I chose Clus-DoC for subsequent analyses.
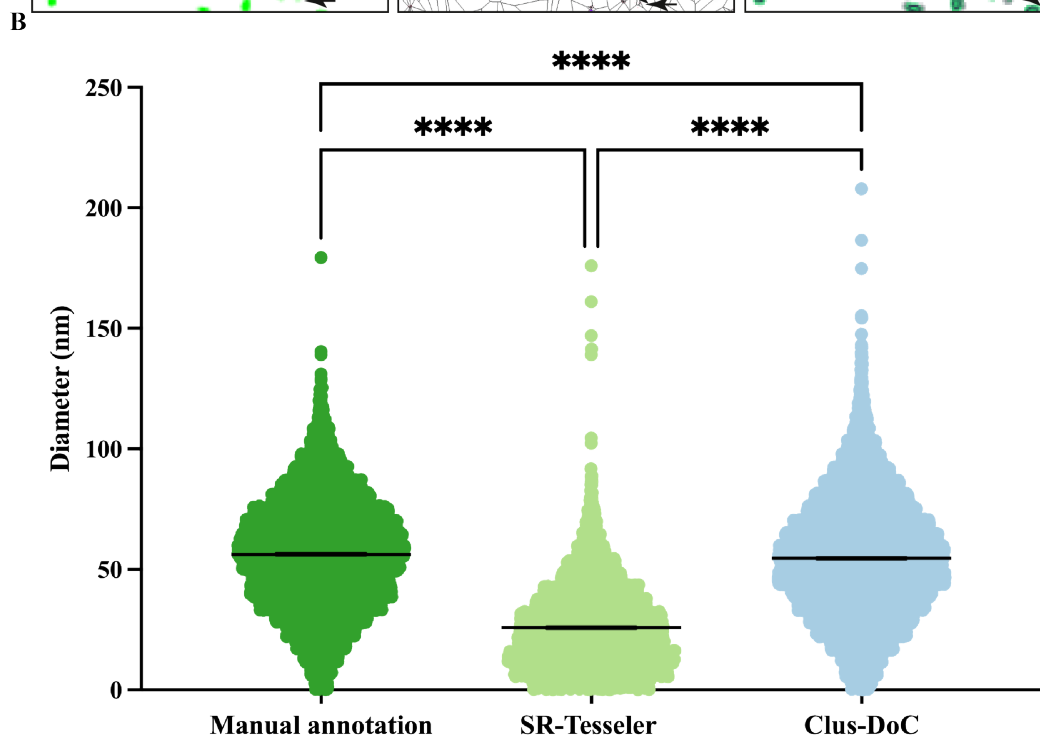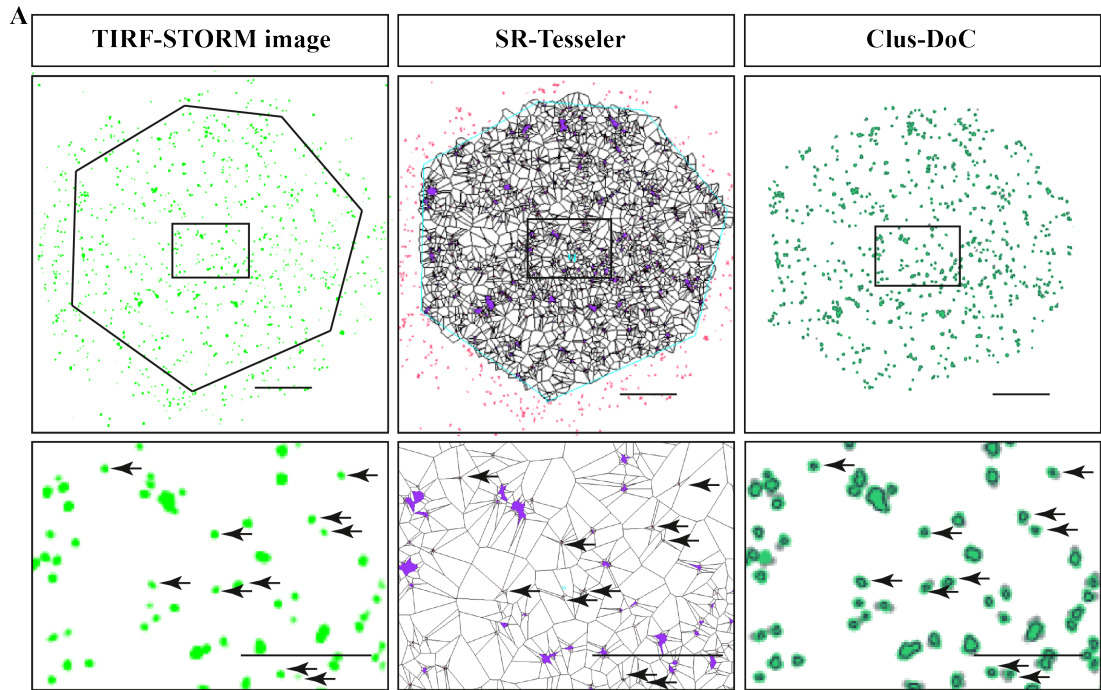
Figure 3.3 Quantitative analysis of CD4 clusters on SupT1-R5 cells with manual annotation, SR-Tesseler and Clus-DoC.

A. Representative TIRF-STORM images of CD4 clusters on SupT1-R5 cell. Compared with SR-Tesseler, Clus-DoC identified cluster maps in the same ROIs. Arrows indicate absently identified clusters in SR-Tesseler and the coordinate location in TIRF-STORM and Clus-DoC images. B. Quantification

of CD4 cluster diameters in the same sets of cells using manual annotation, SR-Tesseler and Clus-DoC. From left to right, 688 ± 136, 253 ± 86 and 643 ± 92 clusters in total. Each point represents 1 cluster; 15 cell profiles were measured. Bars represent mean ± SEM. All data represent at least three independent experiments. **** p<0.0001.

3.2.2 Calibration of photoswitching kinetics

As discussed in 3.1.3.2, to count the molecule number per cluster, I adopted the single-molecule calibration methods from Sieben et al. [227]. Using algorithms provided by Sieben et al. [227], I measured the localisation precision under my experiment setup and calculated the grouping parameters.

STORM imaging was first performed on isolated AlexaFluor 647 conjugated OKT4 antibody molecules. Images were reconstructed to follow the same protocol as other images in this study. Individual localisations were first grouped with a gap of 0 and a search radius of 30 nm to merge individual blink events. Next, localisations were grouped again with a gap time equal to the total acquisition time. This allowed the localisation precision σ_{xy} to be determined as ~15 nm (Figure 3.4). The dark time between individual photoswitching events could then be calculated.
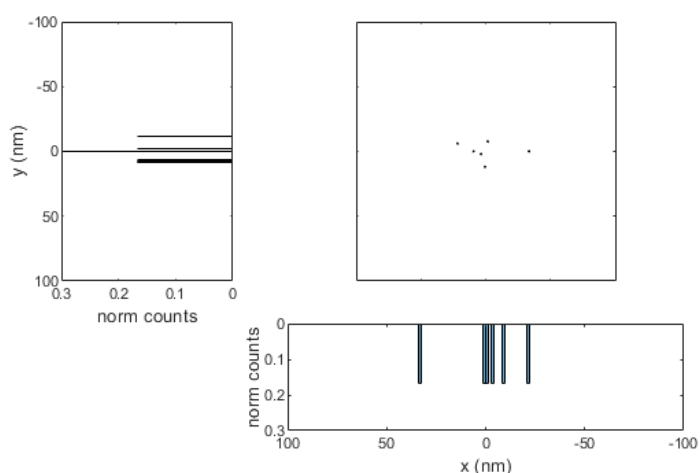
Figure 3.4 Experimentally obtained localisation precision for OKT4-AlexaFluor 647.

Average localisation precision with the optical and experimental setups. $\sigma_{xy} =$ ~15 nm.

The average on-time was 7.6 $\pm$ 1.4 frames and off-time was 7.8 $\pm$ 1.6 for immobilised OKT4-AlexaFluor 647 from 10 different FOVs (Figure 3.5). Experimentally determined localisation precision of 15 nm and the average dark-time 10 frames were used as calibration cut-offs. Thus, localisations identified from the same molecule were calibrated as a single position. In addition, this produced calibrated localisation maps for further molecular counting.
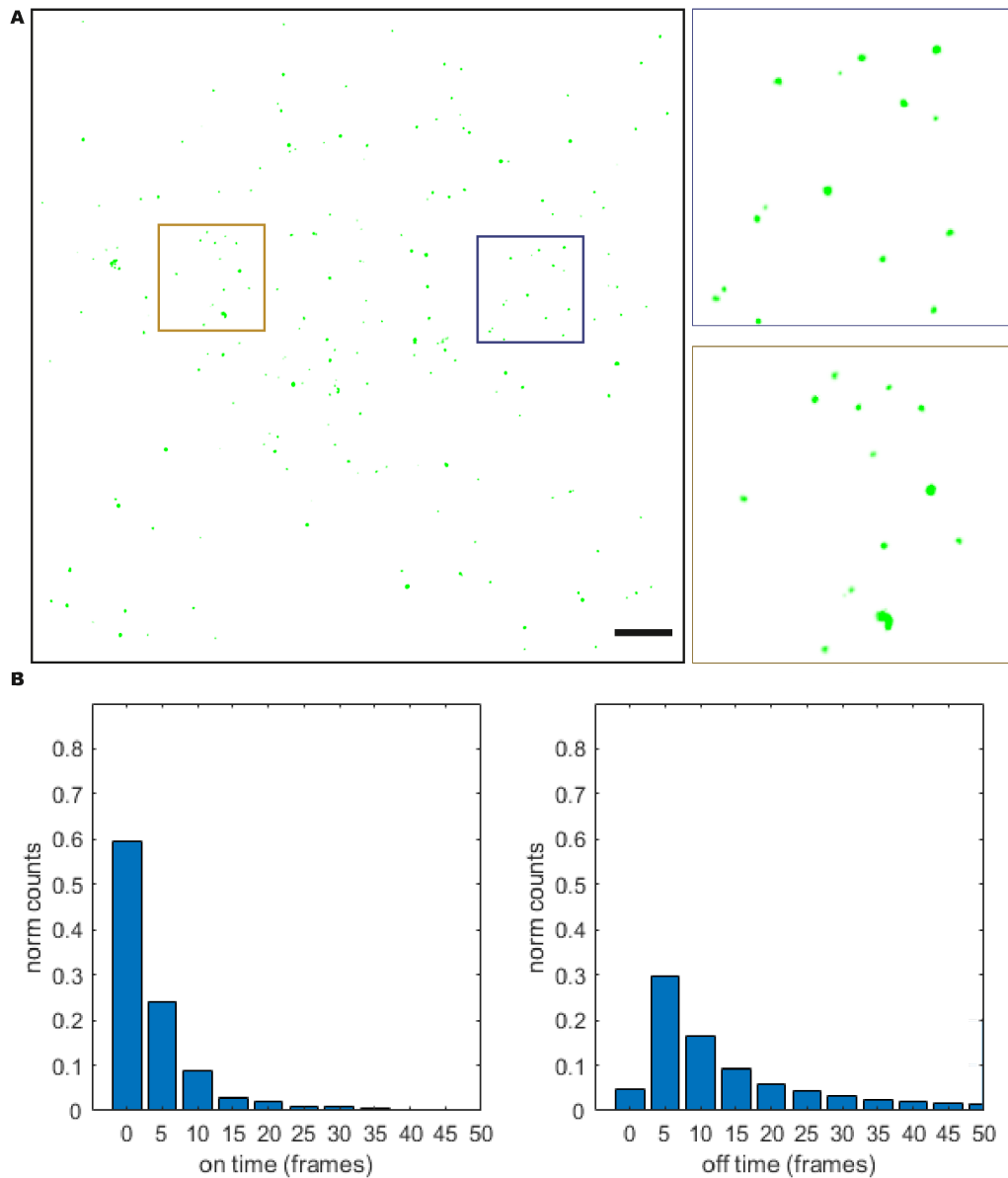
Figure 3.5 Calibration data for photoswitching kinetics and molecule counting.

A. Representative STORM image of immobilised OKT4-AlexaFluor 647 antibodies. Representative distribution of individual localisation on-time (B) and off-time (C) obtained. Scale bar = 2 μm.

3.2.3 Chromatic aberrations on beads imaged under 647 nm and 568 nm channels

As discussed in 3.1.3.3, to obtain precise spatial information between two channels, chromatic aberrations cannot be neglected in STORM imaging. I used images from fiducial bead-coated coverslips as references for estimating the transformation between channels in the experimental groups. Fiducial bead-coated coverslips were imaged for each experiment in both the 647 nm and 568 nm channels. Cross-channel alignment was performed using a chromatic aberration correction plugin developed by the Jalink lab (https://jalink-lab.github.io/).

Although the chromatic aberrations were negligible in the diffracted-limited images (Figure 3.6 TIRF panel), the STORM images showed apparent misalignment (Figure 3.6 Pre-processing Panel). Furthermore, this misalignment displayed a uniform pattern, indicating that it was caused by chromatic aberrations rather than drift. Fiducial beads imaged in both channels showed clear colocalisation post-processing as expected (Figure 3.6 Post-processing Panel). This localisation information collected from fiducial bead images was used as references for correcting the transformation between channels in the experimental groups. This correction was directly measured and applied to the sample localisation data (Figure 3.5).
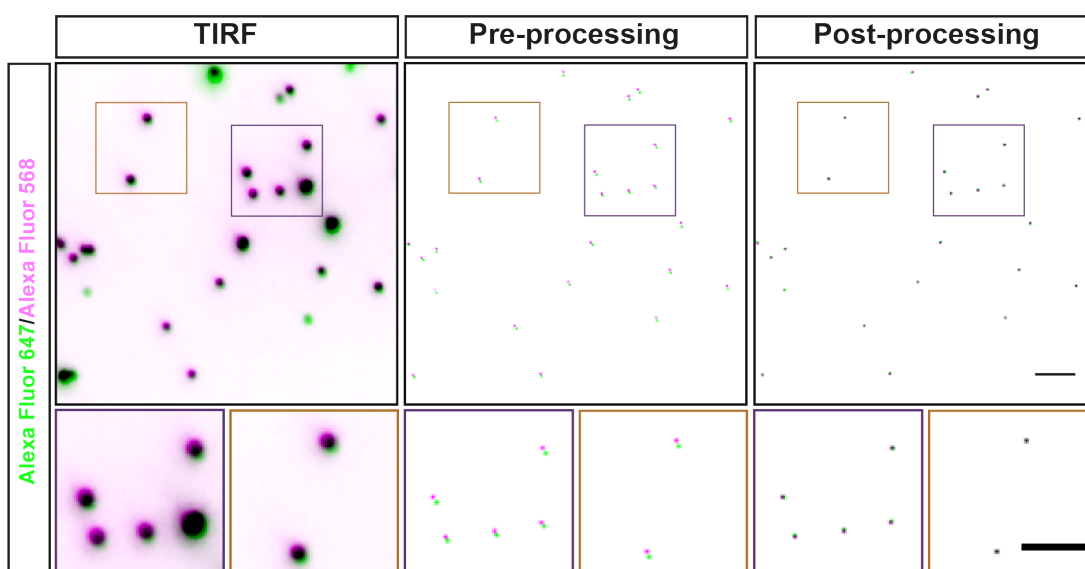
Figure 3.6 Chromatic aberrations on fiducial bead-coated coverslip images.

Representative TIRF (left) and pre-processing STORM (middle) images and insets of fiducial bead-coated coverslip. Examples of post-processing image; insets show the same FOV (right). Scale bar = 2 µm. Insets, Scale bar = 1 µm

Quantitatively, for the pre-processing groups of fiducial bead-coated coverslips, DoC scores were primarily 0, indicating no colocalisation between the AlexaFluor 647 and AlexaFluor 568 channels. After processing, all DoC scores calculated were larger than the set colocalisation threshold 0.4, which would be deemed perfect colocalisation by Clus-DoC (Figure 3.7 A and B). To quantify the percentage of colocalisation, in the pre-processing group, the percentage of colocalisation between beads imaged under AlexaFluor 647 to those under AlexaFluor 568 was $0.6 \pm 1\%$ whereas the number between beads under AlexaFluor 568 and beads under AlexaFluor 647 was $0.7 \pm 1\%$. By comparison, the percentage colocalisation in the post-processing group was $98 \pm 1\%$ and $99 \pm 1\%$, respectively (Figure 3.7 C and D). Therefore, the chromatic aberration performed and the colocalisation threshold chosen in this study were effective.
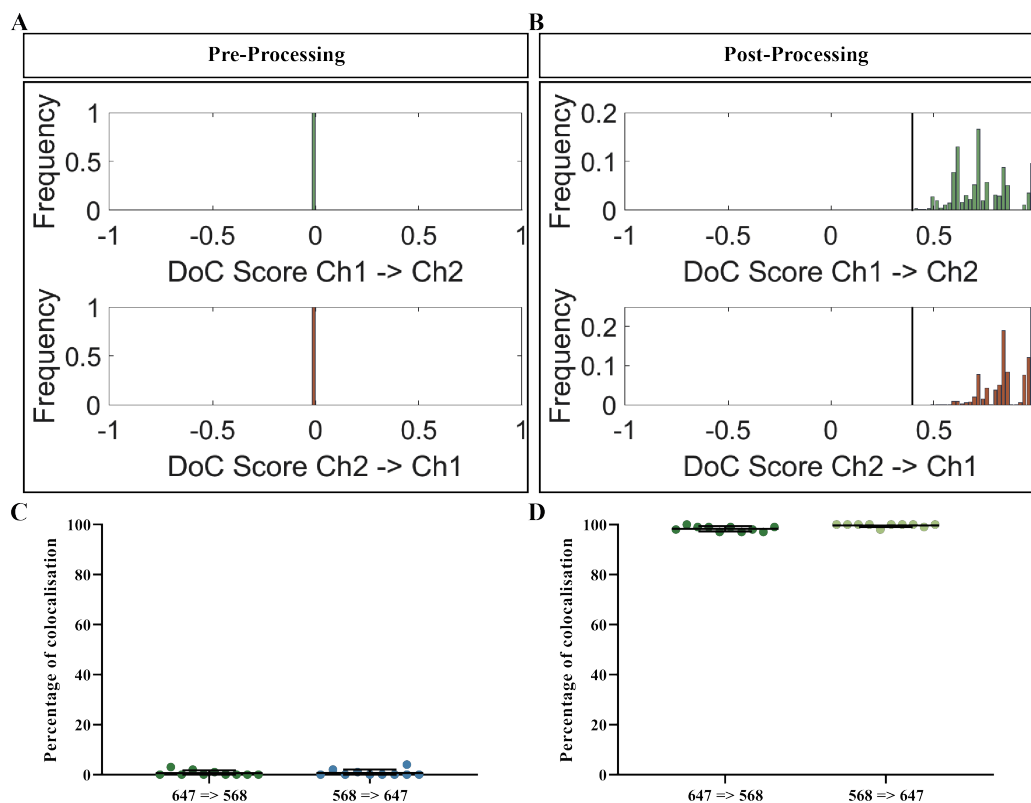
Figure 3.7 Validating cross-channel alignment and chromatic aberration corrections.

Distribution of DoC score of beads imaged under two channels in pre-processing (A) and post-processing (B) bead images. The black line indicates the threshold chosen, 0.4. (C & D) Percentage of colocalisation between two channels in pre-processing (C) and post-processing (D) images. Ch1 indicates beads imaged under AlexaFlour 647; Ch2 indicates beads imaged under AlexaFlour 568. Each point represents one FOV of fiducial beads. Bars represent mean ± SD. All data represent at least three independent experiments.

3.2.4 Quantitative analysis of CD4 clusters in pre- and post-fixation labelling

After the quantitative analysis pipeline was established, I then moved to validate several labelling conditions. First, although 4°C incubation was used in this experiment to minimise membrane fluidity and trafficking, the extent of

antibody crosslinking in pre-fixation labelling has not been validated. The OKT4 epitope intended to be used in this study is damaged by aldehyde fixation [81]. Therefore, to validate the extent of antibody crosslinking in pre- and post-fixation labelling conditions, I selected neutralising anti-CD4 bivalent antibody Q4120, which can be used in pre- and post-fixation conditions. SupT1-R5 cells, a human non-Hodgkin lymphoma CD4+ T-cell line with stable CCR5 expression, were co-incubated with 6 μg/ml Q4120 at 4°C for 1hour before fixation with 4% PFA. In addition to using a low temperature for labelling, antibody-induced receptor dimerization was further minimised by using an excess amount of antibody which should favour monovalent binding. As the control, for the post-fixation condition, SupT1-R5 cells were fixed in 4% PFA for 10min before Q4120 incubation at 4°C. Cells in both conditions were then incubated with the fluorophore conjugated secondary antibody and imaged (Figure 3.8). Based on reconstructed images in both conditions, CD4 was seen in numerous clusters homogeneously distributed across the field of view (FOV) (Figure 3.8), which appears to be small groups of molecules in both pre- and post-fixation labelling conditions.
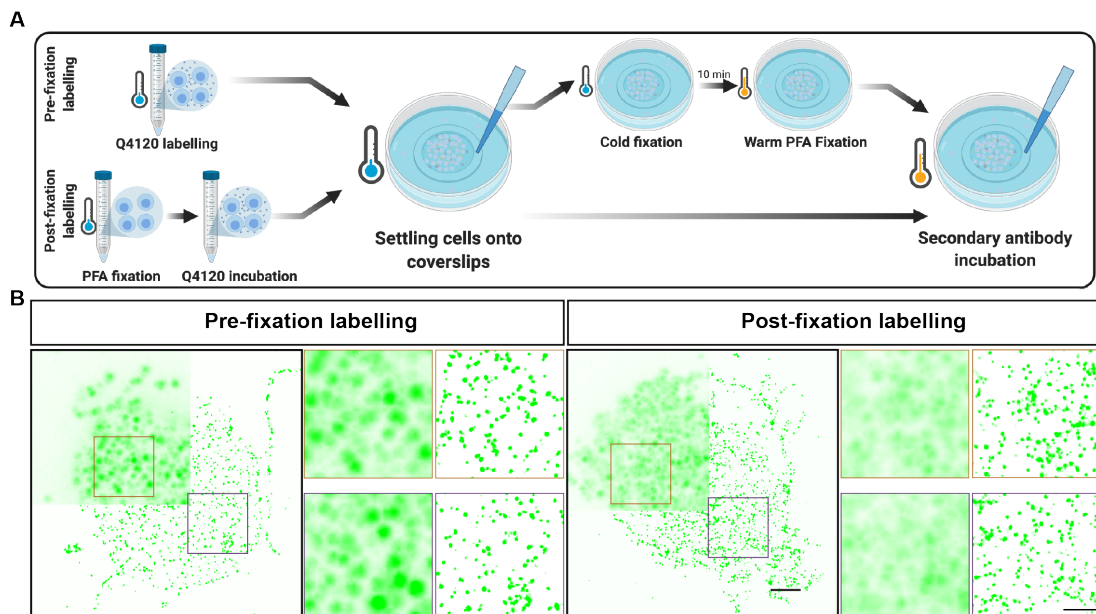
Figure 3.8 Plasma membrane CD4 distribution following pre- and post-fixation Q4120 labelling.

A. Schematic of the experimental pipeline used. SupT1-R5 cells were pre-incubated at 4°C with Q4120 or PFA fixed before being incubation with Q4120 at 4°C. B. Representative diffraction-limited TIRF (top left quarter) and TIRF-STORM (bottom) images of CD4 pre-/post fixation in untreated SupT1-R5 cells. Scale bar = 2 μm. Insets show magnified TIRF and TIRF-STORM images of the indicated regions. Scale bar = 1 μm.

To validate the effect of pre-fixation labelling on CD4 distribution quantitatively, clusters were analysed by Clus-DoC. CD4 was labelled with monoclonal antibody Q4120 and AlexaFluor 647 conjugated secondary antibody pre- and post-fixation. I characterised the diameters of identified clusters and the distribution of molecules per cluster. In the pre-fixation labelling condition, 821 ± 97 clusters per ROI were identified with a mean diameter of 63 ± 30 nm. In comparison, the number of CD4 clusters identified in post-fixation labelling was 881 ± 117 clusters per ROI with 63 ± 28 nm in diameter (Figure 3.9 A). When counting the molecules on the calibrated coordinate maps, the majority (70%) of CD4 clusters were composed 1 to 4 CD4 molecules with no significant difference between groups (Figure 3.9 B). The molecular counting results confirmed my qualitative assessment that pre-fixation labelling did not alter the CD4 membrane distribution.
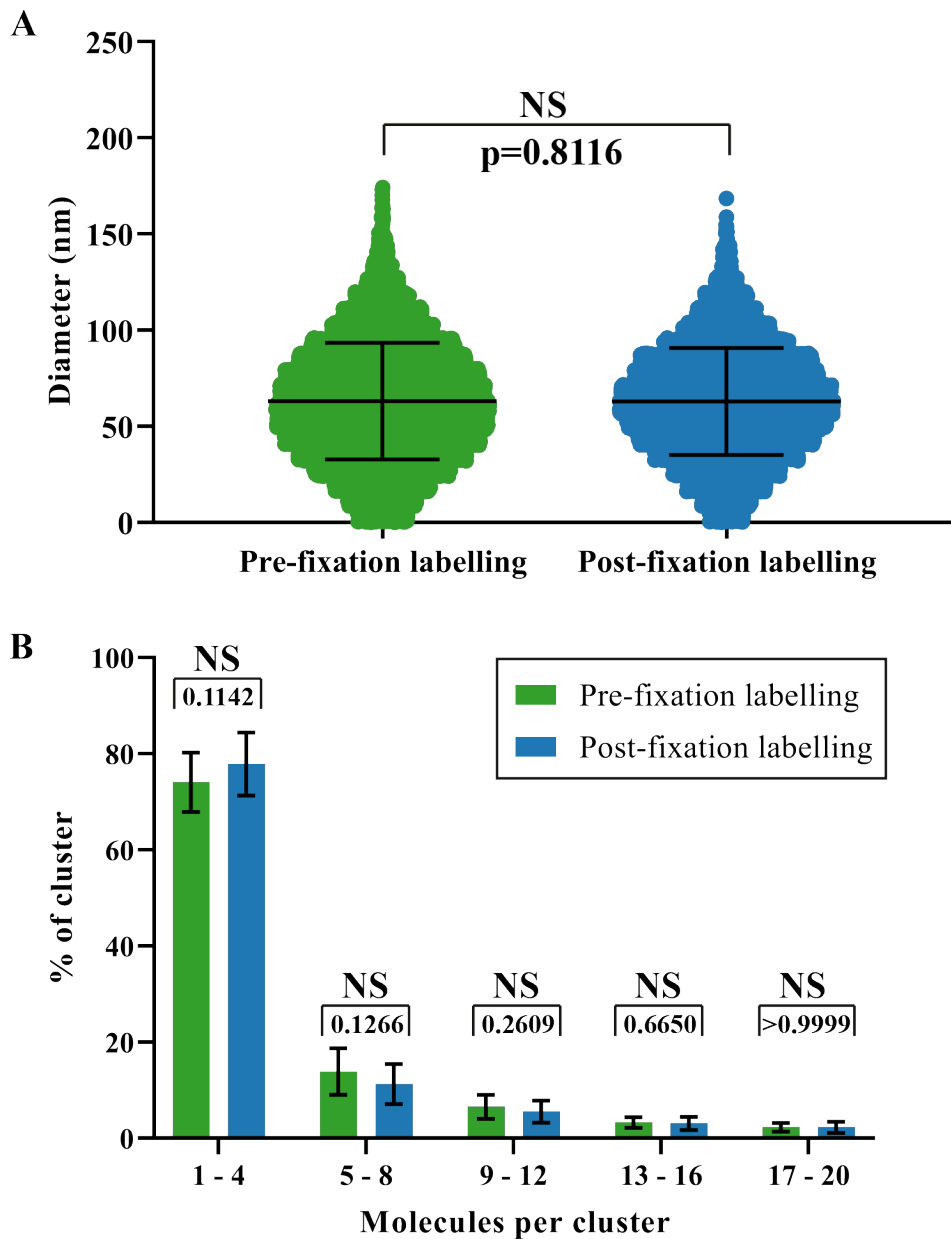
Figure 3.9 CD4 cluster diameter and molecule numbers in pre- and post-fixation labelling.

A. Cluster diameters in pre- and post-fixation Q4120 CD4 labelling. In total, 821 ± 97 and 881 ± 117 clusters were plotted. Each point represents 1 cluster; 15 cell profiles were measured. B. Molecule counting of CD4 clusters in pre- and post-fixation labelling. 15 cell profiles were measured. Bars represent mean ± SD. All data represent at least three independent experiments.

3.2.5 Visualisation of PM CD4 organisation with single and double labelling

The addition of fluorophore-conjugated secondary antibodies in immunolabelling can increase imaging sensitivity by signal amplification due to multiple secondary antibodies binding to a single primary antibody (double labelling) (Figure 3.10 A). However, the use of primary and secondary antibody labelling complex will reduce the imaging fidelity in the imaging system by increasing the size of the antibody/antigen complex. Moreover, it will increase the number of false-positive localisations detected in the quantitative analysis. Therefore, labelling CD4 with fluorophore-conjugated primary antibody (single labelling, Figure 3.10 B) is optimal in the study when labelling efficiency is not lowered.

To visualise and compare CD4 distribution in single and double labelling conditions, for single labelling samples, I have incubated SupT1-R5 cells with AlexaFluor 647 conjugated OKT4 at 4°C before settling the cells onto coverslips, fixation and TIRF-STORM imaging. AlexaFluor 647 conjugated OKT4 was generated via NHS-ester chemistry. The calculated dye-to-protein molar ratio was about 1.7, close to 1 fluorophore per antibody. With double labelling samples, SupT1-R5 cells were incubated with OKT4 at 4°C, deposited onto coverslips and fixed as for the single labelling condition. AlexaFluor 647 conjugated goat anti-mouse secondary antibody was then added to samples for 15min at RT. The samples were then washed, and a second round of fixation was performed before TIRF-STORM imaging.

Reconstructed TIRF-STORM imaging shows no apparent difference in labelling density between single and double labelling conditions using anti-CD4 antibody OKT4 (Figure 3.10 B). However, comparing double labelling using the neutralising anti-CD4 antibody Q4120 and the non-neutralising anti-CD4 antibody OKT4, a slight decrease in CD4 density was visible (Figure 3.8), which indicated that OKT4 has a lower binding efficiency compared to Q4120. Nevertheless, single OKT4 labelling was comparable to OKT4 double labelling.
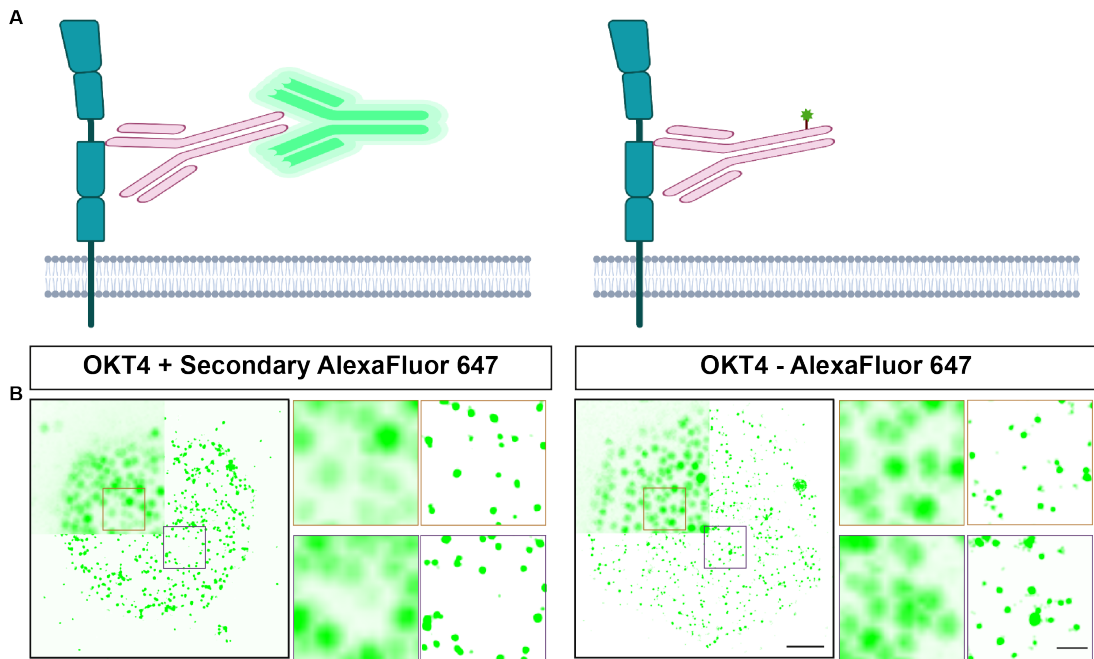
Figure 3.10 Visualisation of CD4 distribution with double and single labelling.

A. Schematic of OKT4 double labelling (left) and OKT4 single labelling. B. Representative diffraction-limited TIRF (top left quarter) and TIRF-STORM (bottom) images of OKT4 double labelling (left) and OKT4 single labelling (right) in untreated SupT1-R5 cells. Scale bar = 2 µm. Insets show magnified TIRF (left) and TIRF-STORM (right) images of the indicated regions. Scale bar = 1 µm.

I quantitatively analysed CD4 cluster diameter and molecule numbers per cluster in both conditions. In the single labelling condition, 593 ± 92 CD4 clusters per ROI were identified with a mean diameter of 59 ± 21 nm. By comparison, clusters identified in double labelling conditions were 591 ± 152 per cell profile and had a mean diameter of 61 ± 24 nm and (Figure 3.10 A). Generally, primary antibody labelling identified a similar number of clusters per ROI with a close cluster size (Figure 3.11 A).

Most CD4 clusters identified in both conditions still consisted of 1-4 CD4 molecules per cluster. However, more clusters containing 5-8 molecules were seen in double labelling condition. The single labelling condition had fewer

clusters containing 5-8 clusters per smaller clusters diameters (Figure 3.11 B). Thus, according to the number of clusters identified, the number in single labelling condition did not significantly different to double labelling condition. The single labelling was, therefore, suitable for subsequent studies.
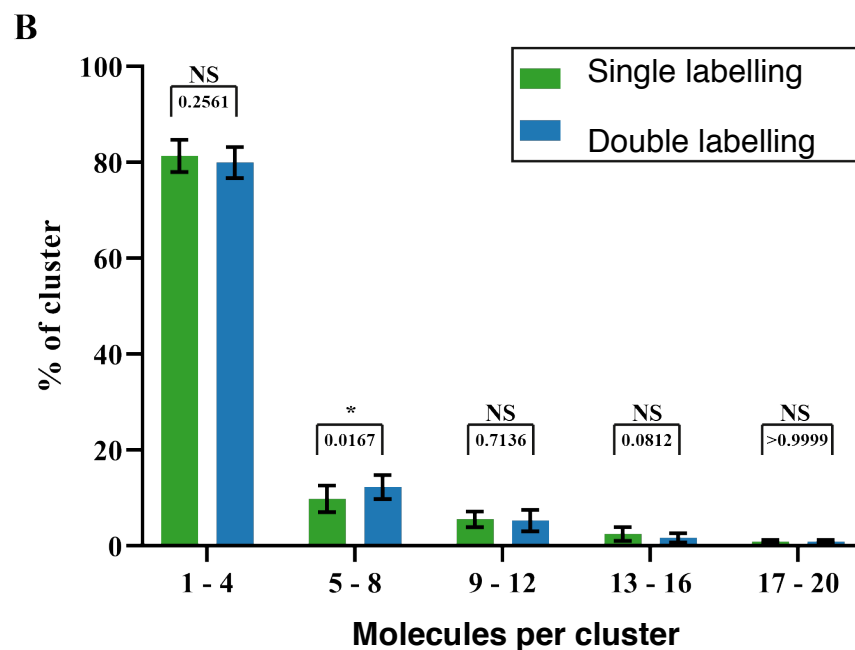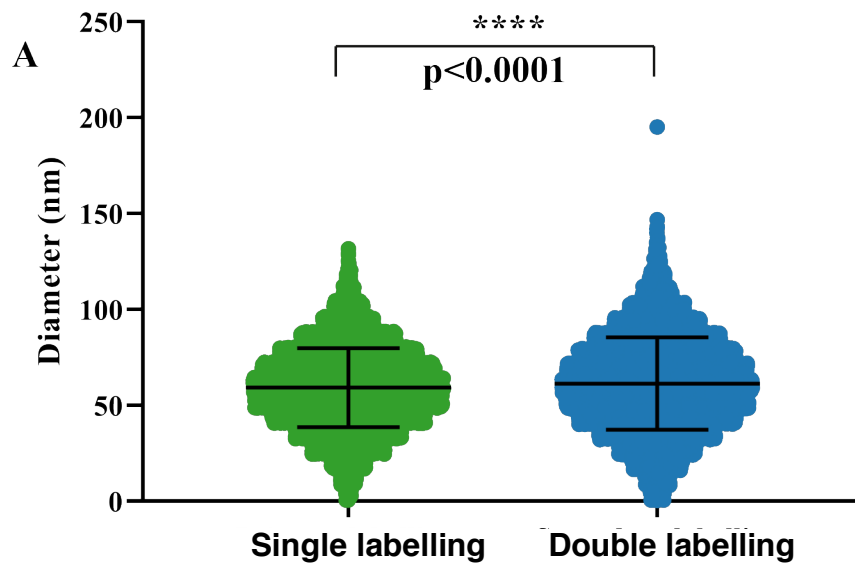
Figure 3.11 Analysis of CD4 cluster diameter and molecule numbers using single and double labelling.

A. Cluster diameters in single labelling and double labelling. 593 ± 92 and 591 ± 152 were plotted. Each point represents 1 cluster; 15 cell profiles were measured. B. Molecule counting of CD4 clusters in single and double labelling. 15 cell profiles were measured. Bars represent mean ± SD. All data represent at least three independent experiments. * p<0.05.

3.2.6 Analysis of the effect of 37°C incubation at timepoints before fixation on CD4 organisation on the plasma membrane

Although the crosslinking caused by bivalent antibodies under cold conditions is minimal (Figure 3.8 and Figure 3.9), this study aims to capture the HIV fusion process, most of which happens at a timescale of 0 - 15min at 37°C [262–265]. Therefore, 37°C incubation before fixation was a necessary step in the experiments.

To further validate whether CD4 organisation was impacted by antibody crosslinking during 37°C incubation, I incubated OKT4-AlexaFluor 647 with SupT1-R5 cells and then allowed the cells to adhere to coverslips as before. Samples were made for three conditions, 1) direct fixation (Timepoint 0min), 2) 1min 37°C incubation (Timepoint 1min) and 3) 15min 37°C incubation (Timepoint 15min) before fixation (Figure 3.12 A). According to the TIRF-STORM reconstructed images, CD4 was organised homogeneously as clusters on the PM in all timepoints. No differences were observed in CD4 distribution among groups (Figure 3.12 B).
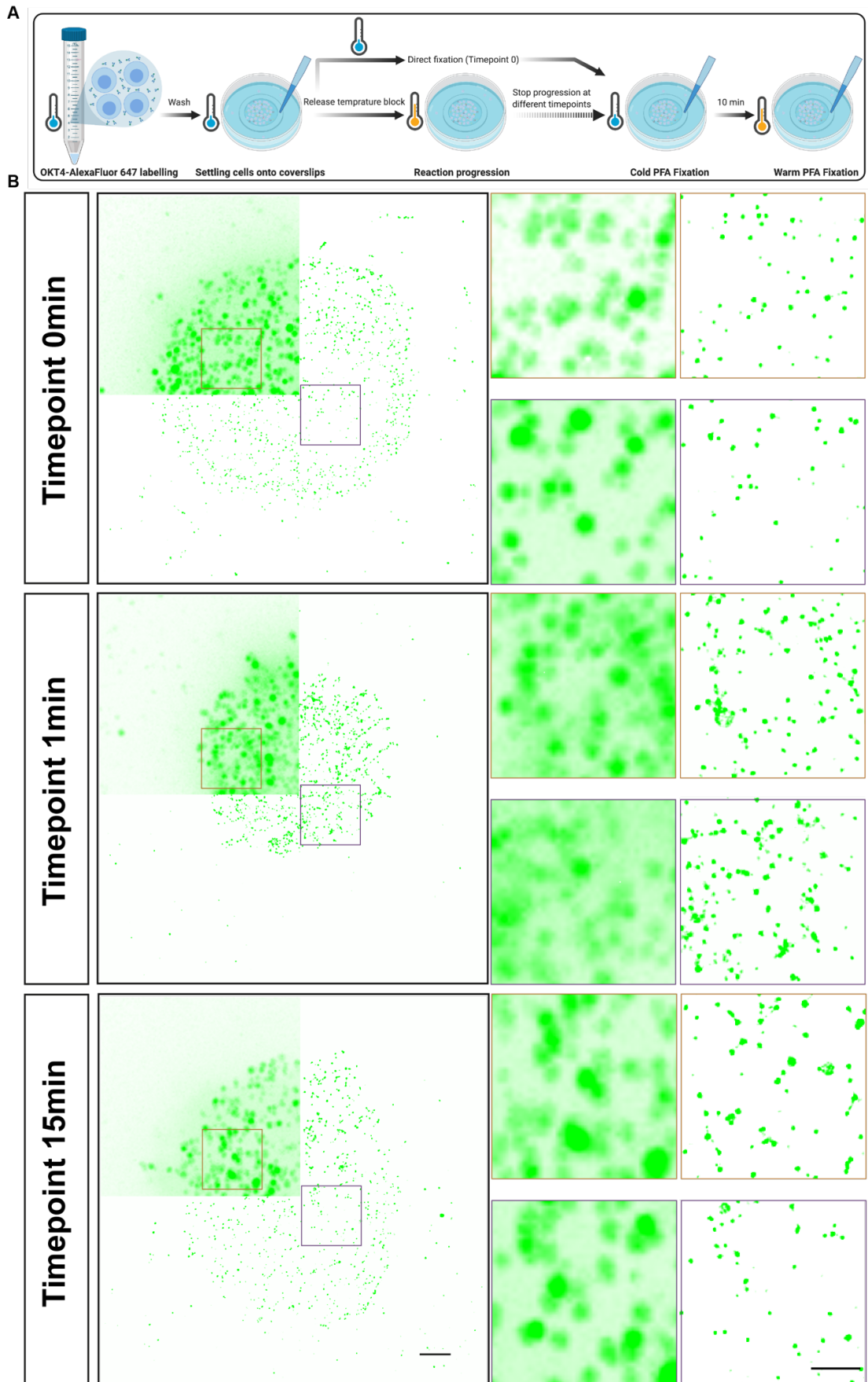
Figure 3.12 Visualising the effect of 37°C incubation at timepoints on CD4 distribution.

A. Experimental workflow for samples fixed at 0min, or 1min and 15min after 37°C incubation. B. Representative diffraction-limited TIRF (top left quarter) and TIRF-STORM (bottom) images of CD4 distribution. Scale bar = 2 μm. Insets show magnified TIRF (left) and TIRF-STORM (right) images of the indicated regions. Scale bar = 1 μm.

As for quantifying CD4 organisation, 666 ± 112, 645 ± 88 and 702 ± 123 clusters per ROI were detected in 0min, 1min and 15min 37°C incubation condition, respectively. There was no significant difference in CD4 cluster diameters among 0min (62 ± 0.20 nm), 1min (62 ± 0.16 nm) and 15min (62 ± 0.18 nm) 37°C incubation conditions (Figure 3.13 A).

When the data were broken down to generate molecule numbers, subtle changes were seen. The majority of clusters still contained 1-4 CD4 molecules in all three conditions. No difference in the number of CD4 clusters containing 9-20 molecules was seen for the three conditions. For clusters containing 1-4 molecules, there were more clusters containing 1-4 molecules post 1min 37°C incubation than 0min and 15min incubation. 5-8 molecules in 0min 37°C incubation condition was slightly more than those in 1min 37°C incubation (Figure 3.13 B).
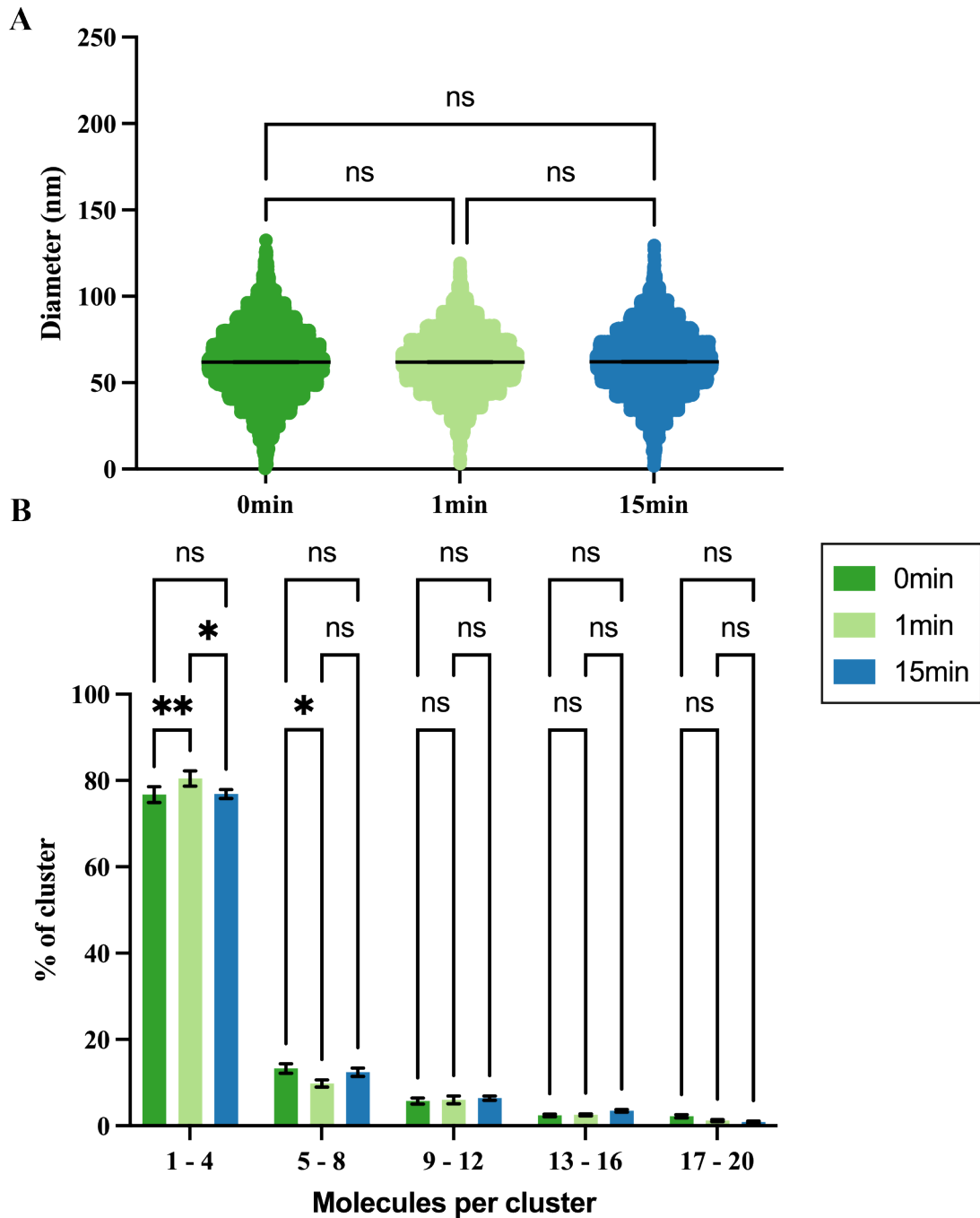
Figure 3.13 CD4 cluster diameter and molecule numbers following incubation at 37°C incubation.

A. Cluster diameters in 0min, 1min and 15min 37°C incubation conditions. 666 ± 112, 645 ± 88 and 702 ± 123 clusters were plotted in total. Each point represents 1 cluster; 15 cell profiles were measured. B. Molecule counting of CD4 clusters following 37°C incubation. 15 cell profiles were measured. Bars

represent mean ± SEM. All data represent at least three independent experiments. * p<0.05, ** p<0.01.

3.2.7 Analysis of the spatial relationship between CD4 and CCR5

To ensure the observed spatial relationship in dual colour labelling under both 647 nm and 568 nm channels was fluorophore-independent, colour-swap experiments were performed. CD4 and CCR5 were used as references for the experiments. Neutralising anti-CCR5 monoclonal antibody MC5 was used for CCR5 labelling. Before settling SupT1-R5 cells onto coverslips and fixation, cells were co-incubated with OKT4-AlexaFluor 568 and MC5-AlexaFluor 647 at 4°C for 1hour. Similar small clusters of CD4 and CCR5 were visualised in single-colour images, with little obvious co-localisation (Figure 3.14).
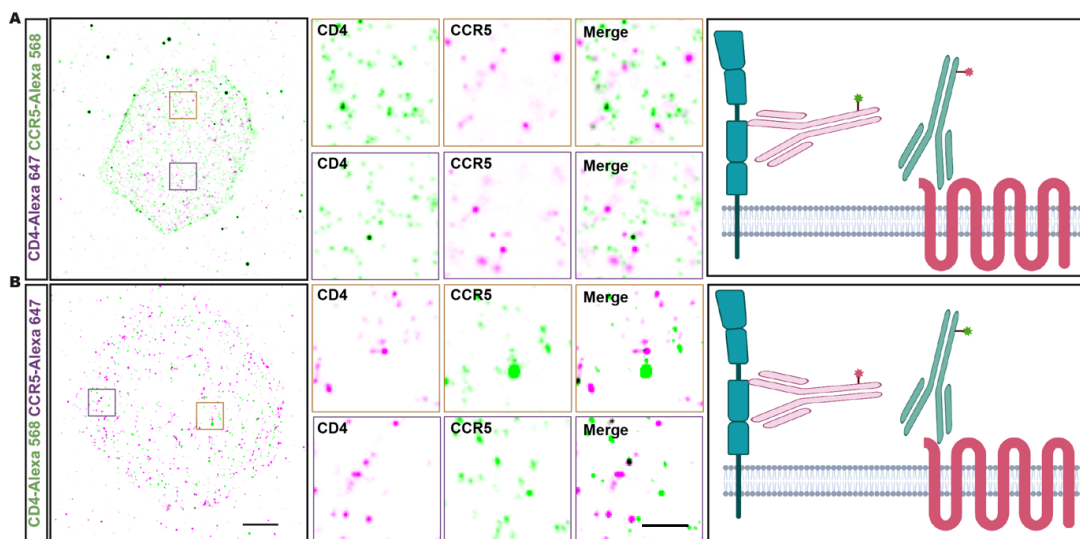
Figure 3.14 Analysis of the spatial distribution of CD4 and CCR5 using dual-colour TIRF-STORM imaging.

A. Representative image and schematic of CD4-AlexaFluor 647 and CCR5-AlexaFluor 568 labelling. B. Representative image and schematic of CD4-AlexaFluor 568 and CCR5-AlexaFluor 647 labelling. Scale bar = 2 µm. Insets show magnified STORM images of the indicated regions. Scale bar = 1 µm.

I validated CD4 and CCR5 cluster diameter in the colour swap experiment. For CD4, 654 ± 68 and 579 ± 109 clusters were identified per ROI in AlexaFluor 647 labelled and AlexaFluor 568 labelled conditions, respectively. The diameters measures were 66 ± 19 nm and 67 ± 30 nm, respectively. As with CCR5, 312 ± 67 and 284 ± 101 clusters per ROI were measured in AlexaFluor 647 labelled and AlexaFluor 568 labelled conditions, and the cluster diameter was 109 ± 23 nm and 109 ± 43 nm, respectively (Figure 3.15 A). Thus, neither dual-colour labelling nor different fluorophore labelling introduced artefacts into cluster diameter measurements.

I then quantitatively characterised the spatial relationship between CD4 and CCR5 in untreated SupT1-R5 cells. As expected, no differences were found for different fluorophore labelling conditions. In detail, when comparing CD4 to CCR5, the percentage of colocalisation was 8 ± 2% and 7 ± 2% with AlexaFluor 647 labelled CD4 and Alexa 568 labelled CD4 (Figure 3.15 B). The average cluster diameter in the colocalised (57 ± 17 nm *vs* 63 ± 5 nm) and non-colocalised areas (53 ± 11 nm *vs* 70 ± 20 nm) remained similar regardless of the fluorophore used (Figure 3.15 C). As for CCR5 to CD4, the percentage of colocalisation remained low (AlexaFluor 647, 5 ± 2% *vs* AlexaFluor 568, 4 ± 2%). After quantifying the cluster diameter, no difference was shown between colocalised (102 ± 19 nm *vs* 118 ± 21 nm) and the non-colocalised areas (99 ± 11 nm *vs* 104 ± 15 nm) in the two fluorophore labelled groups (Figure 3.15 D).
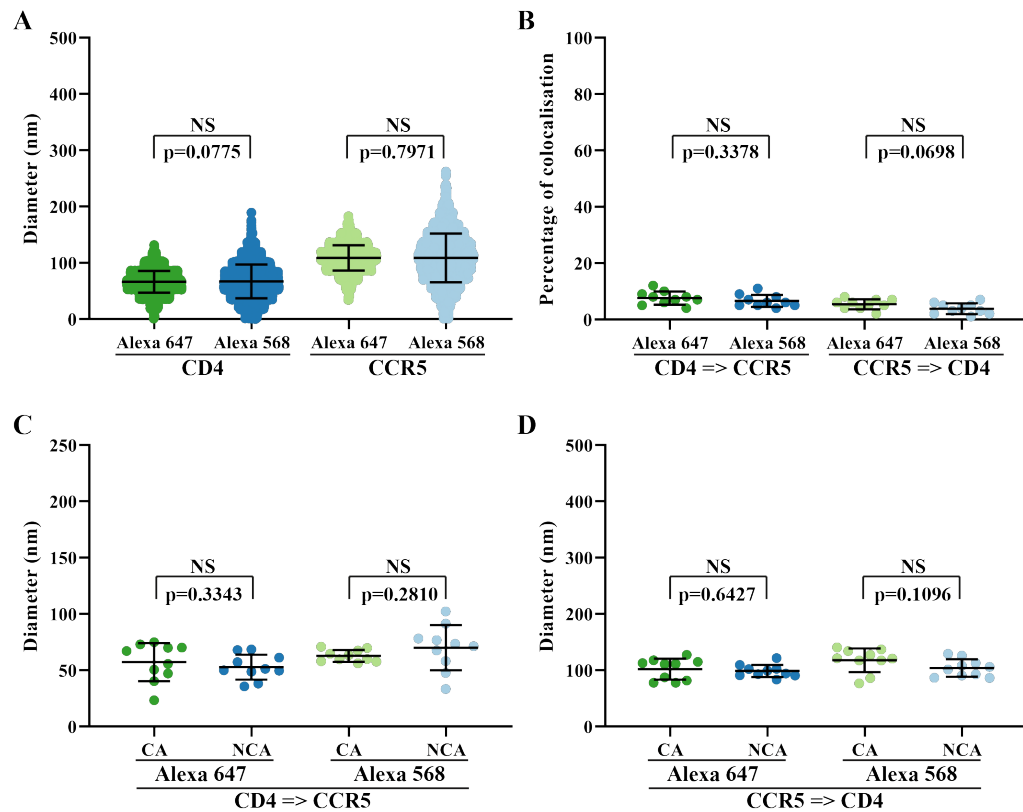
Figure 3.15 Quantitative analysis of cluster diameters and spatial relationship between CD4 and CCR5 on dual-colour labelled untreated SupT1-R5 cells.

A. CD4 and CCR5 cluster diameters labelled by both fluorophores. Each point represents a cluster. B. Percentage of colocalisation between CD4 => CCR5 and CCR5 => CD4 in both fluorophore labelling conditions. Each point represents the average of a cell profile. Comparison of the cluster diameters between colocalised and non-colocalised areas in both fluorophore labelling conditions between CD4 => CCR5 (C) and CCR5 => CD4 (D). Each point represents the average per a cell. 10 cell profiles were included. Bars represent mean ± SD. All data represent at least three independent experiments.

In this section, I quantitatively analysed the colour swap experiments. I found that labelling with different fluorophores does not introduce artefacts into the pipeline used in this study. The quantitative analysis further confirms that CD4

and CCR5 showed little colocalisation in untreated cells with no difference in cluster diameter in colocalised and non-colocalised areas.

3.2.8 Analysis of CD4 organisational changes after PMA treatment

To ensure I could detect potential changes in the distribution of CD4 using this visualisation pipeline, I investigated the effect of PMA stimulation on SupT1-R5 cells. PMA triggers endocytic uptake of CD4 and drives bulk CD4 redistribution on the plasma membrane [81]. Cells were prelabelled with OKT4-AlexaFluor 647 and deposited on coverslips at 4°C as before (Figure 3.16 A), and subsequently warmed to 37°C by addition of pre-warmed media containing PMA or a non-active analogue (4α-PMA) as a control treatment for 0 or 15min (Figure 3.15 A). The cells were then fixed and processed for imaging.

In the 0min PMA treated group, CD4 was distributed as small clusters similar to those in untreated SupT1-R5 cells (Figure 3.16 B). Likewise, CD4 distribution in 0min 4α-PMA treated cells displayed a homogeneous distribution (Figure 3.16 B). However, 15min PMA treatment elicited striking changes in SupT1-R5 cells (Figure 3.16 B); CD4 was heterogeneously distributed across the PM with clearly visible large clusters. No such reorganisation was observed for cells treated with 4α-PMA for 15min (Figure 3.16 B).
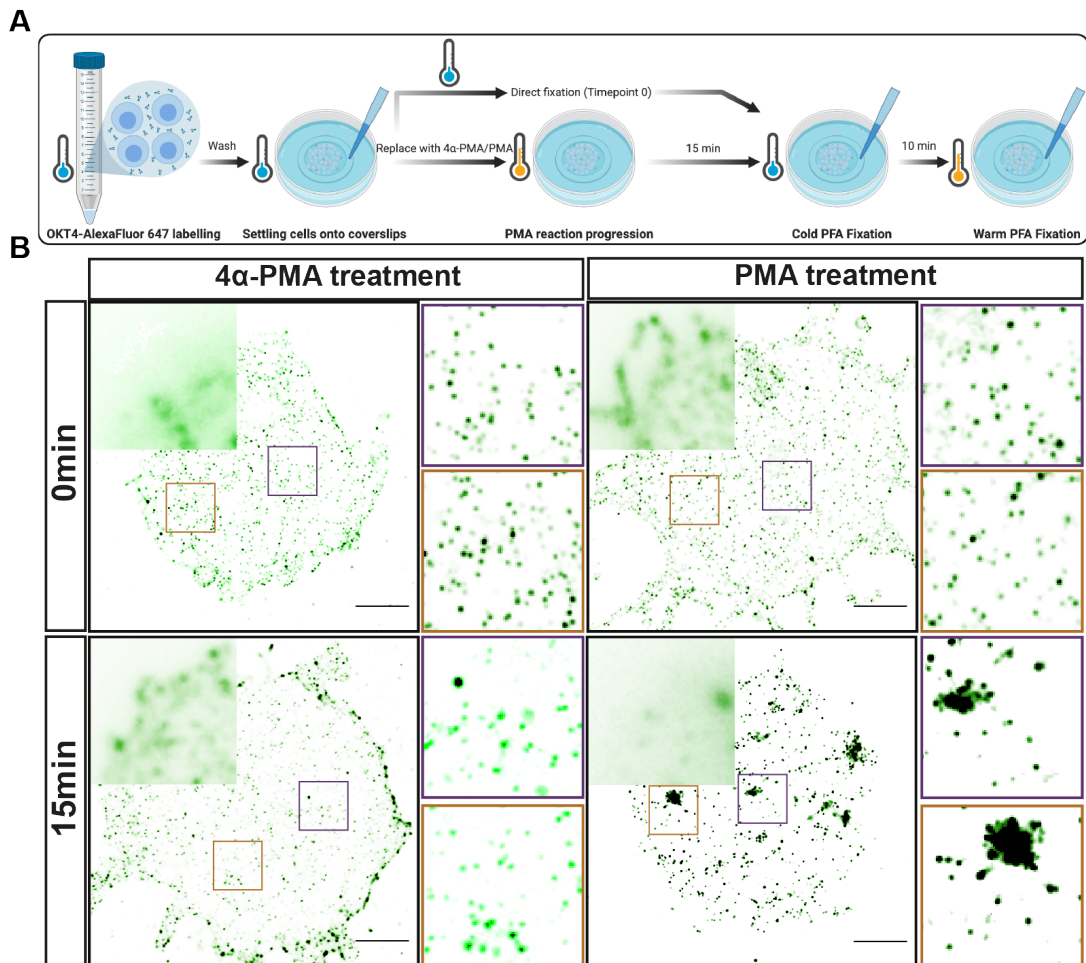
Figure 3.16 CD4 reorganisation in response to PMA and 4α-PMA.

A. Schematic of the sample preparation for 0 and 15min post PMA treatment.
B. Representative TIRF (top left corner) and TIRF-STORM (bottom) images of
CD4 on SupT1-R5 cells following treatment for 0min (top) or 15min (bottom)
with 4α-PMA (left) or PMA (right). Scale bar = 2 μm. Insets show magnified
TIRF-STORM images of the indicated regions. Scale bar = 1 μm.

To determine if the quantitative analysis pipeline I have established can
robustly detect changes in membrane protein organisation, I analysed CD4
clusters on PMA treated SupT1-R5 cells. The lowest number of clusters was
identified after 15 min PMA treatment (203 ± 132 clusters) compared to the
rest (0min 4α-PMA, 634 ± 67; 15min 4α-PMA, 600 ± 92; 0 min PMA, 591 ± 97
clusters). Quantification of the CD4 cluster size revealed a clear increase in
cluster diameter (112 nm ± 2.34 nm; Figure 3.16 A) in 15min PMA treatment

condition. Furthermore, larger CD4 clusters of up to 800 nm were also seen (Figure 3.17 A). An increase in cluster size was not detected in cells fixed immediately following PMA addition, nor in those treated with non-stimulatory 4α-PMA (Figure 3.17 A).

Outputs from molecular counting indicated that PMA induced an increase in the number of CD4 molecules per cluster (21–100 molecules per cluster; an average of 38 ± 73) and, strikingly, a small number of clusters with as many as 500 molecules were shown (Figure 3.17 B). Meanwhile, the distribution of molecule numbers per cluster remained unchanged in 0min 4α-PMA and PMA treatment, 15min 4α-PMA treatment conditions.
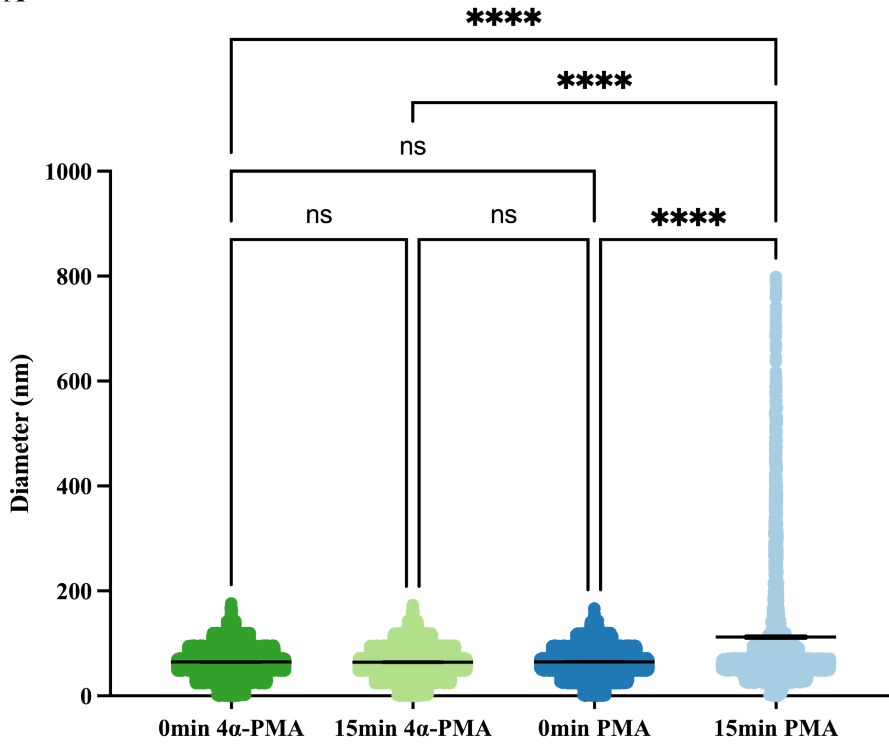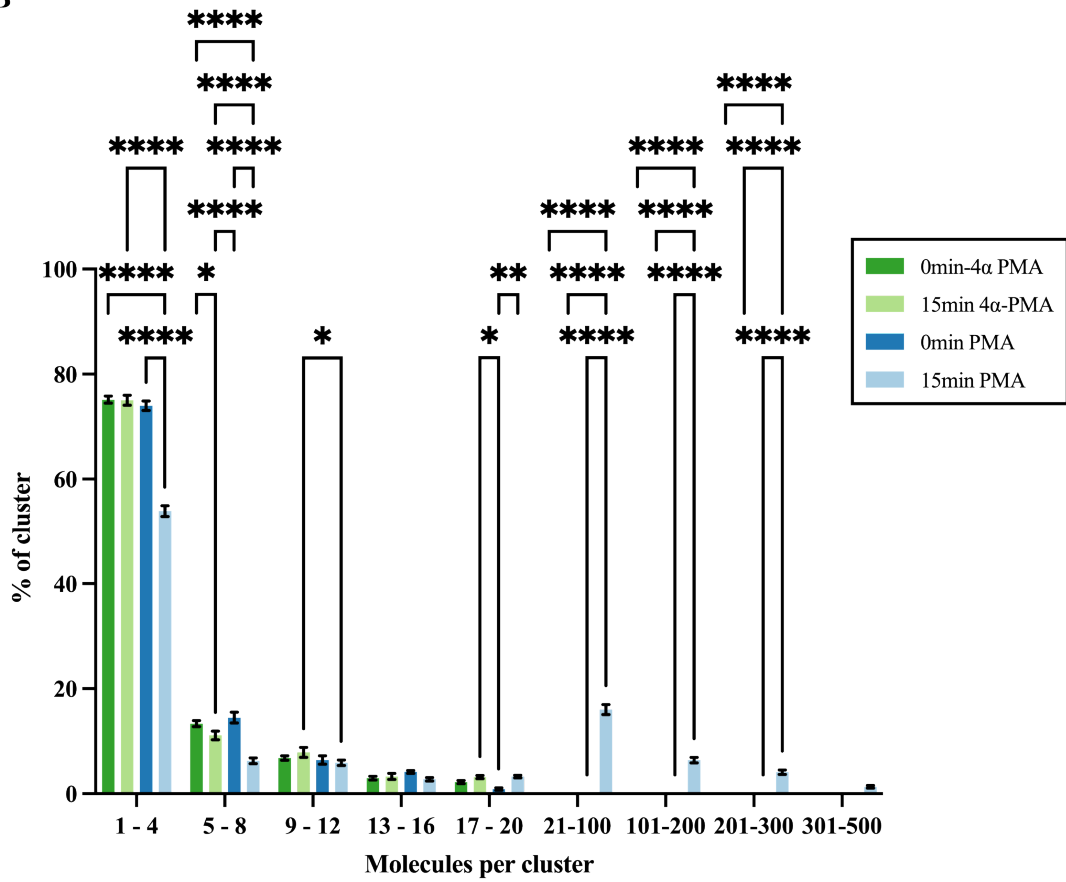
Figure 3.17 Analysis of CD4 cluster parameters following PMA treatment.

A. Quantification of CD4 cluster diameters; In total, 241 ± 77, 276 ± 72, 258 ± 64 and 106 ± 89 clusters were plotted. Each point represents the diameter of individual clusters. (B) Molecular counting of CD4 clusters. Each bar represents the mean cluster fraction displaying the indicated range of molecules per cluster. Data are representative of at least three independent experiments. 15 cell profiles were measured per condition. Bars represent mean ± SEM. ** $p < 0.01$; **** $p < 0.0001$.

These results indicated the experimental pipeline I have established can detect changes in CD4 organisation as indicated by cluster diameter and the number of molecules per cluster.

3.2.9 Statistical simulations of CD4 distribution on untreated SupT1-R5 cells

Although the pipeline I established can detect changes induced by chemical treatment, it does not indicate whether the CD4 clusters identified in the untreated condition are randomly distributed. Therefore, I used a theoretical Poisson statistical model to calculate the distribution of the number of molecules per cluster that might be expected from a random distribution of receptors on the cell surface. The average theoretical Poisson distribution was generated from the different cluster sizes measured experimentally and compared with the experiment data (Figure 3.18 A). For modelling purposes, CD4 surface densities (n) of 60 molecules/μm^2, 200 molecules/μm^2 and 300 molecules/μm^2 were used, based on the number of CD4 molecules per cell reported for SupT1 cells [183,191] (Figure 3.18 B, C, D).

The experimental data showed a similar trend in untreated cells with the modelled distribution regardless of the CD4 surface density used (Figure 3.18 B, C, D). Furthermore, the distribution pattern of the number of CD4 molecules per cluster from the experimental data was similar to the modelled distribution, indicating that CD4 distribution is likely to be random. Of the three conditions

modelled, the distribution with the density of 200 molecules/µm² best represented the experimental acquired distribution of molecules per CD4 cluster (Figure 3.18 C).
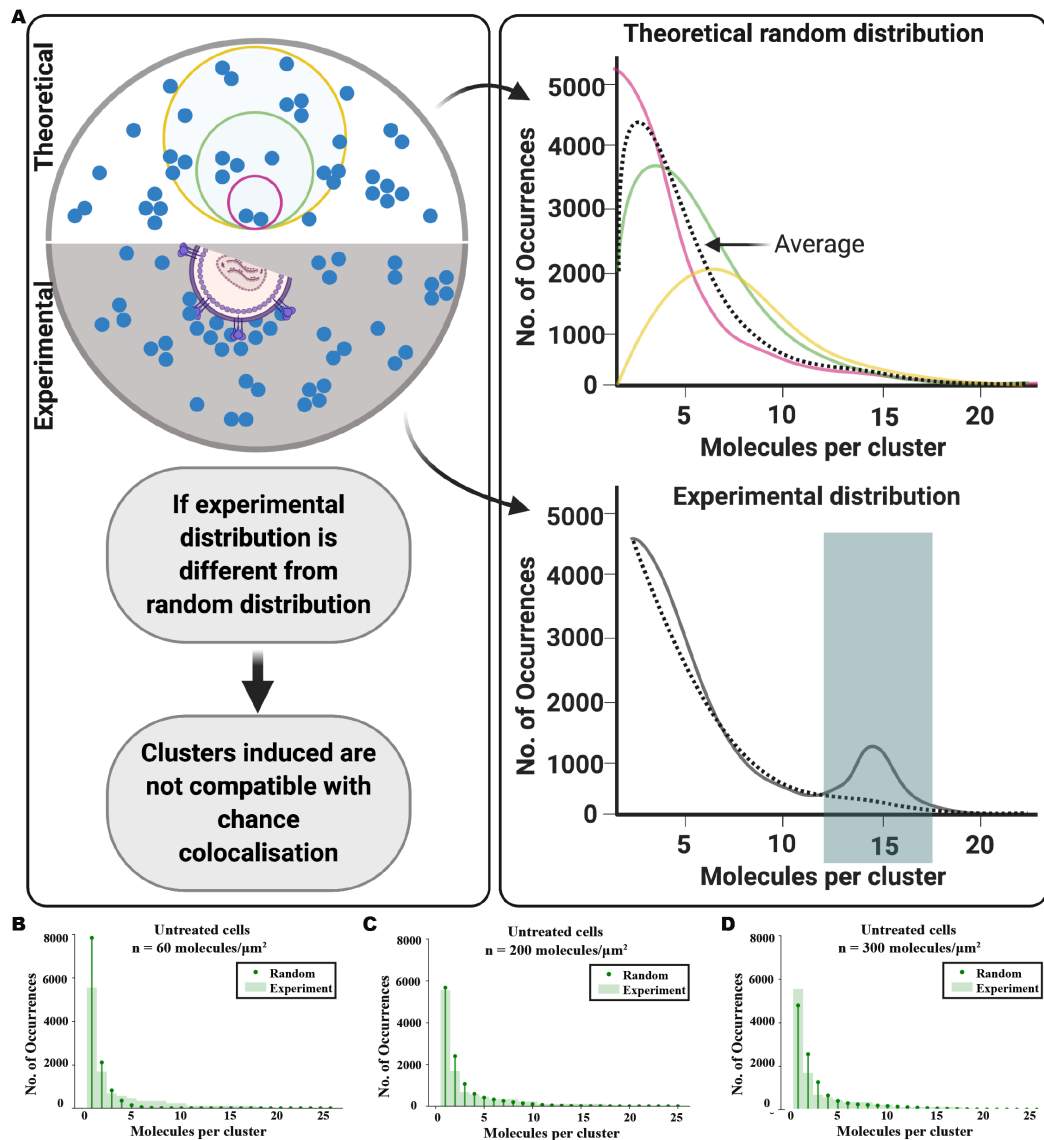
Figure 3.18 Statistical modelling of CD4 surface distribution.

A Model schematic (Top): counting CD4 molecules (blue) in membrane areas of different sizes (small (pink), medium (green) or large (yellow)) compared to a theoretical model based on an averaged Poisson distribution that corresponds to a random distribution of receptors on the cell surface and to multiple measurements in membrane areas (clusters) of different sizes (the black line is the average of Poisson distributions for different cluster sizes [pink,

green, yellow]). Bottom: Comparison between experimentally determined distribution (solid line) and simulated random distribution (dotted line). The occurrence of clusters of a certain number of molecules per cluster is altered (solid line), and the distribution differs from the expected averaged Poisson distribution (dotted line). Comparison of modelled ('Random') and measured distributions of the numbers of molecules per cluster for untreated cells with CD4 surface density (n) of 60 molecules/μm^2 (B), 200 molecules/μm^2 (C) and 300 molecules/μm^2 (D). Data from at least three separate experiments and a total of 15 different cells in each condition, respectively.

Overall, the analysis pipeline established in this chapter was deemed effective for quantitatively characterising CD4 and CCR5 distributions on untreated SupT1-R5 cells, and indicated that CD4 distribution randomly on untreated cells. Meanwhile, it is capable of detecting cross-scale organisational changes. The pipeline also indicated that CD4 and CCR5 has minimal colocalisation in untreated SupT1-R5 cells.

3.3 Discussion

In this chapter I established an imaging pipeline for visualising the nanoscale spatial organisation of CD4 on CD4$^+$ T cells under various conditions and times of antibody labelling, temperature, fixation, and agonist activation. This pipeline also allows me to mathematically describe the diameter of CD4 clusters individually and spatial relationship between CD4 and CCR5 clusters (percentage of colocalisation and comparing cluster features in colocalised and non-colocalised regions). Furthermore, I calibrated fluorophore blinking kinetics for molecular counting and colocalisation thresholds based on experimental data.

CD4 organised as small clusters (~60 nm in diameter) with 1-4 molecules per cluster (primarily 1 molecule) in untreated cells. Furthermore, CD4 and CCR5 were localised in distinct areas with less than 10% colocalisation in untreated SupT1-R5 cells, agreeing with what is seen under EM [266,267]. I also tested the

ability of my pipeline to detect changes in cluster parameters on a scale ranging from tens of to hundreds of nanometres in PMA treated SupT1-R5 cells. Lastly, I used statistical simulation to model a random CD4 distribution based on the number of CD4 molecules and compared it with the molecule number acquired experimentally. Together the analysis demonstrated that this pipeline has the capability to characterise membrane receptor distribution and quantitatively detect subtle changes in receptor distribution.

I further wanted to establish conditions in which labelling and imaging had a minimal apparent impact on the distribution of specific receptor molecules and the ability of these molecules to redistribute under particular conditions while avoiding sophisticated imaging setups, such as EM and 3D-STORM. Direct immobilise cells onto a glass surface can interfere with cell morphology. Flattening T cells on PLL-coated glass can cause artefacts when studying receptor organisation at nanoscale [268–270]. Therefore, in the study, samples were treated in suspension before depositing onto coverslips, allowing organisational changes and signal transduction to occur in near native condition and minimise potential artefacts induced by cell-glass interactions (Figure 3.2).

To establish the quantitative analysis pipeline, I started by comparing the ability of DBSCAN [113]and SR-tesseler [126] to analyse CD4 clusters on the untreated SupT1-R5 cells used throughout the study. DBSCAN performed well in identifying both heterogeneously sized clusters and calculating cluster diameter, which follows a similar trend as the manually annotated groups (Figure 3.3). This is consistent with a recent study evaluating the performance of cluster analysis algorithms [271]. The study showed that DBSCAN was robust in cluster identification in simulated data with multi-blinking nature [271]. However, I still found a statistically significant difference between manually annotated data and from DBSCAN. Manually annotated clusters were generally larger than in DBSCAN identified clusters (65 ± 23 nm vs 62 ± 24 nm). This is likely because the outline of DBSCAN identified clusters tend to be in the inside edge of optically identified clusters. In contrast, the very edge

of the cluster outlines was included when drawing cross-sections manually (Figure 3.3). Nevertheless, DBSCAN results best represent the manual annotation results. Additionally, the subtle difference was negligible when considering the relative change of cluster diameters in follow-up experiments.

For validating the sample preparation process, I quantitatively analysed different labelling conditions. I found there was no difference in pre- and post-fixation Q4120 labelling in both cluster diameters and the number of molecules per cluster, indicating that pre-fixation labelling can be used confidently without causing CD4 reorganisation (Figure 3.8, Figure 3.9). In addition, I tested the effect of double labelling. I saw that the mean diameter of identified clusters was higher per a larger portion of clusters with 5-8 molecules per cluster (Figure 3.10, Figure 3.11). Although the artificial clustering effect of the double labelling is subtle, introducing the double labelling (primary and secondary antibody labelling) in STORM may inevitably cause false-positive localisation identification and further quantitative variations. Therefore, the single labelling for CD4 was used throughout this study.

Following the approach used by Sieben et al. [227], I was able to calibrate the localisation data and obtain estimated numbers of CD4 molecules per cluster. It is critical to note that these numbers should be interpreted cautiously and deemed estimates, considering that the molecule numbers were mostly <10 per cluster. Several factors may contribute to potential undercounting the methods used. For example, though single labelling was used to minimise artificial amplification associated with use of second layer antibody, and I achieved a precision of ~15 nm (Figure 3.4), the binding efficiency of OKT4 is lower than the neutralising antibody Q4120. This was also reflected in a generally smaller number of clusters identified in OKT4 labelling groups (593 $\pm$ 92 clusters) compared to those in Q4120 labelling groups (821 $\pm$ 97 clusters). Post-processing calibration may also contribute to undercounting. This process requires a custom set dark time when calibrating experimental localisation coordinates tables. The parameter is a trade-off between over-merging (high confidence but underestimated counts) and under-merging (low

confidence but overestimated counts). In this study I chose the dark time as 10 (a long dark time) while the average measured was 7.6 to minimise false-positive molecular identifications (Figure 3.5). Nevertheless, the CD4 and CCR5 levels per cell measured in this study (total number of molecules/the area of a region of interest) are similar to those previously reported in primary CD4^{+} T cells and CD4^{+} stable T cell lines (CD4, 60 molecules/μm^2 vs 70 - 200 molecules/μm^2 [183,191,272]). Given the very different measuring techniques used, the numbers are reasonably close. Regardless of these uncertainties, the information extracted is still meaningful when investigating changes in molecule numbers associated with chemical stimulation and HIV treatment.

Using the established cluster characterisation pipeline, CD4 is organised as ~60 nm diameter clusters on the plasma membrane with 1-4 molecules per cluster (> 50% to be monomers). Although the oligomer states and its function correlation remain to be elucidated, these results are in line with previous studies in which it has been reported that the 55 kDa monomer of CD4 is most commonly expressed on CD4^{+} T lymphocytes with various quaternary forms, such as homodimers and tetramers, identified by biochemical assays [198,273].

To restrict membrane fluidity and trafficking, antibody and stimulation, incubation was carried out first at 4°C. However, 37°C is the temperature physiological most relevant for both chemical stimulation and HIV binding *in vivo*. Therefore, although 4°C incubation creates a window to trace receptor behaviour after stimulation at subsequent time points after returning to 37°C, CD4 distribution on the plasma membrane requires careful validation after the restoration of membrane fluidity and trafficking post returning to 37°C. In the assay, I quantified CD4 and CCR5 clusters post 1min and 15min at 37°C conditions and compared them with 0min samples (Figure 3.12). There is no difference shown in cluster diameters between 1,15min 37°C incubation and 0min at 37°C incubation for CD4 and CCR5 (Figure 3.13). Interestingly, subtle variations have been shown in molecule numbers calculated. The variations in molecule numbers were irregular rather than increasing with the 37°C incubation time. This indicates that it was unlikely to be clustering caused by

37°C incubation. Increased membrane fluidity associated with returning the cells to 37°C were likely to have contributed to these changes. Increased fluidity may cause movement of molecules on the edge of an identified larger cluster, resulting in changes in the parameters of the cluster identified by the algorithm as an outlier or in a cluster. These changes would not be sensitive enough to be picked up when characterised by diameter while appears as experimental variations in molecular counting. Therefore, this further emphasised that the molecule counting approach used is an estimation and is not robust enough for single molecule precision.

After chromatic aberration correction, the dual-colour labelling data showed that CD4 has a minimal association with CCR5 on CD4+ T cells (Figure 3.14, Figure 3.15). This indicates that CD4 and CCR5 are likely to be randomly localised on the PM on untreated CD4+ T cells. Previous biochemistry studies have suggested that some CD4 and CCR5 are constitutively associated in the PM even when exogenously co-expressed on 3T3 cells (mouse embryonic fibroblasts) [274–276]. FRAP studies have shown that CD4 may modify the mobility of CCR5, confining a portion of the co-receptor population to small membrane domains enriched with both molecules [276]. Nevertheless, my result is not unexpected. Distinguishing CD4 and CCR5 localisation in small compartments would be problematic with CFM. As shown in EM, little evidence of CD4 and CCR5 association was demonstrated in CD4 and CCR5 expressing CHO cells [277]. In addition, biochemical experiments may be compromised by the formation of mixed micelles. In CD4+ T cells, the cell line most relevant to HIV binding and fusion, my results indicate a minimal association between CD4 and CCR5.

To test the sensitivity of my analysis pipeline to organisational changes, I have treated cells with CD4 endocytosis inducing chemical PMA. I saw a drastic change in PMA treated CD4 membrane organisation in cluster diameter and number of molecules per cluster (Figure 3.16, Figure 3.17). A decrease in the number of CD4 clusters identified corresponds well with the cell-surface internalisation of receptors post-PMA treatment. These results confirmed that

the quantitative analysis pipeline could detect organisational changes at different scales, from tens of nanometres to hundreds of nanometres, a robust pipeline for investigating HIV induced receptor organisational changes.

To build a model for studying whether changes detected would occur by chance, I applied Poisson statistical modelling to simulate a random distribution of receptors on the cell surface and compared my results with the experimental data (Figure 3.18). Although correlation-based analysis, such as Ripley's function [102], nearest neighbour analysis [101], and pair correlation function [107] can also determine whether a point is in a cluster by comparing with a stimulated random distribution. These methods are more robust in providing information with regards to clusters radius, nearest neighbour distance rather than number of molecules per cluster. The customised script used in the study allowed me to compare the randomness with reference to the number of molecules per cluster. It may be helpful for interpreting the data and the biological significance of subtle receptor organisational changes. For example, if a distinct number of molecules per cluster changes in HIV treated data, it gives me hint that this specific number might be relevant to HIV entry kinetics, as the stimulation proved that the increase/decrease of these numbers could not happen by chance.

In this chapter, I have implemented a membrane receptor nanoscale visualisation and quantitative characterisation pipeline, including cluster characterisation and molecule counting. This pipeline can also report the spatial relationship between proteins in dual-colour labelling samples. Additionally, it is a robust pipeline in detecting organisational changes on a scale from tens to hundreds of nanometres. I identified that CD4 is organised as small clusters (Table 3.3), with most clusters containing 1-4 molecules per cluster. I also statistically stimulated CD4 random distribution, which is similar to the experimental data. Thus, the labelling, imaging and quantifying pipeline I established is a robust approach for characterising HIV-1 induced receptor

Figure	Protein	Experiment condition	Mean (nm)	SD / <u>SEM</u>	Data size (number of cells)
Figure 3.3 B	CD4	Manual annotation	65	<u>0.27</u>	10
	CD4	SR-Tesseler	26	<u>0.28</u>	15
	CD4	Clus-DoC	55	<u>0.25</u>	15
Figure 3.8 A	CD4	Pre-fixation labelling	63	30	15
	CD4	Post-fixation labelling	63	28	15
Figure 3.10 A	CD4	Primary labelling	59	21	15
	CD4	Secondary labelling	61	24	15

Figure 3.12 A	CD4	0min	62	<u>0.20</u>	15
	CD4	1min	62	<u>0.16</u>	15
	CD4	15min	62	<u>0.18</u>	15
Figure 3.14 A	CD4	Alexa 647	66	19	15
	CD4	Alexa 568	67	30	15
	CCR5	Alexa 647	109	23	15
	CCR5	Alexa 568	109	43	15
Figure 3.14 C	CD4-Alexa 647	Colocalised	64	17	10
	CD4-Alexa 647	Non-colocalised	62	11	10
	CD4-Alexa 568	Colocalised	63	5	10

	CD4-Alexa 568	Non-colocalised	70	20	10
Figure 3.14 D	CCR5-Alexa 647	Colocalised	102	19	10
	CCR5-Alexa 647	Non-colocalised	99	11	10
	CCR5-Alexa 568	Colocalised	118	21	10
	CCR5-Alexa 568	Non-colocalised	104	15	10
Figure 3.16 A	CD4	0min 4α-PMA	65	0.30	10
	CD4	15min 4α-PMA	64	0.31	10
	CD4	0min PMA	65	0.29	10
	CD4	15min PMA	112	2.34	10

Table 3.3 Mean ± SD of cluster diameters identified in Chapter 4.

Chapter 4 Nanoscale CD4 reorganisation induced by HIV-1

4.1 Introduction

HIV-1 and host cell membrane fusion marks one of the first phases of the HIV-1 replication cycle. As discussed in Chapter 1.3.4, HIV-1 membrane fusion begins when HIV Env gp120 makes contact with the principal receptor CD4 and co-receptors CCR5 or CXCR4 [278–280], which are primarily expressed on CD4^{+} T cells [183]. The interaction between Env and receptor and coreceptor triggers the exposure of the Env fusion peptide at the N terminus of gp41, which subsequently inserts into the host cell membrane [281]. The ectodomain of gp41 then folds back on its own to form a highly stable 6-helix bundle, which brings the fusion peptide-associated cellular membrane and the viral membrane into close proximity [282]. This reorientation drives the fusion of the viral and host cell membranes (Figure 1.6, Chapter 1.3.4). Biochemical and morphological studies have provided a basic understanding of the HIV fusion process. However, many pieces of the process remain to be understood in detail, especially the behaviour of the receptor components that mediate virus binding and trigger fusion.

4.1.1 Env numbers and HIV-1 entry

Several findings have suggested a close correlation between the number of Env molecules on a virus particle and HIV infectivity. Studies from quantitative western blotting [165] and cryo-EM [283] revealed that each HIV-1 virion has an average of 14 Env trimers per virion. Follow up mathematical modelling showed that HIV-1 derived from HEK-293T cells has an average of 6-20 Env trimers per virion [284]. This latter study suggested that, for HIV-1 with low infectivity and slow fusion kinetics, higher Env number is required for a productive entry; highlighting the stoichiometry of HIV entry is an important

parameter steering virion infectivity [284]. On average, 1-7 wild-type Env trimers are thought to be required to complete a fusion event [284]. Experimental evidence using optical trapping virometry showed that, with DEAE-dextran, an agent known to enhance HIV-1 infectivity, HIV-1 infectivity and gp120 density displayed a sigmoidal correlation with an evident plateau. By contrast, without DEAE-dextran, HIV-1 infectivity increases monotonically with increased gp120 density and without saturation [285]. Although the precise number and mechanisms remain to be studied, mathematic modelling results suggest that, at the single-particle level, HIV-1 infectivity increases with the number of Env trimers once a lower threshold is reached (presumably 2-3 Env trimers). An upper threshold of the number of Env molecules also exists while HIV reaches a maximum infectivity (hypothetically 7-9 Env trimers) [286–289].

4.1.2 Env organisation and HIV-1 fusion

Although the topology of Env in the viral membrane is well understood, the spatial organisation of Env trimers is less clear. A study using super-resolution STED microscopy revealed that exterior Env reorganisation is essential in virion maturation [290]. Envs were randomly distributed on immature virions, but clustering on mature virions. This clustering behaviour might generate a local concentration of Env that can support fusion. A follow-up mechanic study using FCS-STED has shown an increase in mobility during HIV maturation, which might be one of the drives for Env clustering [291]. All the studies above have indicated that the quantitative and organisational characterisation of HIV components is indispensable when studying HIV-1 fusion.

4.1.3 Questions remaining to be answered from the host cell membrane point of view

There are far fewer quantitative and organisational studies of CD4 and CCR5 in the context of host cells during HIV-1 fusion. A recent study combining fluorescence fluctuation spectroscopy imaging and number & brightness (N&B) analysis on COS-7 cells showed that, for R5-tropic virus-like particles (VLPs),

an Env-CD4 interaction generates an asymmetric Env pre-hairpin intermediate that can bind two additional CD4 molecules with concomitant CCR5 dimerisation. This secondary intermediate leads to the formation of a final fusion-competent complex with a total of 4 ± 0.3 CD4, 2 ± 0.3 CCR5 per Env trimer [211]. However, this study did not take Env cluster on the mature HIV-1 virion into consideration and did not show that the proposed complex does lead to a successful fusion event (Figure 4.1).
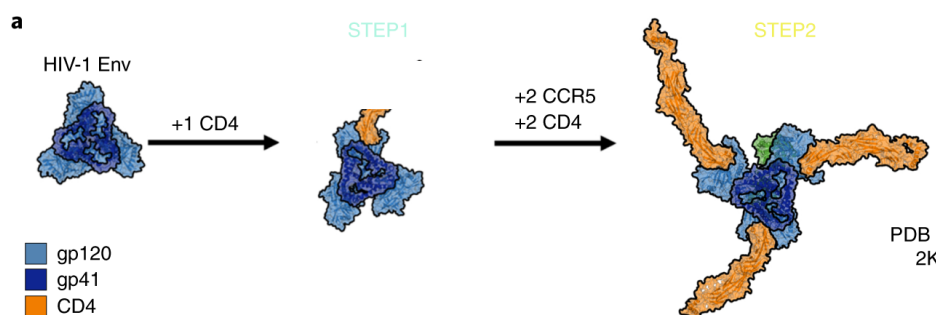
Figure 4.1 A proposed model for HIV-1 Env-CD4 stoichiometry. Adapted from [211]

From an organisational point of view, imaging is considered to be one of the most straightforward ways to study protein organisation. However, CFM cannot achieve the resolution needed to look at HIV and membrane protein clusters (30-250nm). Although CD4 and CCR5 polarisation were used to describe receptor reorganisation [292–294], it was primarily used as a complementary approach to biochemical assays. Using CD4 and CCR5 polarisation as a surrogate for HIV induced clustering can be questioned because no precise spatial relationship between proteins and virus is shown. Furthermore, due to the limitations of imaging approaches, most studies have focused on downstream proteins that interact with HIV receptors rather than receptors themselves, e.g. cytoskeleton-associated proteins [292–302]. Therefore, the labelling, imaging, and quantitative analysis pipeline I have established may be a useful tool to quantitatively study one of the first step of HIV-1 entry, to determine how CD4 molecules reorganises during HIV binding by direct protein and HIV-1 visualisation and quantitative characterisation.

4.1.4 Temperature arrested state (TAS): a useful intermediate state to study HIV-1 entry

Most HIV-fusion events occur as fast as under a minute to up to 15 minutes after virus addition to cells at 37ºC [262–265]. To capture the whole process using the established pipeline, from virus contact to fusion, I need to break the process down into discrete steps. Temperature can be used to experimentally manipulate the progression of the HIV fusion event. Cell-HIV association enters arrested state (TAS) when the temperature is reduced below 24ºC. However, a moderate level of gp120-CD4 specific association continues at low temperature with associated gp120 conformational changes [303,304]. Furthermore, in TAS, gp120 is kinetically poised to interact with, but not yet engaged with, the co-receptor [304]. Notably, the fusion process will continue when the TAS is released and the temperature shifted back to 37ºC [300,304,305]. At 4ºC, HIV can bind to cells with moderate levels of CD4-specific association [303], reduced membrane fluidity and cytoskeleton dynamics. Thus, in the experiments described in this chapter, the analytical pipeline described in Chapter 3 and 4 is suitable for analysing receptor organisation and reorganisation during HIV engagement.

4.1.5 Objectives

In the experiments described in this chapter, I use my established labelling, imaging, and quantitative analysis pipeline to characterise CD4 spatial redistribution post-HIV binding and investigate whether CD4 organisational changes are CCR5 dependent. Specifically, I

- Optimise the multiplicity of infection for STORM imaging.
- Characterise features of CD4 cluster following HIV-1 binding and analyse the spatial relationship with HIV particles at different time points following release of a temperature block on SupT1 cells.
- Measure how features of CD4 clusters change following release of a temperature block on SupT1 cells.

- Compare the experimentally acquired distribution of molecule numbers per cluster with previously simulated distributions to test the randomness of any observed organisational changes.

4.2 Results

4.2.1 Establishment of an optimal MOI

To find a balance between having a sufficient number of bound HIV particles per FOV and a relevant number of HIV virions per cell, MOIs (calculation method described in Chapter 2.3.2) of 10, 30 and 50 infectious units per cell were added. SupT1-R5 cells were pre-incubated with OKT4-AlexaFluor 647 for 15min at RT and then cooled to 4°C before adding different numbers of HIV-1$_{JR-CFS}$. The antibody-HIV-cell mixture was incubated at 4°C for 1hour. HIVs virions were labelled using an anti-Gag p24 antibody (following permeabilsation) before imaging. The average amount of HIV observed was 2, 26, and 46 particles per cell, respectively (Figure 4.2). To maximise the experimental throughput while maintaining a reasonable number of bound particles, I chose MOI 30 for the following experiments.
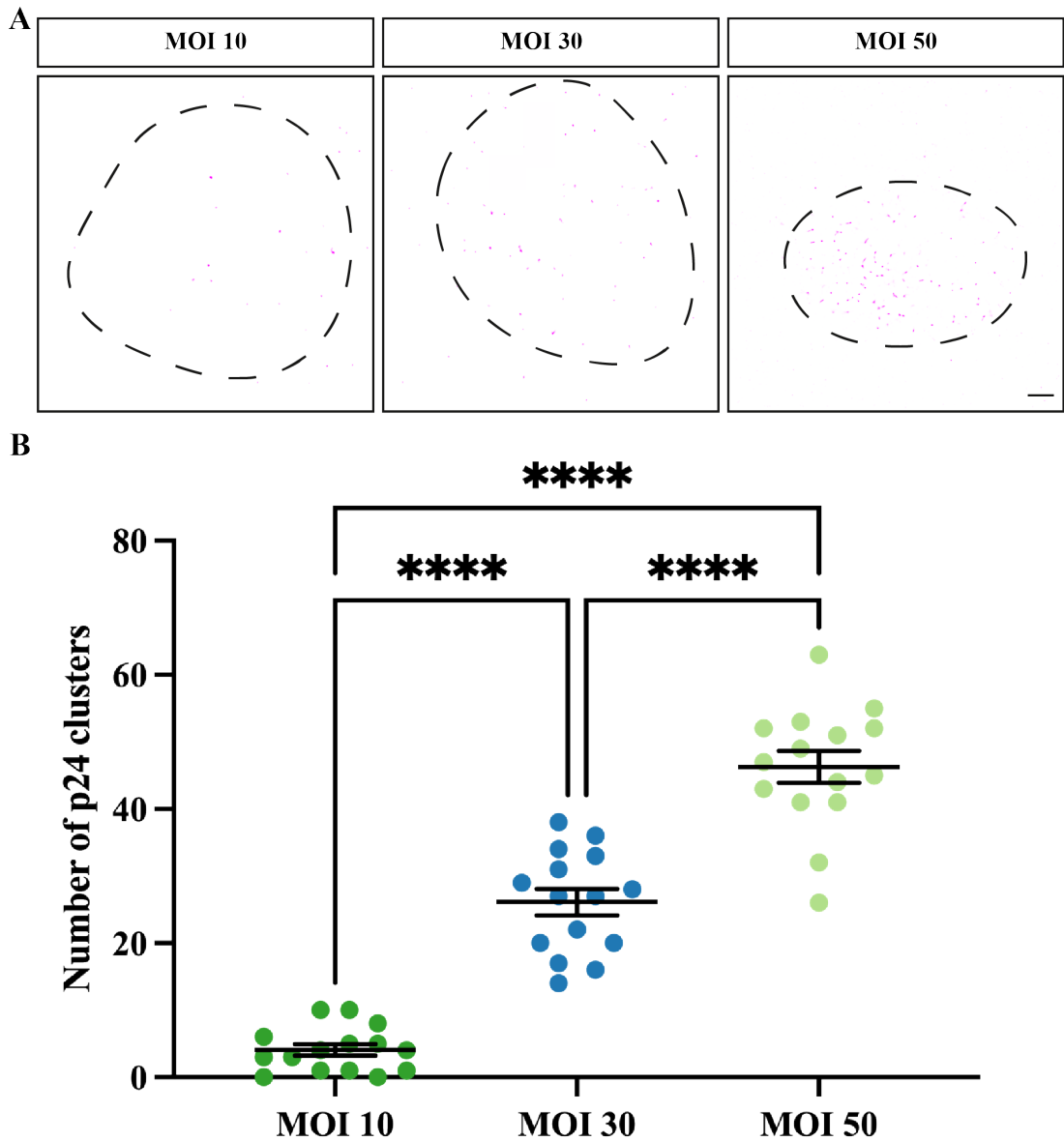
Figure 4.2 Determining the optimal MOI for imaging experiments.

A. Representative images of p24-labelled HIV particles (magenta) at input MOIs of 10, 35, 50 on SupT1-R5 cells. The dashed line represents the outline of a cell. Scale bar = 2 μm. B. Quantification of the number of HIV particles per cell at MOI 10, 30. 50. **** p<0.0001. 15 cell profiles were measured per condition. Bars indicate mean ± SEM. The data are representative of at least three independent experiments.

4.2.2 Analysis of HIV induced CD4 organisation at TAS

Even though HIV cell entry is initiated by the binding between the HIV Env subunit gp120 and CD4 molecules, how Env-receptor binding impacts the nanoscale organisation of CD4 in the plasma membrane of target cells remains poorly understood [306]. Thus, using the labelling, imaging and quantitative analysis pipeline I established in the previous chapters, I set out to measure the effect of HIV binding on CD4 nanoscale organisation.

To validate that CD4 nanoscale organisation is not changed by TAS, I compared CD4 organisation in Env-CD4 binding permissive and non-permissive conditions without 37°C incubation. For Env-CD4 binding permissive condition, as described previously, I incubated SupT1-R5 cells with OKT4-AlexaFluor 647 for 15min at RT and cooled to 4°C before adding HIV$_{JR-CSF}$ at MOI 30. A CD4 binding non-permissive condition was used as control; SupT1-R5 cells were co-incubated with OKT4-AlexaFluor 647 and the neutralising anti-CD4 antibody Q4120, which inhibits Env-CD4 binding [307] at RT before cooling down to 4°C and adding HIV$_{JR-CSF}$. Although there were HIV particles on the imaged PM in both conditions, dual-colour TIRF-STORM imaging of immunolabelled CD4 and HIV p24 showed no difference in CD4 organisation in regions with virus (Figure 4.3 A, B).

Quantitatively, no significant difference was shown between CD4 clusters with HIV colocalisation (63 ± 8 nm) and CD4 clusters without HIV colocalisation (64 ± 16 nm) in Env-CD4 binding permissive condition (Figure 4.3 C). In Env-CD4 non-permissive group, the diameter of HIV-colocalised CD4 clusters (63 ± 7 nm) was similar to that of HIV-non-colocalised CD4 clusters (58 ± 7 nm; Figure 4.3 D). Thus, no nanoscale organisational change was seen under TAS conditions in both Env-CD4 binding permissive and non-permissive conditions. This set a foundation for me to investigate further the effect of virus binding on CD4 nanoscale organisation after initiating the fusion process by 37°C incubation.
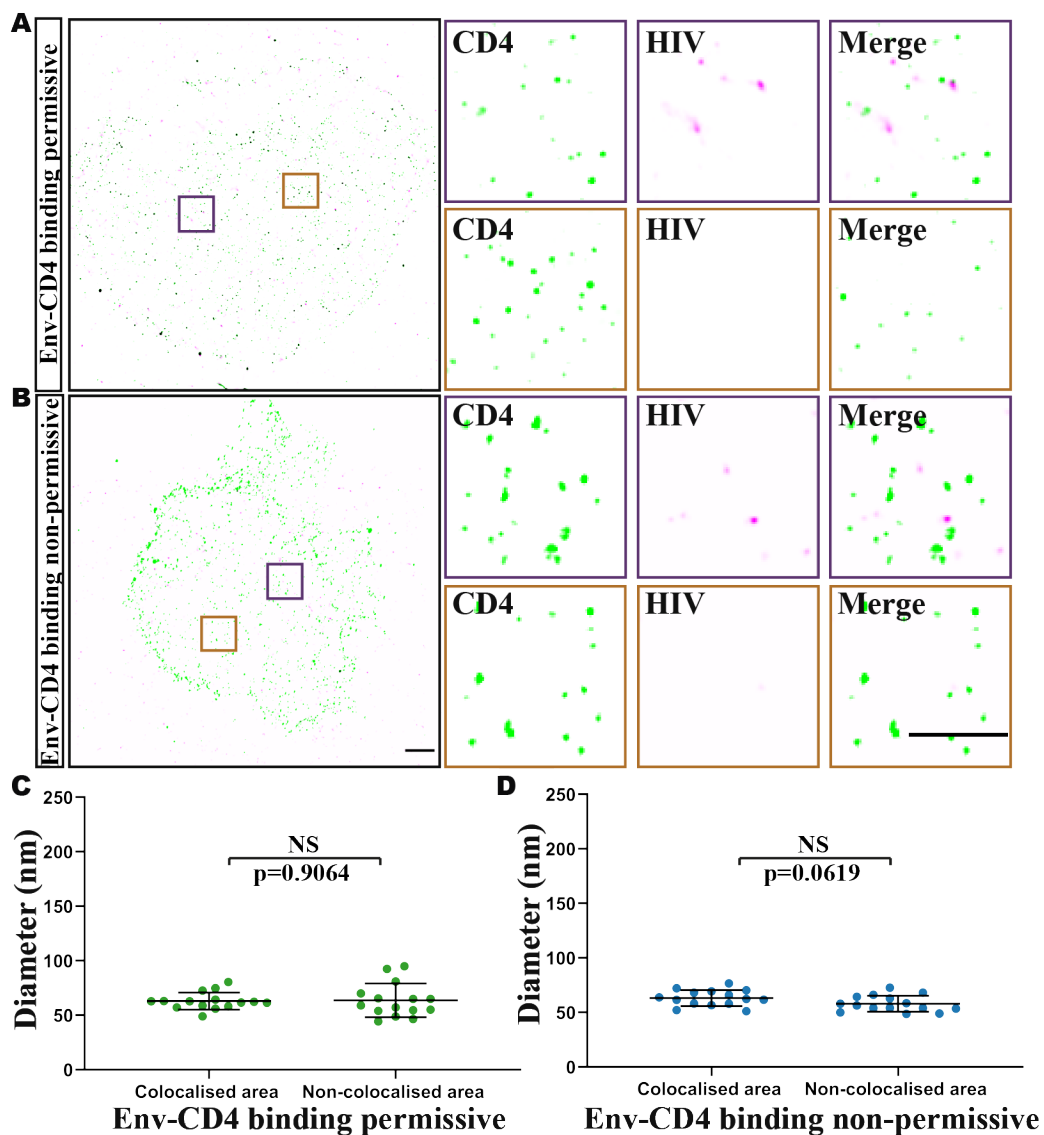
Figure 4.3 Analysis of HIV-bound CD4 clusters under TAS conditions.

A, B Representative TIRF-STORM images and selected magnified regions of cell-surface CD4 (green) and HIV p24 (magenta). Scale bar=2μm. C, D Quantification of CD4 cluster diameters in Env-CD4 binding permissive (C) and non-permissive (D) conditions in both HIV-CD4 colocalised regions and non-colocalised regions. Each point represents the average CD4 cluster diameter on one cell. 15 cell profiles were measured per condition. Bars indicate mean ± SD. The data are representative of at least three independent experiments. NS p>0.05.

4.2.3 Analysis of HIV induced CD4 reorganisation after 1min at 37°C

To study the impact of HIV-1 binding on CD4 nanoscale organisation, samples were prepared as in the previous section under both Env-CD4 permissive and non-permissive conditions (Figure 4.4 C). Dual-colour TIRF-STORM imaging of immunolabelled CD4 and HIV p24 revealed enlarged CD4 clusters around HIV contact sites in the permissive condition but not in the non-permissive control condition (Figure 4.4 A, B). Cell-surface bound HIV associated CD4 clusters were more than twice the diameter of non-HIV-colocalised clusters on the same cells (191 ± 6 nm vs 65 ± 9 nm, respectively; Figure 4.4 D). Moreover, the diameter of the non-HIV-associated CD4 clusters was in good agreement with those measured on untreated cells (65 ± 9 nm vs 62 ± 11 nm, respectively; Figure 4.4 D vs Figure 3.15 C). This increase in CD4 cluster diameter was not observed when Env-CD4 binding was blocked by neutralising anti-CD4 antibody Q4120 in both HIV associated and non-associated regions (66 ± 6 nm vs 66 ± 4 nm; Figure 4.4 E). These results indicate that HIV association induced an increase in the size of CD4 clusters.
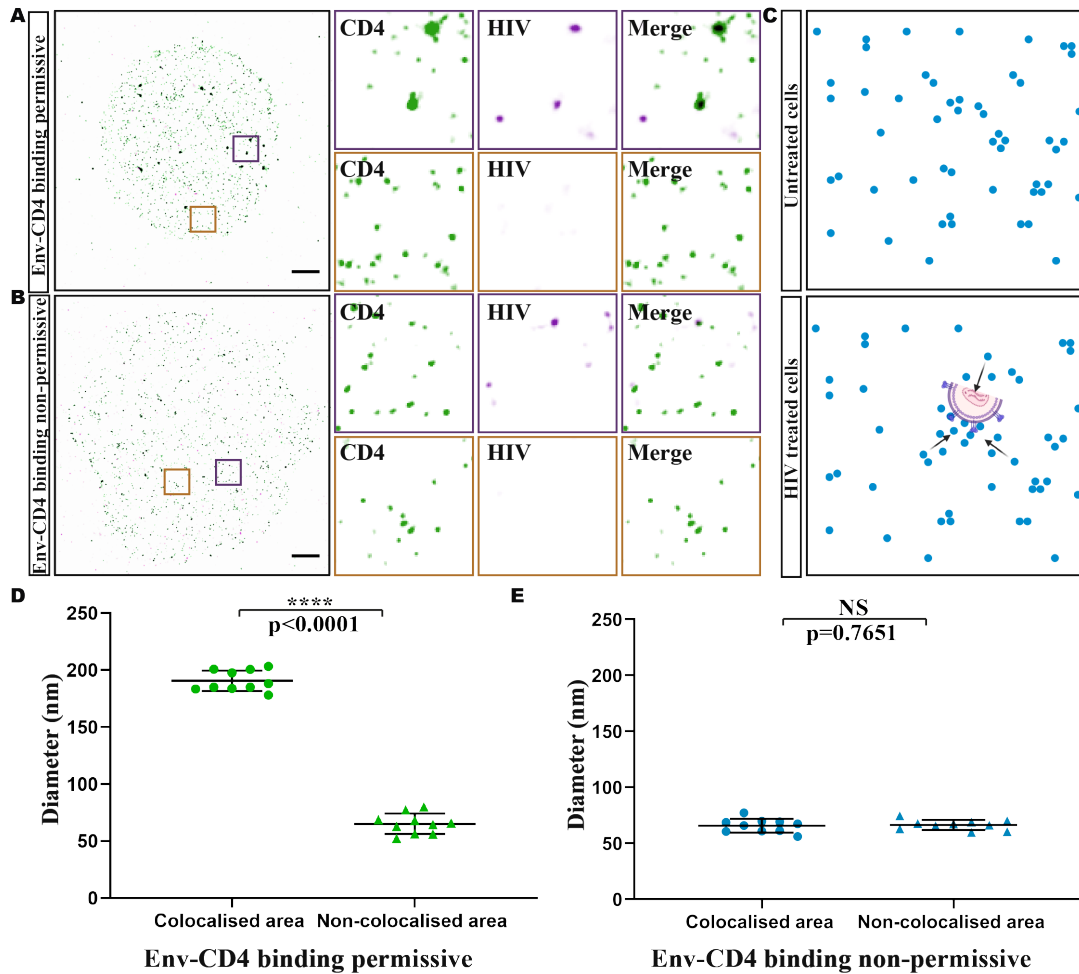
Figure 4.4 Analysis of HIV induced CD4 cluster organisation after 1 min at 37°C.

A, B Representative TIRF-STORM images and insets of cell-surface CD4 (green) and HIV p24 (magenta). Scale bar = 2μm. C Schematic of cell-surface CD4 molecules (blue) in untreated cells (upper panel) and HIV treated cells (lower panel). D, E Quantification of CD4 cluster diameters in Env-CD4 binding permissive (D) and non-permissive (E) conditions. Each point represents the average CD4 cluster diameter on one cell. 10 cell profiles were measured per condition. Bars indicate mean ± SD. The data are representative of at least three independent experiments. NS $p > 0.05$. **** $p < 0.0001$.

4.2.4 Quantitative analysis of the HIV-CD4 spatial relationship

Although Env-CD4 binding was inhibited by Q4120, cell-bound HIVs were still detected. To study the spatial relationship between HIV and CD4 in both 1min 37°C incubation groups, the percentage colocalisation between HIV and CD4 was analysed by Clus-DoC. In the Env-CD4 binding non-permissive condition, only 5% ± 2% of virus particles were colocalised with CD4 clusters, whereas 83% ± 5% of virus particles were colocalised with CD4 clusters in the binding permissive condition (Figure 4.5 B). This indicated that the association between Env and CD4 was specific. In the binding permissive condition, the colocalised regions showed enlarged CD4 clusters (Figure 4.5 A); over 80% of the virus particles were associated with enlarged CD4 clusters. A small amount of non-specific HIV binding was detected in the Env-CD4 non-permissive binding condition, presumably due to virions binding to cell surface adhesion proteins.
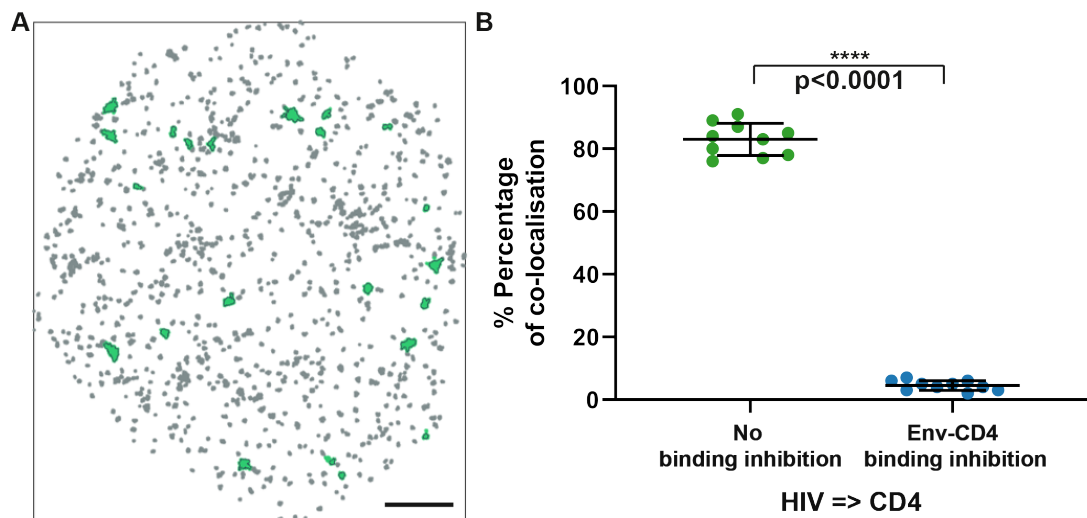
Figure 4.5 Analysis HIV-CD4 spatial relationship.

A A representative image showing enlarged CD4 clusters that colocalised with HIV p24 signal on the same cell illustrated in Figure 4.4 A. B The percentage of HIV particles colocalised with CD4 in the binding permissive condition and Env-CD4 binding non-permissive condition as obtained from Clus-DoC co-clustering analysis. Green indicates identified clusters; grey indicates other

clusters. Each data point represents a cell. Bars indicate mean ± SD. The data are from 10 different cell profiles in three separate experiments. **** p< 0.0001.

4.2.5 Molecular counting of CD4 clusters after 1min at 37°C

To look into the enlarged CD4 clusters in detail, I conducted molecule counting on CD4 clusters. Only looking at the colocalised area, in the binding permissive condition, the increase in CD4 cluster size was accompanied by an increase in the number of CD4 molecules per cluster; 70% of clusters consisted of 13-16 molecules, compared to 1-4 molecules per HIV-associated cluster when receptor binding was inhibited (Figure 4.6 A). Characterising all clusters identified on cell surfaces, there was a significant increase in clusters containing 13-16 CD4 molecules in the Env-CD4 binding permissive condition, compared to Env-CD4 non-permissive condition (Figure 4.6 B). Significantly, this reorganisation did not lead to a statistically significant general increase in the density of CD4 clusters per ROI (Figure 4.7). This indicated that the increase in cluster diameters is likely due to local accumulations of CD4 molecules. The data indicate that HIV-receptor binding at the plasma membrane induced an increase in local CD4 clustering around bound viral particles in a manner dependent on direct interaction between the virus and receptors.
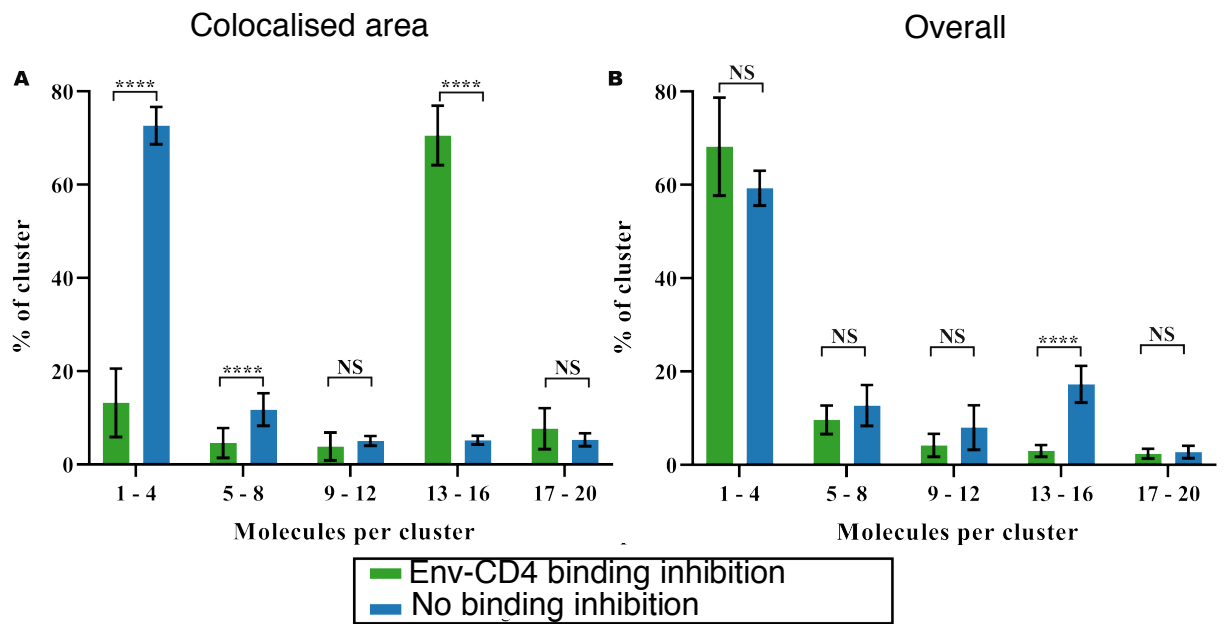
Figure 4.6 Molecular counting of CD4 molecules after 1min at 37ºC.

Molecular counting of colocalised areas (A) and all identified clusters (B) in Env-CD4 binding inhibition and no binding inhibition conditions. Bars indicate mean ± SD. The data are from 10 different cell profiles in three separate experiments. **** p< 0.0001.

A

Density (molecules/µm²) plot comparing untreated cells and HIV treated cells, with NS p=0.7152.
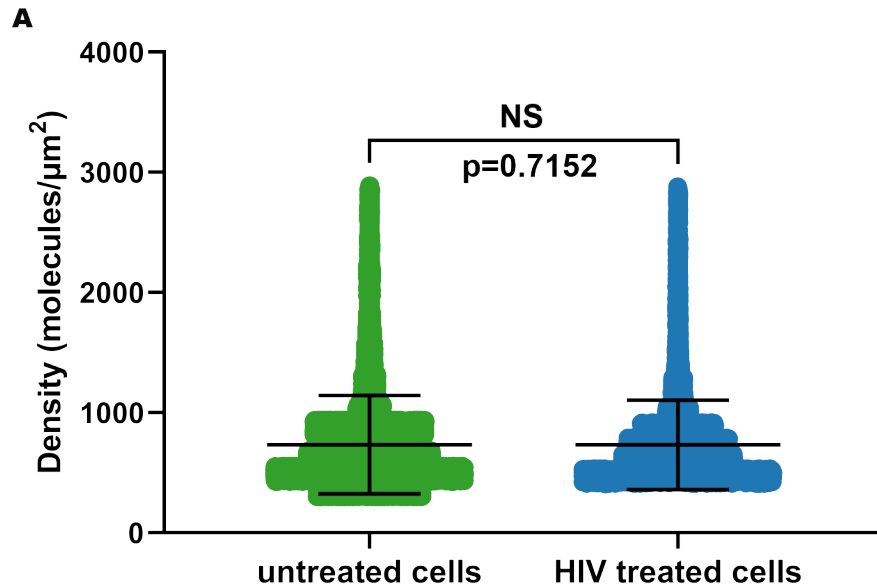
Figure 4.7 CD4 densities on HIV-treated and untreated cells.

A. Distribution of CD4 molecule density of CD4 molecules on untreated cells and HIV-treated cells. Data from 15 cell profiles in each condition were plotted. Each point represents 1 cluster; Bars represent mean ± SD. NS p>0.05

4.2.6 Comparison between the experimental data and the statistical model

In Chapter 3.2.9, I used a theoretical Poisson statistical model to simulate a random CD4 distribution in the untreated condition. To test the randomness of the increased number of CD4 molecules per cluster detected in HIV treated cells, I compared the number of CD4 molecules in HIV treated cells with a simulated random distribution. A similar apparent additional peak at 13-16 molecules per cluster was not predicted by the theoretical model (Figure 4.8). This further supported that the observed CD4 cluster reorganisation is a result of HIV binding.
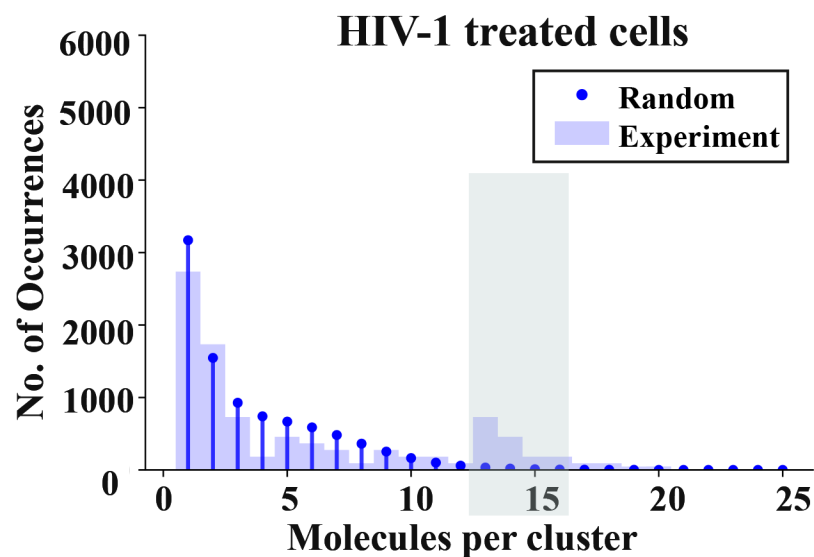
Figure 4.8 Comparing the experimental data in HIV treated cells with the statistical modelling of a random CD4 surface distribution.

The discrepancy between the predicted model and the experimental data in HIV treated cells is highlighted in grey shading. Data from at least three separate experiments and total 15 different cell profiles in each condition.

4.2.7 Analysis of HIV induced CD4 cluster reorganisation after 2, 5 and 10min at 37°C

After adding HIV-1 at 37°C, majority of fusion events occur between 1min and 15min [262–265]. Aiming to capture CD4 organisation beyond an initial 1 min time point, I extended the 37°C incubation time to 2, 5, and 10min and analysed the organisation of CD4 as described above. Increased CD4 clustering was still seen in HIV bounded areas after 2 and 5min but not after 10min at 37°C (Figure 4.9 A). Comparing the diameters of CD4 clusters in HIV bounded and unbounded areas, there was no difference in samples kept at 4°C incubation (62 ± 1.74 nm vs 65 ± 2.78 nm) and an apparent increase after 1min at 37°C (191 ± 2.26 nm vs 60 ± 2.07 nm), as shown previously. After 2min at 37°C, the CD4 cluster diameter in HIV associated areas was larger than in areas without virus (162 ± 8.56 nm vs 54 ± 2.15 nm), but slightly less than at 1min. This trend continued for longer incubation times; there was a further decrease in CD4

cluster diameters after 5min at 37°C, though the CD4 cluster diameters remained larger than in virus negative areas (105 ± 10.72 nm vs 54 ± 1.53 nm). After 10min at 37°C, there was no significant difference in the sizes of CD4 clusters for areas with and without virus (71 ± 7.02 nm vs 66 ± 4.46 nm). This observed change in the nanoscale organisation of CD4 is likely to be functionally correlated with either the process of coreceptor binding or HIV fusion.

A

2 min warm incubation

| CD4 | HIV | Merge |
| CD4 | HIV | Merge |

5 min inbubation

| CD4 | HIV | Merge |
| CD4 | HIV | Merge |

10 min warm incubation

| CD4 | HIV | Merge |
| CD4 | HIV | Merge |

B

ns

ns   ****   ****   ****   ns

Mean Diameter (nm)

250
200
150
100
50
0

| CA | NCA | CA | NCA | CA | NCA | CA | NCA | CA | NCA |
| 0 min | | 1 min | | 2 min | | 5 min | | 10 min | |
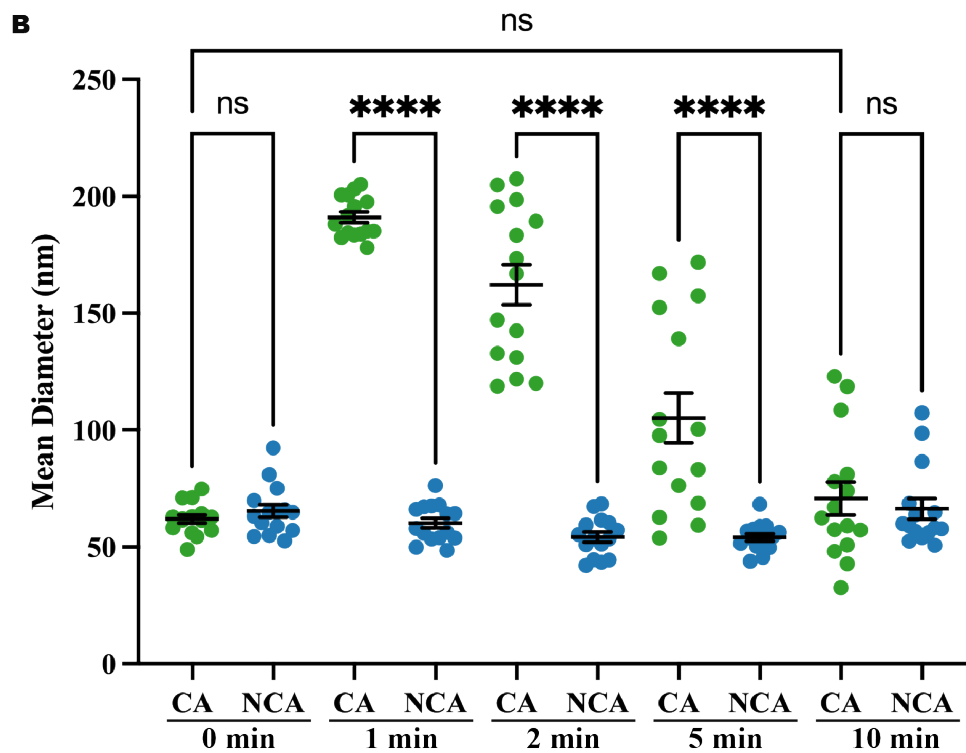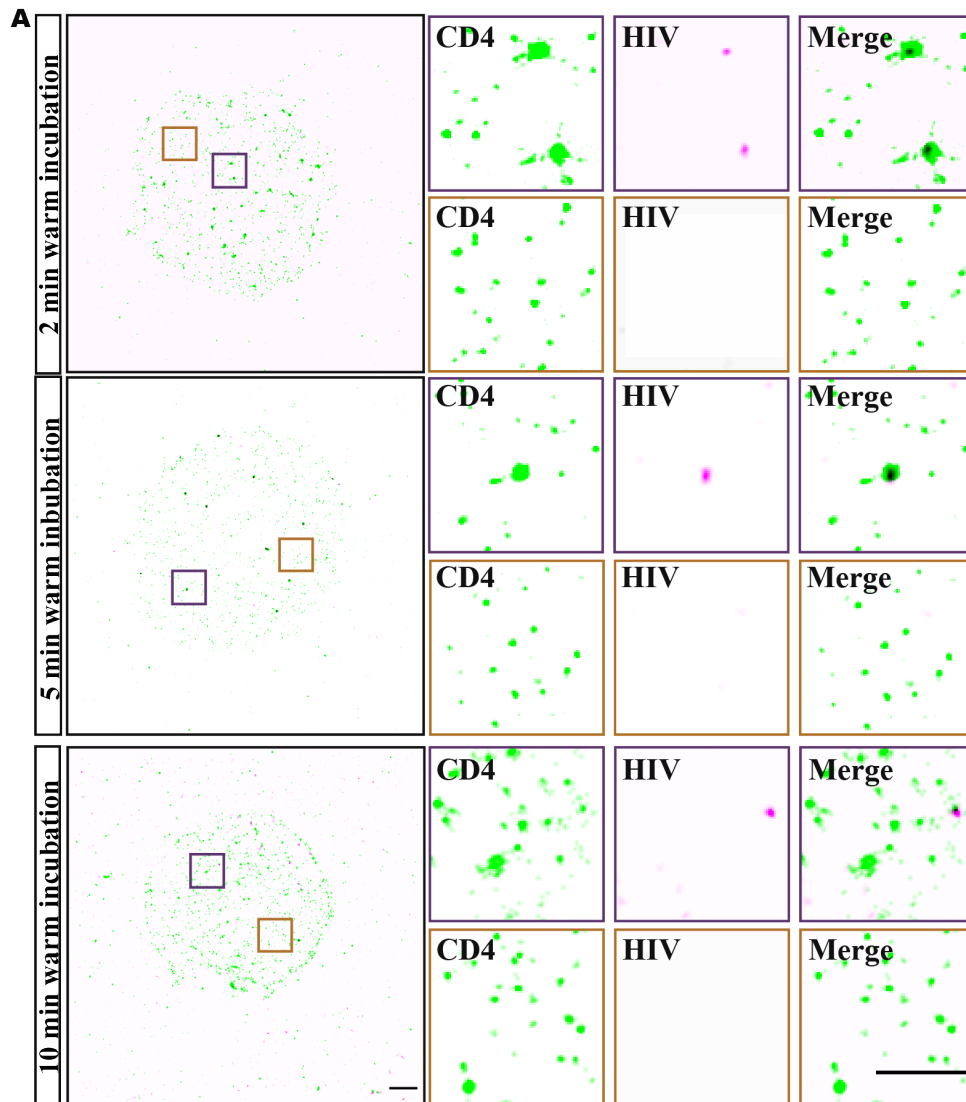
Figure 4.9 CD4 nanoscale organisation after HIV treatment and 2, 5, and 10 min at 37°C.

A. Representative TIRF-STORM images and insets of cell-surface CD4 (green) and HIV p24 (magenta) after 2, 5, and 10min at 37°C. Scale bar = 2 µm. B. Quantification of CD4 cluster diameters after 2, 5, 10min at 37°C. CA indicates virus colocalised areas. NCA indicates non-colocalised areas. Each point represents the average CD4 cluster diameter on one cell. 15 cell profiles were measured per condition. Bars indicate mean ± SEM. The data are representative of at least three independent experiments. ns p>0.05. * p<0.05. ** p<0.01. **** p<0.0001.

4.2.8 Characterisation of the spatial relationship between HIV and CD4 after 2, 5 and 10min at 37°C

To test whether the changes I observed in CD4 organisation is correlated with the interaction between HIV and CD4, I quantified the colocalisation of HIV and CD4 as previously described. There was 18% ± 2.33% colocalisation between HIV and CD4 in samples maintained at 4°C and 80% ± 1.94% colocalisation in samples after 1min at 37°C. The ratios decreased to 69% ± 2.91% in samples with 2min incubation and 59% ± 3.00% in samples with 5min incubation at 37°C. The association between HIV and CD4 dropped to the base level (21% ± 1.94%) after 10min at 37°C (Figure 4.10). Thus, it is likely that HIV and CD4 association decreases 10min after the temperature shift.
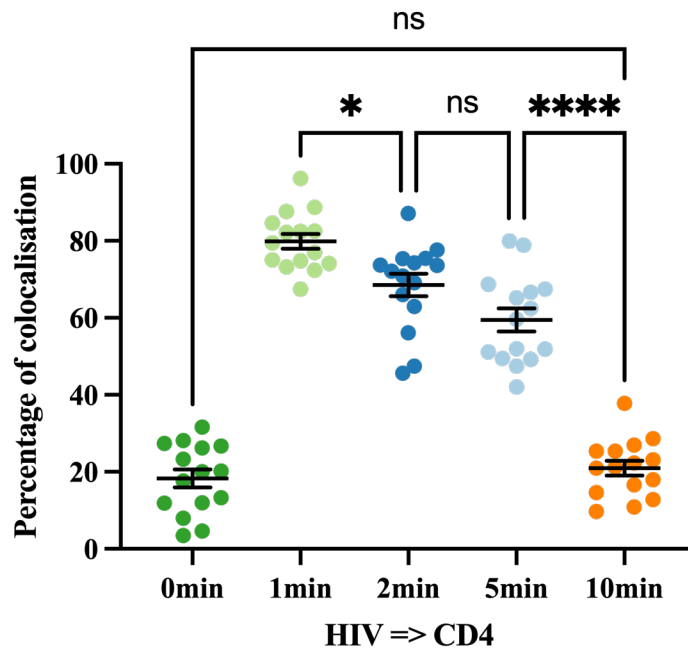
Figure 4.10 The percentage of HIV particles colocalised to CD4 in 0, 1, 2, 5 and 10min at 37ºC.

Each data point represents a cell. Bars indicate mean ± SEM. The data are from 15 different cell profiles in three separate experiments. ns p>0.05. * p<0.05. ** p<0.01. **** p< 0.0001.

4.2.9 Number of HIV clusters after 2, 5 and 10min at 37ºC

The number of HIV cluster on the PM after 2, 5 and 10min at 37ºC was quantified. There were 32 ± 2.16 HIV clusters in samples maintained at 4°C. The number remained similar in cells after 1 and 2min post 37ºC incubation (32 ± 1.97 and 30 ± 2.07). HIV cluster numbers decreased in cells following 5min and 10min 37ºC incubation to 22 ± 1.54 and 13 ± 1.31, respectively (Figure 4.11). These results indicate that, a. HIV might undergo the entry process, b. move further away for co-receptor engagement, while the disassociation between CD4 and HIV observed in Chapter 4.2.8.
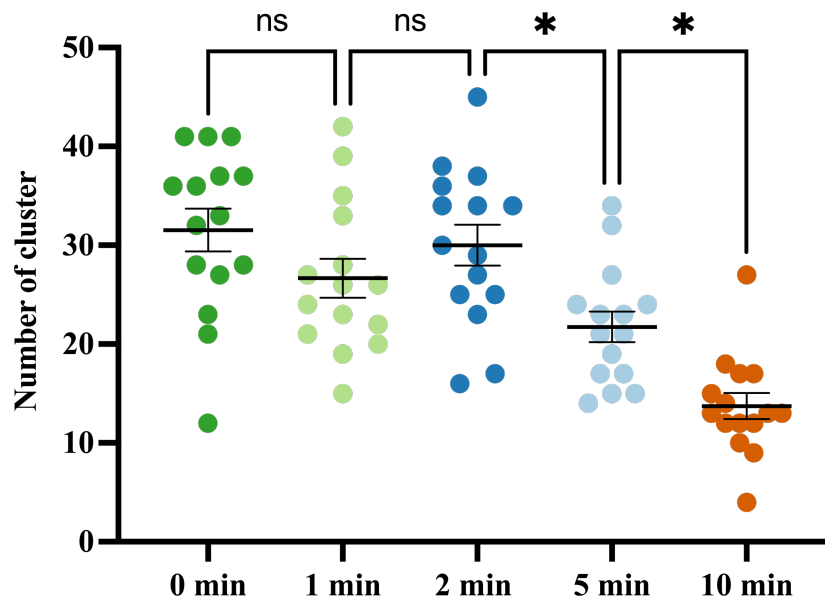
Figure 4.11 Counting of HIV cluster numbers after 0, 1, 2, 5 and 10min at 37°C.

Each data point represents a cell. Bars indicate mean ± SEM. The data are from 15 different cell profiles in three separate experiments. ns p>0.05. * p<0.05.

4.2.10 Counting of CD4 molecules in clusters after 2, 5 and 10min at 37°C

To study whether the increase in the size of the CD4 cluster corresponded to an increase in the number of CD4 molecules per cluster, I performed molecular counting on samples after 2, 5 and 10 min at 37 ° C, as previously described. In colocalised areas alone, an increase in the percentage of clusters containing 13-16 molecules was apparent after 1, 2, and 5min at 37°C, while clusters with 1-4 molecules was the primary clusters after 10min 37°C incubation (Figure 4.12 A, B). After counting all identified clusters, samples without 37°C incubation and after 10min at 37°C had a similar frequency of molecule numbers per cluster, with most clusters containing 1-4 CD4 molecules. As with clusters seen after 1min at 37°C, the frequency of clusters with 13-16 CD4 molecules was high after 2min at 37°C. By contrast, the ratio

of clusters with 13-16 molecules decreased after 5min 37°C incubation. An increase in the percentage of clusters with 9-12 molecules was observed in accordance with the decreases in the average cluster diameter (Figure 4.12 C, D). HIV-receptor binding at the plasma membrane induced an increase in local CD4 clustering around bound viral particles from surrounding clusters containing 1-4 molecules in the first 2min after warming to 37°C. Subsequently, the cluster containing large number of CD4 molecules declined and returned back to its original cluster forms, which contains smaller number of molecules, after 10mins at 37°C.

Figure 4.12 Counting of CD4 molecules after 2, 5 and 10min at 37ºC.

Molecular counting of colocalised areas (A) and all identified clusters (B) in all conditions. Bars indicate mean ± SEM. The data are from 15 different cell profiles in three separate experiments. ns p>0.05. ** p<0.01. **** p< 0.0001.

4.2.11 Analysis of the influence of CCR5 on HIV-induced CD4 clustering

To test whether the observed HIV induced CD4 clustering is CCR5 dependent, I used HIV treated SupT1 cells, which lack CCR5. HIV was bound to cells as above; the cells were warmed to 37°C for 1min, then processed and imaged as described above. Enlarged CD4 clusters were also detected in HIV treated SupT1 cells after 1min at 37°C but not in samples kept at 4°C (Figure 4.13 A). Quantitatively, the size of CD4 cluster in HIV associated areas was significantly larger (209 ± 16 nm) than in areas without virus (57 ± 9 nm) and on samples without 37°C incubation (CA 55 ± 11 nm vs NCA 57 ± 20 nm) (Figure 4.13 B). There was an increase in the frequency of clusters with 13-20 CD4 molecules in HIV associated areas (Figure 4.13 C). This trend was consistent with the distribution of the number of molecules per cluster in all identified clusters in both SupT1-R5 and SupT1 cells (Figure 4.13 D). The diameter of HIV associated CD4 clusters also increased, to larger extent than on cells with CCR5 expression (213 ± 8 nm vs 191 ± 6 nm; Figure 4.4 D). Thus, the initial HIV induced CD4 clustering appeared to be CCR5 independent.
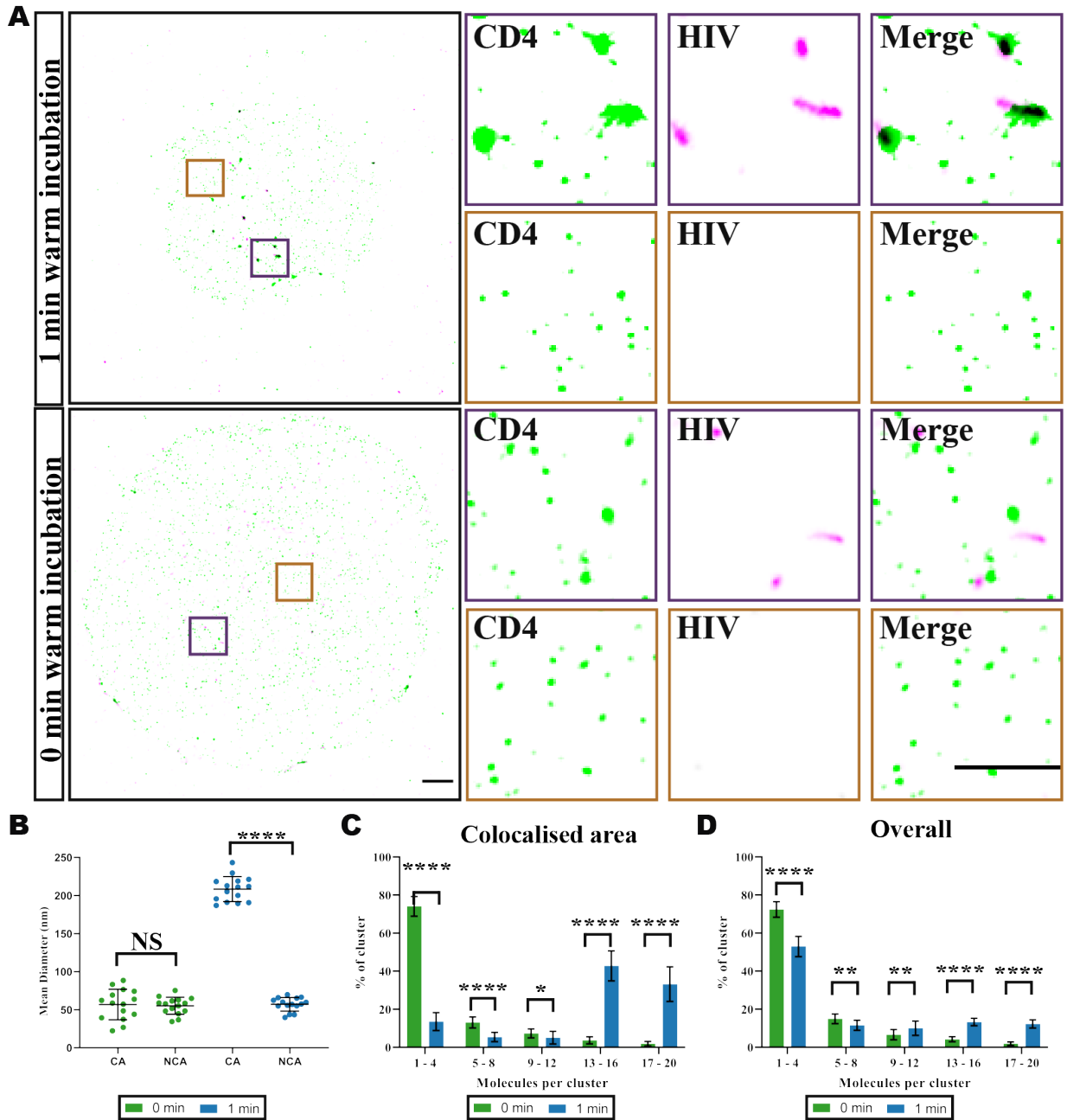
Figure 4.13 HIV-induced CD4 nanoscale organisation on SupT1 cells.

A. Representative TIRF-STORM images and insets of cell-surface CD4 (green) and HIV p24 (magenta) after 0 and 1min at 37°C. Scale bar = 2 μm. B. Quantification of CD4 cluster diameters in HIV associated areas and HIV negative areas after 0 and 1min at 37°C. CA represents HIV associated areas. NCA represents HIV negative areas. Each point represents the average CD4 cluster diameter on one cell. C and D. Molecular counting of CD4 molecules after 0 and 1min at 37°C. Molecular counting of colocalised areas (A) and all

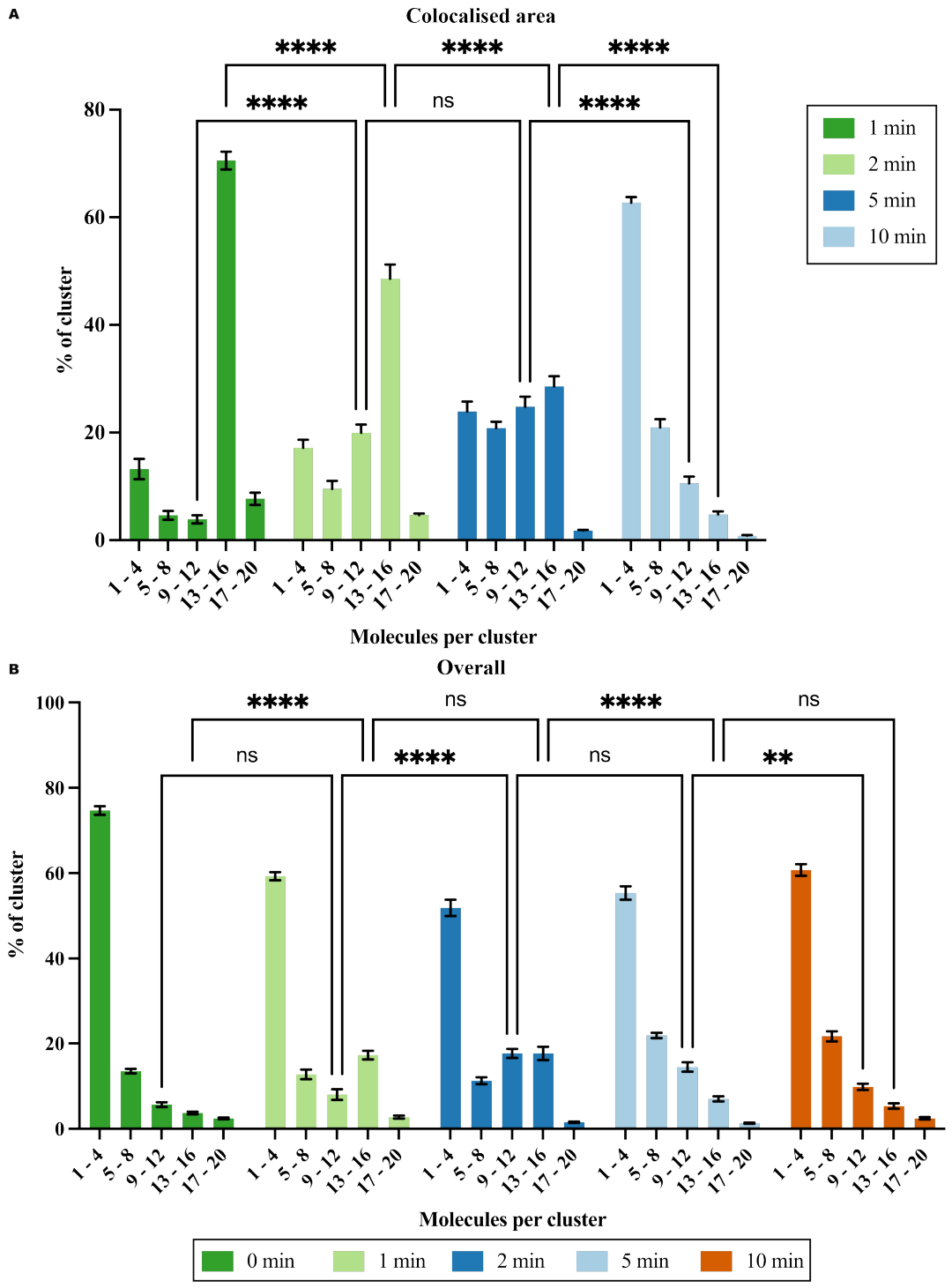identified clusters (B) in both conditions. 15 cell profiles were measured per condition. Bars indicate mean ± SD. The data are representative of at least three independent experiments. NS p>0.05. * p<0.05. ** p<0.01. **** p<0.0001.

4.3 Discussion

In this chapter, I applied the nanoscale labelling, imaging and quantitative analysis pipeline to investigate CD4 nanoscale (re-)organisations in response to HIV-1 binding. CD4 distribution showed a dynamic change at different timepoints post temperature shift. HIV induced local CD4 clustering started within 1min of 37°C incubation; and the clustering behaviour was inhibited by neutralising antibody Q4120 co-incubation. The mean diameter of CD4 clusters colocalised with HIV subsequently decreased over the following 2 -10 min of 37°C incubation. I also applied the molecular counting method to HIV treated SupT1-R5 cells. These experiments indicated that the increase in cluster size corresponded to an increase in CD4 molecules per cluster to an average of 13-16 in SupT1-R5 cells. This distinct pool of clusters containing 13-16 molecules was also significantly different from what would be expected in a random distribution predicted by statistical simulation. In addition, I comfirmed that the initial Env-CD4 interaction was CCR5-independent; The size of the CD4 clusters was also larger than those in SupT1-R5 cells with 13-20 molecules per cluster. Thus, using the established labelling, imaging and quantitative analysis pipeline, I found that HIV induced a reorganisation of cell surface CD4 molecules.

To set up the HIV binding assay, I first determined an optimal MOI for imaging experiments that balances cellular infectivity with the ability to image a reasonable frequency of virus particles. Previous studies from HIV infected patients and mathematical modelling suggest that 3-4 viruses internalise in an infected cell regardless of the cell type [308–311]. These events did not happen randomly [312]. Therefore, I suspected that the number of viruses that bind to a susceptible cell before fusion would be more than 3-4. This number needs to

be balanced with having a sufficient number of bound particles per FOV to ensure a workable throughput for quantitation in the imaging assays. I tested MOI, 10, 30 and 50 infectious units per cell. The average number of virus particles observed per cell were 2, 26 and 46, respectively (Figure 4.2). As a balance between experimental throughput and a physiologically relevant number of particles per cell, I chose the MOI of 30 as being optimal.

HIV fusion is a dynamic process estimated to take up to 15min after virus addition to cells at 37°C [262–265]. While the imaging was performed on fixed cells, it first required co-incubating HIV and labelling antibodies at the TAS state, releasing the temperature block, and sample fixation at different time points to trace the fusion process. Although previous studies reported that HIV can bind to cells with moderate CD4-specific association [303] at 4°C, whether incubation at 4°C alters CD4 organisation has never been validated at the nanoscale. I characterised CD4 organisation after HIV and labelling antibody co-incubation in cells with and without neutralising antibody Q4120 pre-treatment (Figure 4.3). CD4 cluster diameter showed no difference between HIV colocalised and non-colocalised areas on the same cell with or without neutralising antibody Q4120 treatment. This result indicated that HIV binding did not induce any detectable changes in CD4 organisation after incubation at 4°C. Interestingly, HIV virions were observed attached to cells even in conditions non-permissive for CD4 binding. This is consistent with previous studies indicating that HIV can bind to cells through interactions with adhesion proteins, such as integrins, lectins and syndycans [280,313–316]. This level of HIV-CD4 colocalisation has later been referred to as base level colocalisation.

With the established imaging and quantitative analysis pipeline and HIV binding assay, I characterised HIV induced CD4 reorganisation after 37°C incubation for up to 10 min. Analysing CD4 organisation by cluster diameters, a local induced CD4 cluster size to 191 nm ± 6 nm was observed in HIV-colocalised regions in CD4-HIV binding permissive condition. Meanwhile, CD4 clusters in non-colocalised regions in CD4-HIV binding permissive conditions remained the same as those in colocalised and non-colocalised regions in

CD4-HIV binding inhibition conditions (Figure 4.4). Around 83% ± 5% of HIV particles colocalised with CD4 in binding permissive conditions, which traces to enlarged CD4 clusters (Figure 4.5). By contrast, the binding for the non-permissive condition was 5% ± 2% (Figure 4.5). In the 2min 37°C incubation condition, the diameter of CD4 cluster in HIV colocalised areas showed a slight decrease in CD4 diameter to 162 ± 33 nm while there was no change in non-colocalised areas. There were fewer HIV colocalised with CD4 after 2min 37°C incubation. The decreasing trend continued up to 5min 37°C incubation to 105 ± 42 nm with 59% ± 12% of HIV-CD4 colocalisation. After 10min of HIV-CD4 association, the detected CD4 cluster size dropped back to the base level in colocalised areas and non-colocalised area(Figure 4.9). Moreover, the ratio of colocalisation between HIV and CD4 has also returned to the base level.

Little study has shown the HIV fusion process in the context of timescale and receptor organisation at nanoscale. For one of the first times, the time-series data in the study indicated that CD4 membrane organisation is a dynamic process during HIV fusion. A report suggested that HIV can expand to 130 nm after interacting with CD4 [210]. Comparing with results acquired in this study, after HIV-CD4 binding, a local accumulation of CD4 peaked at 1min on most HIV binding sites, which are around 1.5 times larger than an HIV particle. However, parts of HIV detached before 5min, which the lack of co-receptor CCR5 around might explain. A decrease in CD4 cluster diameter was shown in those sites still with HIV binding. In this case, CD4 cluster diameter reduced to be smaller than (0.8 times) a typical HIV particle. Until 10min, with a base level of HIV still colocalised with CD4, there was no difference in CD4 cluster diameter in both HIV colocalised and non-colocalised areas within the same cell. This is corresponding with the decreases of the overall number of HIV detected on the PM (Figure 4.11). Combining these results, the disassociation between Env and CD4 might be due to HIV-1 fusion, rather than moving onto coreceptor engagement.

Moreover, considering the measured density of CD4 molecules within the HIV-induced clusters (approximately 500 molecules/μm^2), the estimated inter-

molecular centre-to-centre distances for CD4 molecules was 40-50 nm. The distance is larger than the measured width of trimeric Env complexes as 10-15 nm [293,294,317,318]. This suggests that not all gp120 molecules on an individual Env spike engage CD4.

Estimated molecular counting is another aspect to characterise CD4 organisation upon HIV binding in the established pipeline. The changes in molecules per cluster are mainly in accordance with the trend of cluster diameters in HIV binding sites. An apparent pool of 13-16 molecules per cluster in HIV binding areas is coordinated with the increased diameter of CD4 clusters after 1min 37°C incubation (Figure 4.6). Hypothetically, the cluster of Envs on the mature virion has at least three Env proteins, thereby contains twelve gp120 proteins [290,291]. The 13-16 molecules per cluster we detected might indicate that single CD4 bound Env might not be sufficient for fusion. This peak is also shown in the overall distribution of molecule numbers per cluster in all identified clusters, which distinct molecule numbers per cluster in HIV treated cells to statistical simulated random distribution (Figure 6.7). This further confirms that the detected CD4 reorganisation cannot happen by chance.

Clusters containing 13-16 molecules per cluster gradually decrease after 2, 5 and 10min 37°C incubation while 1-8 molecules per cluster gradually increase for up to 10min. Interestingly, molecules per cluster at HIV binding largely returns to the base level with an increase of slightly larger cluster with 5-8 molecules per cluster after 10min (Figure 4.12). This results perhaps indicate that the clusters with formed through aggregation from surrounding smaller clusters that contains 1-8 molecules per cluster. And they disassociated and returned back as smaller clusters after gp120-Env engagement.

A previous study has characterised CD4 and CCR5 molecule numbers on COS-7 cells using HIV_{JR-FL} VLPs for up to 7 min [211]. They concluded an HIV-1 driven pre-fusion 3-step mechanism model. Using N&B methods, at 1.7 min CD4-Env intermediated binding, followed by additional 3 CD4 molecules to

bind to the Env trimer from 3.4 – 7 min. Meanwhile, the dimerisation of CCR5 results in the final pre-fusion complex, consisting of 4 CD4 and 2 CCR5 molecules per Env trimer. However, the authors further showed an average of 1 Env engaged with pre-fusion CD4 and CCR5 complexes, suggesting that potentially 1 Env is sufficient to trigger fusion [211]. Their findings are partially lined with what I found. Given that mature HIV particles have an average of 15 Env trimers per virion [165,166,283] that can be clustered in the viral envelop [290,291], my 1 min 37°C incubation data indicates that potentially the ratio of CD4:Env is at least 1:1, indicating that every Env will be bound to minimal of one CD4 for maximal fusion possibility in the intermediated binding step [211]. However, a decrease in molecule numbers per cluster was shown in this study in contrast with further recruitment of additional CD4 proteins. This difference might be due to the methods restriction where only 1 Env trimers can be studies at given timepoints rather than HIV as a whole in the other study [211]. Considering that not all Env-CD4 binding is essential for fusion and the proximity of nearby CD4 and Env, it is likely that Env-CD4 binding would switch dynamically within the following minutes. The apparent increase of clusters containing 5-8 molecules suggests that 2-3 Env trimer is bound with CD4 at a pre-fusion stage at 5min. It is worth noting that it remains difficult to estimate the precise Env-CD4 stoichiometry required and whether it directly links to successful fusion and entry. Nevertheless, my result indicates a more considerable biophysical influence for CD4 reorganisation and Env trimer clustering during HIV fusion.

The initial gp120-CD4 association is CCR5-independent (Figure 4.13). A slight increase in cluster diameter was detected in SupT1 cells compared to SupT1-R5 cells (209 ± 16 nm vs 191 ± 6 nm). This coordinates with the increase in CD4 clusters containing 17-20 molecules. From a downstream mechanistic point of view, although signalling via GPCR co-receptors has been identified as a cytoskeleton remodelling process for HIV to facilitate productive infection [294], reports are conflicts on whether GPCR-dependent signalling through CCR5 is essential for HIV entry [319,320]. The CCR5-independent CD4 clustering

within the 1min of 37°C incubation detected in this study suggests that HIV-induced signalling through CD4 and p56[Lck] can trigger CD4 clustering. Lck, as a lymphocyte-specific, Src-family tyrosine kinase, binds to CD4 directly on the plasma membrane. The binding indicates the signalling potential to CD4 and inhibits CD4 internalisation [267,321–323]. Moreover, Lck participates in filamin-A activation, resulting in enhanced F-actin cross-linking and artificial immune-synapse formation [324,325]. With the functional links between Lck and the cortex [326–328], Lck may impact the diffusive properties of CD4 [267]. Therefore, CD4-Lck signalling can potentially induce CD4 clustering in T cells. It is reported that CD4/Lck signalling is not essential for HIV infection in macrophages [306], indicating CD4/Lck signalling dependence in productive HIV fusion might be cell type dependent.

In conclusion, in this chapter, I have quantitatively characterised the dynamic CD4 reorganisation after HIV binding. The result thus far indicates that CD4 clustering around HIV-binding sites. These clusters dispersed over time potentially along with the process to further stages of fusion. Therefore, HIV-induced CD4 spatial reorganisation might link to their functional role during HIV binding and fusion. This contributes to our goal of better understanding how viruses spatially modulate cell-surface receptors to facilitate entry. These results also call for characterising co-receptor distribution behaviour to understand the fusion process in full, ideally in the context that the fusion timepoint can be real-time traced. Furthermore, these results provide evidence for another line of HIV entry inhibition assay through modifying spatial redistribution.

Chapter 5 Discussion and Conclusion

Cell PM serves as the primary interface between cells and extracellular signals and stimuli as well as the barrier for pathogens, such as invading viruses. Receptor engagement mediated the majority of these regulations. Growing body of evidence suggested that the organisation of receptors on the PM may serves as one of the regulatory factors in these finely controlled interactions [1]. To understand these events, imaging is essential. However, the detailed characterisation of these nanoscale spatial event remains limited largely due to the resolving power of CFM.

Using HIV-1 entry as a model, previous findings showed that differences in the number and organisation of Env on the virus membrane correlate with virus fitness [287,290,329–331]. Similarly, the stoichiometry of CD4 and CCR5, HIV receptor and coreceptor on the host cell, also appears to contribute to HIV infectivity [81,332–337]. However, there are still many outstanding unknowns to uncover due to the resolution limit of CFM. In particular, questions about the organisation and stoichiometry of key questions remain to be answered. Specifically, is there a preferred distribution and stoichiometry for HIV? Do the kinetic of virus-receptor engagement influence the location and mode of viral entry? How are Env-receptor complexes assembled? How does the entry kinetics vary between HIV isolates and cell types? Answers to these questions may also help determine the nature and properties of neutralising antibodies that inhibit HIV entry.

Previous studies have shown that mature HIV particles are 100-150 nm in diameter [338] while CD4 is organised into 200-500 nm membrane compartments in radius [192]. These dimensions are at or below the resolution of CFM. By contrast, EM, which increases the resolution, cannot provide information on dynamic events that occur in seconds to minutes. Therefore, to direct image receptor organisation and quantify protein kinetics at the scale of HIV-receptor interplay, technologies that combine the specific visualisation of

involved protein, quantitative assessments of protein numbers and identification of fusion sites are needed. SRM has become a bridge between quantitative molecule organisation characterisation and cellular biology studies. As one of the mainstream SRM methods, STORM technique becomes one of the optimal tools for studying protein kinetics and organisation on the nanoscale. It can achieve a resolution of ~20nm, produce coordinate maps with every localisation detected, and is compatible with spatial statistical analysis. Furthermore, TIRFM enables the analysis of fluorescent molecules within a few hundred nanometres close to the coverslip while being STORM compatible. Pipelines incorporating TIRF and STORM could be a potential candidate for quantitative characterising receptor organisational changes during HIV entry.

In this thesis, I set out to quantitatively characterise the dynamic organisation of CD4 during the early stages of viral engagement, focusing on R5-tropism (HIV$_{JR-CSF}$) [339,340]. Firstly, a validated imaging pipeline was established for visualising CD4 and CCR5 organisation, and organisational changes on SupT1-R5 cells, one of the models for the primary viral target cells. I then developed an analysis pipeline to characterise the imaging data quantitatively. I applied it to determine the size of CD4 and CCR5 clusters, the number of CD4 and CCR5 molecules per cluster, and the spatial correlation between CD4 and CCR5. Finally, the effect of HIV-1 binding on CD4 organisation for 1 - 10min was measured using the established pipeline.

The imaging and analytical pipeline I established provides a powerful and robust toolbox to study HIV entry and the properties of other virus-receptor systems and membrane proteins in general. In this pipeline, samples are first incubated at 4°C for pre-binding before returning to 37°C for a specific period and reactions were stopped by rapid cooling and chemical fixation. The labelled samples were then imaged using the TIRF-STORM technique. Localisations were detected and recorded from over 15000 frames as a coordinate map and then used for SR image reconstruction and quantitative analysis. The output parameters include cluster size, the number of molecules

per cluster, as well as spatial characterisation between channels, such as percentage of colocalisation and features of clusters in colocalised/non colocalised regions of each channel (Figure 5.1).
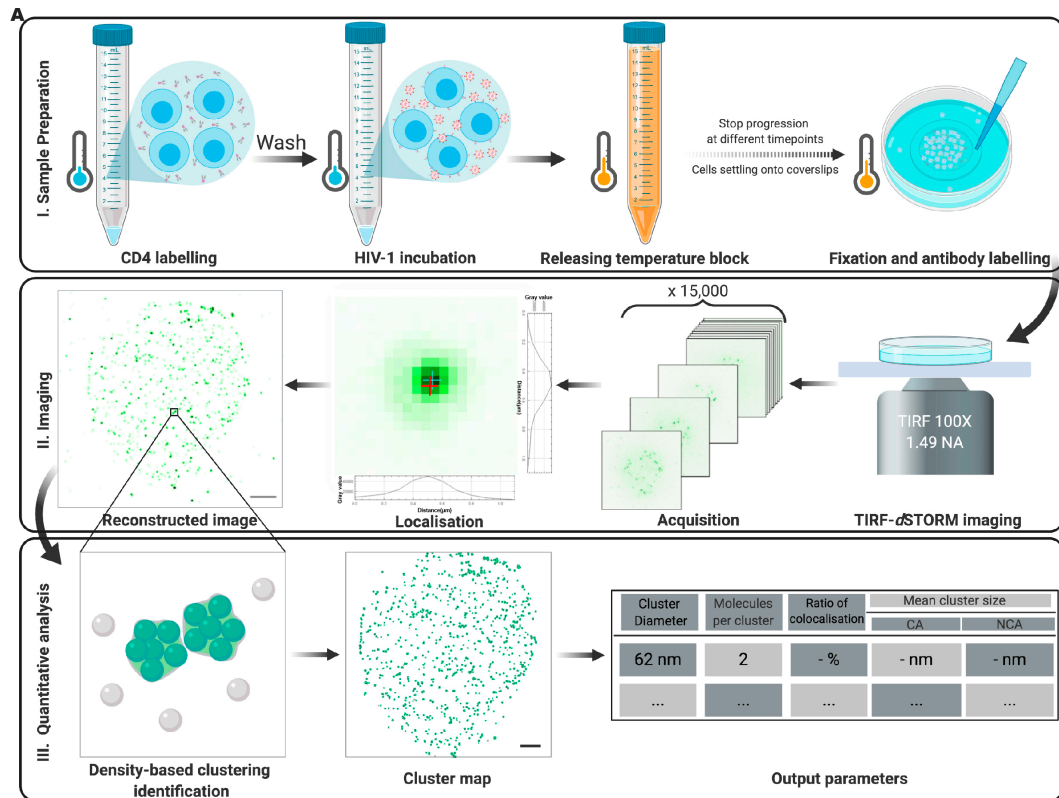
Figure 5.1 Schematics of the visualisation and quantitative analysis pipeline used in this study.

I. Sample Preparation. SupT1-R5 cells were pre-incubated at 4°C with antibodies and HIV-1 before a quick release of the temperature block and rapid cooling before fixation. II. Imaging. Collected and labelled cells deposited on imaging surfaces were imaged using a standard TIRF-STORM acquisition, and III. Quantitative analysis. localisations were used for density-based cluster analysis and molecular counting.

Chapters 3 described the establishment and validation of the imaging and analytical pipeline, focusing on visualisation and quantitative analysis. Starting from approaches used for sample preparation, CD4 organisation under different labelling conditions was compared. My results showed that pre- and

post-fixation labelling and primary antibody labelling alone did not lower labelling efficacy nor alter CD4 distribution (Figure 3.8, Figure 3.9; Figure 3.10, Figure 3.11). Furthermore, no significant change was detected in CD4 cluster diameter in samples with up to 15 min 37°C incubation before fixation (Figure 3.12, Figure 3.13). This indicated that pre-fixation labelling samples with a fluorophore-conjugated primary antibody for up to 15 min at 37°C is suitable for use in the pipeline.

For cluster analysis, two widely-used SR cluster analysis methods were tested and compared with manually annotated data. Clus-DoC [115], a platform that incorporated DBSCAN and CDC based colocalisation analysis, stands out because the features of identified clusters best mimic those of the manual annotation (Figure 3.3). For molecular counting, immobilised AlexaFluor 647 conjugated OKT4 was used to calibrate photoswitching kinetics. Calibration algorithms used were adopted from Sieben et al. [227]. The measured imaging precision was ~15nm with an average dark-time of 10 frames (Figure 3.4, Figure 3.5). The pipeline was further extended to characterise the spatial relationship between two channels quantitatively. Fiducial beads imaged under the same experimental conditions were used for chromatic aberrations and quantitative cross-channel alignment threshold validation (Figure 3.6, Figure 3.7). A colour swap experiment was then used to validate that the chosen fluorophores (AlexaFluor 647 and AlexaFluor 568) were compatible with the pipeline and don't change CD4 or CCR5 distribution (Figure 3.14, Figure 3.15).

Finally, PMA treatment was used to validate the pipeline's capability for detecting nanoscale organisational changes. PMA is believed to trigger the endocytic uptake of CD4 and induces bulk CD4 redistribution on the PM [81]. I verified that the established pipeline could visualise these organisational changes (Figure 3.16, Figure 3.17). Further quantitative analysis indicated that the scale of change detected ranges from tens to hundreds of nanometres. Overall, the visualisation and quantitative analysis pipeline developed in this study were found to provide a robust methodology to analyse the nanoscale

organisation of labelled PM proteins with sensitivity to detect changes within tens of nanometres.

A biological application for the pipeline I developed is shown in Chapter 4 – an investigation of the effect of HIV binding on CD4 distribution. The MOI of 30 was chosen as the optimal balance between physiological relevance and pipeline compatibility (Figure 4.2). Under TAS, no HIV associated changes in CD4 distribution were detected (Figure 4.3). However, a striking increase in HIV colocalised CD4 was detected after 1min at 37°C (Figure 4.4, Figure 4.5, Figure 4.6, Figure 4.7), both in cluster size and the number of molecules per cluster. This reorganisation did not occur randomly and was distinct from a simulated random distribution (Figure 4.8). The initial Env-CD4 organisational change seems to be CCR5 independent (Figure 4.13). The impact of HIV binding on CD4 organisation for more prolonged periods was also tested. Quantitative analysis showed that HIV binding increased local CD4 clustering around bound viral particles for around 2min; subsequently, these clusters dispersed, and the distribution returned to that seen on untreated cells by 10min at 37°C (Figure 4.9, Figure 4.10, Figure 4.11, Figure 4.12).

Taken together, the reorganisation of CD4 following HIV binding I observed provides exciting insights into the potential functions of the organisational changes of the receptor during virus entry. The fast changes upon temperature shift would seem partly to be induced by physical forces imposed by HIV binding, with the pulling force from Env clusters seen on mature HIV particles [290,329]. The maximum diameter CD4 clusters was about 1.5 times the size of a typical HIV particle (191 nm *vs* 120 nm), even when a proposed increase in HIV particle size upon receptor binding (134 nm) seen under cryo-EM is taken into consideration [210]. This suggests that CD4 clustering is not driven by Env engagement alone and implies a role of biochemical signalling across the cell surface. Understanding the nature of this signalling might suggest novel ways to inhibit CD4 clustering that could impact the efficiency of HIV entry.

More pipeline improvements and experimental investigations are necessary to provide an explicit answer to the larger question about the exact number and organisation of CD4 and CCR5 required for efficient HIV entry. From the pipeline point of view, the development of high-affinity CCR5 mAbs that do not interfere with HIV binding is required to further characterise CCR5 organisation, which is essential to elucidate HIV-1 entry fully. One of the possibilities would be to carefully validate whether CCR5 genetically tagged with GFP, as used in previous studies [341,342], would accurately report the biological properties of native, untagged CCR5 in CD4+ T cells. If tagging does not perturb CCR5 properties, SR compatible tags, such as SNAP- [343], CLIP- [344] and Halo-Tag [345], might be used. These are proteins to which fluorophore-conjugated probes can bind. It is also easily adaptable to the current imaging and quantitative analysis pipeline.

Second, the molecular numbers acquired in the current study should only be viewed as estimates. A method(s) that provides insight into the exact number of molecules is still in need. As discussed in Chapter 1.2.4.3, the precision of molecular counting can be increased through qPAINT [145]. In this variant of SMLM, blinking can be achieved by transient binding between dye labelled probes. This approach circumvents the need for stochastic chemical photoswitching and is resistant to photobleaching due to the abundant source of free-floating probes. Furthermore, the number of molecules can be precisely calculated by predictable DNA binding kinetics [147]. qPAINT methods are also compatible with labelling protein fused with SNAP- [343], CLIP- [344] and Halo-tags [345], namely tagPAINT [346]. The main limitations for the application of qPAINT are the availability of appropriate secondary antibodies and the extended imaging time. In the context of the current study, the availability of secondary antibodies from different species would not be the restriction factor if SR compatible tags is incorporated. However, by doing qPAINT, the throughput of this study will still be influenced due to the increased imaging time.

Moreover, there is still a lack of direct visualisation approaches to support the notion that these captured CD4 organisational changes are precursors to HIV

fusion. CypA-DsRed and INsfGFP double labelled HIV particles are currently used for tracing viral fusion at the single virion level. The marker CypA-DsRed is *Discosoma sp.* Red fluorescent protein fused at the carboxy-terminal domain of cyclophilin A [347]. It is incorporated into virions by binding to CA with high-affinity , and the infectivity of tagged HIV is not affected in TZM-bl, or Jurkat T cells [348–352]. The loss of CypA-DsRed signal reports the loss of CA from the post-fusion cores co-labelled with integrase-superfoldedGFP [347]. This approach is robust in time-resolved imaging of HIV uncoating. It showed that more than 95% of viral cores uncoated within 90 min after infection [347]. However, it is less suitable to study early-stage fusion events like that in this study. Therefore, the development of another fusion reporting assay with the single virion detection capability is required to recognise HIV fusion sites within the first few minutes of binding.

Further work is also required to understand the mechanisms under which receptor organisational changes occur, through physical forces or biochemical signalling. Physical forces could be imposed by the mass of HIV on the host cell membrane. The physical association of CD4 through multiple interactions with a trimeric Env complex in the case of an intact virus could also contribute partially to the clustering observed in this study. However, the size of enlarged CD4 clusters we observed is beyond the virion size, this suggesting that both mechanisms are likely to be involved.

To investigate the potential biochemical signalling involved, in particular, to look into the actin cortex and endocytic machinery such as clathrin and adaptor proteins. A clearer understanding of whether changes in receptor cluster morphology corresponds to alteration in local actin cortex density or association with endocytic machinery and their according timing, would inform interpretation of the receptor dynamics observed in this study. These would also build on the current understanding of receptor signalling responses and their role in HIV infection [293,294,319]. Therefore, it would be interesting to investigate the effect of immobilising receptors or reducing the number of receptors on the plasma membrane on CD4 cluster size after HIV binding. It

could be done through drug treatment (such as DNP, 2,4-dinitrophenol [353]) or genomic editing/Knock-down Filamin-A. As one of the highest upregulate genes upon HIV infection, siRNA treatment in target cells strongly reduced receptor co-capping and infection by inbound cell-free virus under CFM [293].

Overall, potential models to explain the dynamic process through both physical forces and biochemical signaling pathways would be a 'CD4 centred' model (Figure 5.2). After HIV binds to CD4, CD4 accumulates around the virus to form a larger cluster than the virus to allow maximal binding between Env and CD4 via biochemical recruitment. The Env-CD4 disassociation detected in the study from 2 min could be in favor of fusion (Figure 5.3). The Env-CD4 complex potentially undergoes conformational changes and bends to an orientation almost in parallel with the viral membrane, presumably directing the virus to where it is enriched in the coreceptor. This allows further Env-CD4-CCR5 interaction, as shown in EM data (Figure 1.9) [170]. Furthermore, as CCR5 tend to localise at the junction region between lipid ordered and lipid disorder domain, which is also the preference fusion site for HIV-1 [222].
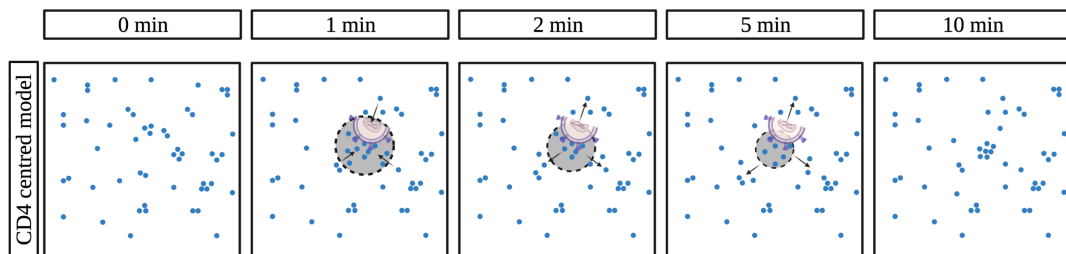
Figure 5.2 Schematic of the 'CD4-centered' model (lower half) of the organisation of CD4 during HIV fusion.

Shadows indicate the cluster seen in reconstructed images. Arrow indicates the direction of CD4 movements.
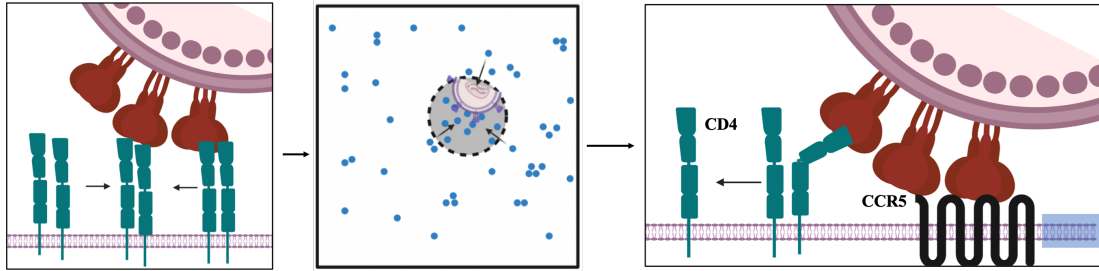
Figure 5.3 Schematic of CD4 conformational changes 1 min after Env binding.

The blue shadow indicates the lipid disordered domain.

Overall, this work provides a validated visualisation and quantitative pipeline for characterising nanoscale receptor organisation and estimate the number of molecules using SRM and associated statistical analytical tools. This pipeline provides a robust scaffold to study virus entry and the properties of other ligand-receptor systems and membrane proteins in general with great customisable potential. It contributes to better understanding how viruses spatially modulate cell-surface receptors to facilitate their entry. Under current climate, it might be of immediate use for studying the determinants of the prevalent pathway for SARS-CoV-2 entry in specific cell lines from an organisational point of view. After binding to the cellular receptor angiotensin converting enzyme 2 (ACE2), it is shown that SARS-CoV-2 enters target cells either via direct fusions triggered by transmembrane protease serine 2 (TMPRSS2) or the endocytic pathway within the endosomal-lysosomal compartments [354–357]. By comparing the organisational changes of receptors among different cell lines, it might be possible to identify a clear-cut situation where distinct pathways are used, which could inform the choice of cell line or model systems to conduct drug screen and the intervention strategies.

References

1. Grecco, H. E., Schmick, M. & Bastiaens, P. I. H. Signaling from the Living Plasma Membrane. *Cell* **144**, 897–909 (2011).
2. Miosge, L. & Zamoyska, R. Signalling in T-cell development: is it all location, location, location? *Curr. Opin. Immunol.* **19**, 194–199 (2007).
3. Hung, M.-C. & Link, W. Protein localization in disease and therapy. *J. Cell Sci.* **124**, 3381–3392 (2011).
4. Cebecauer, M., Spitaler, M., Sergé, A. & Magee, A. I. Signalling complexes and clusters: functional advantages and methodological hurdles. *J. Cell Sci.* **123**, 309–320 (2010).
5. Nussinov, R. The spatial structure of cell signaling systems. *Phys. Biol.* **10**, 045004 (2013).
6. Garcia-Parajo, M. F., Cambi, A., Torreno-Pina, J. A., Thompson, N. & Jacobson, K. Nanoclustering as a dominant feature of plasma membrane organization. *J. Cell Sci.* **127**, 4995–5005 (2014).
7. Bernardino de la Serna, J., Schütz, G. J., Eggeling, C. & Cebecauer, M. There Is No Simple Model of the Plasma Membrane Organization. *Front. Cell Dev. Biol.* **4**, (2016).
8. van Meer, G. & de Kroon, A. I. P. M. Lipid map of the mammalian cell. *J. Cell Sci.* **124**, 5–8 (2011).
9. Dupuy, A. D. & Engelman, D. M. Protein area occupancy at the center of the red blood cell membrane. *Proc. Natl. Acad. Sci.* **105**, 2848–2852 (2008).
10. McLaughlin, S. & Murray, D. Plasma membrane phosphoinositide organization by protein electrostatics. *Nature* **438**, 605–611 (2005).
11. Berrier, A. L. & Yamada, K. M. Cell–matrix adhesion. *J. Cell. Physiol.* **213**, 565–573 (2007).
12. Singer, S. J. & Nicolson, G. L. The fluid mosaic model of the structure of cell membranes. *Science* **175**, 720–731 (1972).
13. Luby-Phelps, K. *et al.* A novel fluorescence ratiometric method confirms the low solvent viscosity of the cytoplasm. *Biophys. J.* **65**, 236–242 (1993).
14. Peters, R. & Cherry, R. J. Lateral and rotational diffusion of bacteriorhodopsin in lipid bilayers: experimental test of the Saffman-Delbrück equations. *Proc. Natl. Acad. Sci.* **79**, 4317–4321 (1982).
15. Chazotte, B. & Hackenbrock, C. R. The multicollisional, obstructed, long-range diffusional nature of mitochondrial electron transport. *J. Biol. Chem.* **263**, 14359–14367 (1988).
16. Frick, M., Schmidt, K. & Nichols, B. J. Modulation of Lateral Diffusion in the Plasma Membrane by Protein Density. *Curr. Biol.* **17**, 462–467 (2007).
17. Saxton, M. J. A Biological Interpretation of Transient Anomalous Subdiffusion. II. Reaction Kinetics. *Biophys. J.* **94**, 760–771 (2008).
18. Saffman, P. G. & Delbrück, M. Brownian motion in biological membranes. *Proc. Natl. Acad. Sci.* **72**, 3111–3113 (1975).
19. Marsh, D. Chapter 2 The nature of the lipid-protein interface and the influence of protein structure on protein-lipid interactions. in *New*

Comprehensive Biochemistry (ed. Watts, A.) vol. 25 41–66 (Elsevier, 1993).

20. Mouritsen, O. G. & Bloom, M. Models of Lipid-Protein Interactions in Membranes. *Annu. Rev. Biophys. Biomol. Struct.* **22**, 145–171 (1993).
21. Anderson, R. G. W. & Jacobson, K. A Role for Lipid Shells in Targeting Proteins to Caveolae, Rafts, and Other Lipid Domains. *Science* (2002) doi:10.1126/science.1068886.
22. Kaiser, H.-J. *et al.* Lateral sorting in model membranes by cholesterol-mediated hydrophobic matching. *Proc. Natl. Acad. Sci.* **108**, 16628–16633 (2011).
23. DePierre, J. W. & Karnovsky, M. L. PLASMA MEMBRANES OF MAMMALIAN CELLS : A Review of Methods for Their Characterization and Isolation. *J. Cell Biol.* **56**, 275–303 (1973).
24. Shimshick, E. J. & McConnell, H. M. Lateral phase separation in phospholipid membranes. *Biochemistry* **12**, 2351–2360 (1973).
25. van Meer, G., Gumbiner, B. & Simons, K. The tight junction does not allow lipid molecules to diffuse from one epithelial cell to the next. *Nature* **322**, 639–641 (1986).
26. Karnovsky, M. J. *et al.* Lipid Domains in Membranes*. *Ann. N. Y. Acad. Sci.* **401**, 61–74 (1982).
27. Simons, K. & Ikonen, E. Functional rafts in cell membranes. *Nature* **387**, 569–572 (1997).
28. Pike, L. J. Rafts defined: a report on the Keystone Symposium on Lipid Rafts and Cell Function. *J. Lipid Res.* **47**, 1597–1598 (2006).
29. Eggeling, C. *et al.* Direct observation of the nanoscale dynamics of membrane lipids in a living cell. *Nature* **457**, 1159–1162 (2009).
30. Owen, D. M., Williamson, D. J., Magenau, A. & Gaus, K. Sub-resolution lipid domains exist in the plasma membrane and regulate protein diffusion and distribution. *Nat. Commun.* **3**, 1256 (2012).
31. Brameshuber, M. *et al.* Imaging of Mobile Long-lived Nanoplatforms in the Live Cell Plasma Membrane*. *J. Biol. Chem.* **285**, 41765–41771 (2010).
32. Honigmann, A. *et al.* Scanning STED-FCS reveals spatiotemporal heterogeneity of lipid interaction in the plasma membrane of living cells. *Nat. Commun.* **5**, 5412 (2014).
33. Sevcsik, E. *et al.* GPI-anchored proteins do not reside in ordered domains in the live cell plasma membrane. *Nat. Commun.* **6**, 6969 (2015).
34. Fujita, A. *et al.* Gangliosides GM1 and GM3 in the Living Cell Membrane Form Clusters Susceptible to Cholesterol Depletion and Chilling. *Mol. Biol. Cell* **18**, 2112–2122 (2007).
35. Chen, Y., Qin, J. & Chen, Z. W. Fluorescence-topographic NSOM directly visualizes peak-valley polarities of GM1/GM3 rafts in cell membrane fluctuations*. *J. Lipid Res.* **49**, 2268–2275 (2008).
36. Amaro, M. *et al.* GM1 Ganglioside Inhibits β-Amyloid Oligomerization Induced by Sphingomyelin. *Angew. Chem. Int. Ed.* **55**, 9411–9415 (2016).

37. Zanten, T. S. van *et al.* Direct mapping of nanoscale compositional connectivity on intact cell membranes. *Proc. Natl. Acad. Sci.* **107**, 15437–15442 (2010).

38. Sezgin, E., Levental, I., Mayor, S. & Eggeling, C. The mystery of membrane organization: composition, regulation and roles of lipid rafts. *Nat. Rev. Mol. Cell Biol.* **18**, 361–374 (2017).

39. Murase, K. *et al.* Ultrafine Membrane Compartments for Molecular Diffusion as Revealed by Single Molecule Techniques. *Biophys. J.* **86**, 4075–4093 (2004).

40. Andrade, D. M. *et al.* Cortical actin networks induce spatio-temporal confinement of phospholipids in the plasma membrane – a minimally invasive investigation by STED-FCS. *Sci. Rep.* **5**, 11454 (2015).

41. Mueller, V. *et al.* STED Nanoscopy Reveals Molecular Details of Cholesterol- and Cytoskeleton-Modulated Lipid Interactions in Living Cells. *Biophys. J.* **101**, 1651–1660 (2011).

42. Dustin, M. L. & Choudhuri, K. Signaling and Polarized Communication Across the T Cell Immunological Synapse. *Annu. Rev. Cell Dev. Biol.* **32**, 303–325 (2016).

43. Hellen, E. H. & Axelrod, D. Kinetics of epidermal growth factor/receptor binding on cells measured by total internal reflection/fluorescence recovery after photobleaching. *J. Fluoresc.* **1**, 113–128 (1991).

44. Zhou, Y. & Hancock, J. F. Ras nanoclusters: Versatile lipid-based signaling platforms. *Biochim. Biophys. Acta* **1853**, 841–849 (2015).

45. Varma, R. & Mayor, S. GPI-anchored proteins are organized in submicron domains at the cell surface. *Nature* **394**, 798–801 (1998).

46. Zanten, T. S. van *et al.* Hotspots of GPI-anchored proteins and integrin nanoclusters function as nucleation sites for cell adhesion. *Proc. Natl. Acad. Sci.* **106**, 18557–18562 (2009).

47. Jacobson, K., Liu, P. & Lagerholm, B. C. The lateral organization and mobility of plasma membrane components. *Cell* **177**, 806–819 (2019).

48. Gowrishankar, K. *et al.* Active remodeling of cortical actin regulates spatiotemporal organization of cell surface molecules. *Cell* **149**, 1353–1367 (2012).

49. Lin, B. *et al.* Lipid rafts sense and direct electric field-induced migration. *Proc. Natl. Acad. Sci.* **114**, 8568–8573 (2017).

50. Kusumi, A. *et al.* Dynamic organizing principles of the plasma membrane that regulate signal transduction: commemorating the fortieth anniversary of Singer and Nicolson's fluid-mosaic model. *Annu. Rev. Cell Dev. Biol.* **28**, 215–250 (2012).

51. Freeman, S. A. *et al.* Transmembrane Pickets Connect Cyto- and Pericellular Skeletons Forming Barriers to Receptor Engagement. *Cell* **172**, 305-317.e10 (2018).

52. Fujiwara, T. K. *et al.* Confined diffusion of transmembrane proteins and lipids induced by the same actin meshwork lining the plasma membrane. *Mol. Biol. Cell* **27**, 1101–1119 (2016).

53. Fujiwara, T., Ritchie, K., Murakoshi, H., Jacobson, K. & Kusumi, A. Phospholipids undergo hop diffusion in compartmentalized cell membrane. *J. Cell Biol.* **157**, 1071–1082 (2002).

54. Sadegh, S., Higgins, J. L., Mannion, P. C., Tamkun, M. M. & Krapf, D. Plasma Membrane is Compartmentalized by a Self-Similar Cortical Actin Meshwork. *Phys. Rev. X* **7**, 011031 (2017).

55. Lee, S., Tan, H. Y., Geneva, I. I., Kruglov, A. & Calvert, P. D. Actin filaments partition primary cilia membranes into distinct fluid corrals. *J. Cell Biol.* **217**, 2831–2849 (2018).

56. Kusumi, A., Ike, H., Nakada, C., Murase, K. & Fujiwara, T. Single-molecule tracking of membrane molecules: plasma membrane compartmentalization and dynamic assembly of raft-philic signaling molecules. *Semin. Immunol.* **17**, 3–21 (2005).

57. Suzuki, K. G. N., Fujiwara, T. K., Edidin, M. & Kusumi, A. Dynamic recruitment of phospholipase C gamma at transiently immobilized GPI-anchored receptor clusters induces IP3-Ca2+ signaling: single-molecule tracking study 2. *J. Cell Biol.* **177**, 731–742 (2007).

58. Smith, B. A., Clark, W. R. & McConnell, H. M. Anisotropic molecular motion on cell surfaces. *Proc. Natl. Acad. Sci. U. S. A.* **76**, 5641–5644 (1979).

59. Jaqaman, K. *et al.* Cytoskeletal control of CD36 diffusion promotes its receptor and signaling function. *Cell* **146**, 593–606 (2011).

60. Hashimoto-Tane, A. *et al.* Dynein-driven transport of T cell receptor microclusters regulates immune synapse formation and T cell activation. *Immunity* **34**, 919–931 (2011).

61. Monks, C. R. F., Freiberg, B. A., Kupfer, H., Sciaky, N. & Kupfer, A. Three-dimensional segregation of supramolecular activation clusters in T cells. *Nature* **395**, 82–86 (1998).

62. Grakoui, A. *et al.* The Immunological Synapse: A Molecular Machine Controlling T Cell Activation. *Science* (1999) doi:10.1126/science.285.5425.221.

63. Dustin, M. L. & Cooper, J. A. The immunological synapse and the actin cytoskeleton: molecular hardware for T cell signaling. *Nat. Immunol.* **1**, 23–29 (2000).

64. Kumari, S. *et al.* T Lymphocyte Myosin IIA is Required for Maturation of the Immunological Synapse. *Front. Immunol.* **3**, (2012).

65. Yokosuka, T. & Saito, T. The Immunological Synapse, TCR Microclusters, and T Cell Activation. in *Immunological Synapse* (eds. Saito, T. & Batista, F. D.) 81–107 (Springer, 2010). doi:10.1007/978-3-642-03858-7_5.

66. Varma, R., Campi, G., Yokosuka, T., Saito, T. & Dustin, M. L. T Cell Receptor-Proximal Signals Are Sustained in Peripheral Microclusters and Terminated in the Central Supramolecular Activation Cluster. *Immunity* **25**, 117–127 (2006).

67. Freiberg, B. A. *et al.* Staging and resetting T cell activation in SMACs. *Nat. Immunol.* **3**, 911–917 (2002).

68. Garcia, E. & Ismail, S. Spatiotemporal Regulation of Signaling: Focus on T Cell Activation and the Immunological Synapse. *Int. J. Mol. Sci.* **21**, 3283 (2020).

69. Saito, T. & Yokosuka, T. Immunological synapse and microclusters: the site for recognition and activation of T cells. *Curr. Opin. Immunol.* **18**, 305–313 (2006).

70. Lillemeier, B. F. *et al.* TCR and Lat are expressed on separate protein islands on T cell membranes and concatenate during activation. *Nat. Immunol.* **11**, 90–96 (2010).

71. Purbhoo, M. A. *et al.* Dynamics of Subsynaptic Vesicles and Surface Microclusters at the Immunological Synapse. *Sci. Signal.* (2010) doi:10.1126/scisignal.2000645.

72. Hsu, C.-J. & Baumgart, T. Spatial Association of Signaling Proteins and F-Actin Effects on Cluster Assembly Analyzed via Photoactivation Localization Microscopy in T Cells. *PLOS ONE* **6**, e23586 (2011).

73. Sherman, E. *et al.* Functional Nanoscale Organization of Signaling Molecules Downstream of the T Cell Antigen Receptor. *Immunity* **35**, 705–720 (2011).

74. Rossy, J., Owen, D. M., Williamson, D. J., Yang, Z. & Gaus, K. Conformational states of the kinase Lck regulate clustering in early T cell signaling. *Nat. Immunol.* **14**, 82–89 (2013).

75. Neve-Oz, Y., Razvag, Y., Sajman, J. & Sherman, E. Mechanisms of localized activation of the T cell antigen receptor inside clusters. *Biochim. Biophys. Acta BBA - Mol. Cell Res.* **1853**, 810–821 (2015).

76. Barr, V. A. *et al.* Development of nanoscale structure in LAT-based signaling complexes. *J. Cell Sci.* **129**, 4548–4562 (2016).

77. Yi, J., Balagopalan, L., Nguyen, T., McIntire, K. M. & Samelson, L. E. TCR microclusters form spatially segregated domains and sequentially assemble in calcium-dependent kinetic steps. *Nat. Commun.* **10**, 277 (2019).

78. *Jenaische Zeitschrift Für Naturwissenschaft.* (Gustav Fischer, 1874).

79. England), B. N. S. (Bristol. *Proceedings of the Bristol Naturalists' Society.* (The Society, 1876).

80. Rayleigh. XXXI. Investigations in optics, with special reference to the spectroscope. *Lond. Edinb. Dublin Philos. Mag. J. Sci.* **8**, 261–274 (1879).

81. Jacobs, C. A. The nanoscale organisation of HIV cell surface receptors CD4 and CCR5. *Doctoral thesis, UCL (University College London).* (UCL (University College London), 2018).

82. Török, P. & Wilson, T. Rigorous theory for axial resolution in confocal microscopes. *Opt. Commun.* **137**, 127–135 (1997).

83. Zipfel, W. R., Williams, R. M. & Webb, W. W. Nonlinear magic: multiphoton microscopy in the biosciences. *Nat. Biotechnol.* **21**, 1369–1377 (2003).

84. Erni, R., Rossell, M. D., Kisielowski, C. & Dahmen, U. Atomic-resolution imaging with a sub-50-pm electron probe. *Phys. Rev. Lett.* **102**, 096101 (2009).

85. Gustafsson, M. G. L. Surpassing the lateral resolution limit by a factor of two using structured illumination microscopy. *J. Microsc.* **198**, 82–87 (2000).

86. Schermelleh, L. *et al.* Subdiffraction Multicolor Imaging of the Nuclear Periphery with 3D Structured Illumination Microscopy. *Science* (2008) doi:10.1126/science.1156947.

87. Hell, S. W. & Wichmann, J. Breaking the diffraction resolution limit by stimulated emission: stimulated-emission-depletion fluorescence microscopy. *Opt. Lett.* **19**, 780–782 (1994).

88. Thorley, J. A., Pike, J. & Rappoport, J. Z. Chapter 14 - Super-resolution Microscopy: A Comparison of Commercially Available Options. in *Fluorescence Microscopy* (eds. Cornea, A. & Conn, P. M.) 199–212 (Academic Press, 2014). doi:10.1016/B978-0-12-409513-7.00014-2.

89. Rust, M. J., Bates, M. & Zhuang, X. Sub-diffraction-limit imaging by stochastic optical reconstruction microscopy (STORM). *Nat. Methods* **3**, 793–795 (2006).

90. Betzig, E. *et al.* Imaging Intracellular Fluorescent Proteins at Nanometer Resolution. *Science* **313**, 1642–1645 (2006).

91. Pereira, P. M., Almada, P. & Henriques, R. Chapter 7 - High-content 3D multicolor super-resolution localization microscopy. in *Methods in Cell Biology* (ed. Paluch, E. K.) vol. 125 95–117 (Academic Press, 2015).

92. Kner, P., Chhun, B. B., Griffis, E. R., Winoto, L. & Gustafsson, M. G. L. Super-resolution video microscopy of live cells by structured illumination. *Nat. Methods* **6**, 339–342 (2009).

93. Funatsu, T., Harada, Y., Tokunaga, M., Saito, K. & Yanagida, T. Imaging of single fluorescent molecules and individual ATP turnovers by single myosin molecules in aqueous solution. *Nature* **374**, 555–559 (1995).

94. Axelrod, D., Thompson, N. L. & Burghardt, T. P. Total internal inflection fluorescent microscopy. *J. Microsc.* **129**, 19–28 (1983).

95. Fish, K. N. Total internal reflection fluorescence (TIRF) microscopy. *Curr. Protoc. Cytom.* **Chapter 12**, Unit12.18 (2009).

96. Drenan, R. M. *et al.* Subcellular trafficking, pentameric assembly, and subunit stoichiometry of neuronal nicotinic acetylcholine receptors containing fluorescently labeled alpha6 and beta3 subunits. *Mol. Pharmacol.* **73**, 27–41 (2008).

97. Fan, Z. & Jin, W. A method for visualization of biomolecules labeled by a single quantum dot in living cells by a combination of total internal reflection fluorescence microscopy and intracellular fluorescence microscopy. *Talanta* **72**, 1114–1122 (2007).

98. Riven, I., Iwanir, S. & Reuveny, E. GIRK Channel Activation Involves a Local Rearrangement of a Preformed G Protein Channel Complex. *Neuron* **51**, 561–573 (2006).

99. Henriques, R., Griffiths, C., Hesper Rego, E. & Mhlanga, M. M. PALM and STORM: unlocking live-cell super-resolution. *Biopolymers* **95**, 322–331 (2011).

100. Coltharp, C., Yang, X. & Xiao, J. Quantitative analysis of single-molecule superresolution images. *Curr. Opin. Struct. Biol.* **0**, 112–121 (2014).

101. Cover, T. & Hart, P. Nearest neighbor pattern classification. *IEEE Trans Inf Theory* (1967) doi:10.1109/TIT.1967.1053964.

102. Ripley, B. D. Modelling Spatial Patterns. *J. R. Stat. Soc. Ser. B Methodol.* **39**, 172–212 (1977).

103. Owen, D. M. *et al.* PALM imaging and cluster analysis of protein heterogeneity at the cell surface. *J. Biophotonics* **3**, 446–454 (2010).

104. Kiskowski, M. A., Hancock, J. F. & Kenworthy, A. K. On the use of Ripley's K-function and its derivatives to analyze domain size. *Biophys. J.* **97**, 1095–1103 (2009).

105. Sengupta, P. *et al.* Probing protein heterogeneity in the plasma membrane using PALM and pair correlation analysis. *Nat. Methods* **8**, 969–975 (2011).

106. Veatch, S. L. *et al.* Correlation Functions Quantify Super-Resolution Images and Estimate Apparent Clustering Due to Over-Counting. *PLOS ONE* **7**, e31457 (2012).

107. van Leeuwen, J. M. J., Groeneveld, J. & de Boer, J. New method for the calculation of the pair correlation function. I. *Physica* **25**, 792–808 (1959).

108. Bar-On, D. *et al.* Super-resolution Imaging Reveals the Internal Architecture of Nano-sized Syntaxin Clusters. *J. Biol. Chem.* **287**, 27158–27167 (2012).

109. Williamson, D. J. *et al.* Pre-existing clusters of the adaptor Lat do not participate in early T cell signaling events. *Nat. Immunol.* **12**, 655–662 (2011).

110. Razvag, Y. *et al.* T Cell Activation through Isolated Tight Contacts. *Cell Rep.* **29**, 3506-3521.e6 (2019).

111. Nieves, D. J. & Owen, D. M. Analysis methods for interrogating spatial organisation of single molecule localisation microscopy data. *Int. J. Biochem. Cell Biol.* **123**, 105749 (2020).

112. Feher, K., Halstead, J. M., Goyette, J. & Gaus, K. Can single molecule localization microscopy detect nanoclusters in T cells? *Curr. Opin. Chem. Biol.* **51**, 130–137 (2019).

113. Ester, M., Kriegel, H.-P., Sander, J. & Xu, X. *A Density-Based Algorithm for Discovering Clusters in Large Spatial Databases with Noise*. www.aaai.org (1996).

114. Pageon, S. V. *et al.* Functional role of T-cell receptor nanoclusters in signal initiation and antigen discrimination. *Proc. Natl. Acad. Sci.* **113**, E5454–E5463 (2016).

115. Pageon, S. V., Nicovich, P. R., Mollazade, M., Tabarin, T. & Gaus, K. Clus-DoC: A combined cluster detection and colocalization analysis for single-molecule localization microscopy data. *Mol. Biol. Cell* **27**, 3627–3636 (2016).

116. Nan, X. *et al.* Single-molecule superresolution imaging allows quantitative analysis of RAF multimer formation and signaling. *Proc. Natl. Acad. Sci. U. S. A.* **110**, 18519–18524 (2013).

117. Deschout, H., Shivanandan, A., Annibale, P., Scarselli, M. & Radenovic, A. Progress in quantitative single-molecule localization microscopy. *Histochem. Cell Biol.* **142**, 5–17 (2014).

118. Griffié, J. *et al.* A Bayesian cluster analysis method for single-molecule localization microscopy data. *Nat. Protoc.* **11**, 2499–2514 (2016).

119. Rubin-Delanchy, P. *et al.* Bayesian cluster identification in single-molecule localization microscopy data. *Nat. Methods* **12**, 1072–1076 (2015).

120. Pike, J. A. *et al.* Topological data analysis quantifies biological nano-structure from single molecule localization microscopy. *Bioinformatics* **36**, 1614–1621 (2020).

121. Wu, Y.-L., Tschanz, A., Krupnik, L. & Ries, J. Quantitative Data Analysis in Single-Molecule Localization Microscopy. *Trends Cell Biol.* **30**, 837–851 (2020).

122. Andronov, L. *et al.* 3DClusterViSu: 3D clustering analysis of super-resolution microscopy data by 3D Voronoi tessellations. *Bioinformatics* **34**, 3004–3012 (2018).

123. Khater, I. M., Nabi, I. R. & Hamarneh, G. A Review of Super-Resolution Single-Molecule Localization Microscopy Cluster Analysis and Quantification Methods. *Patterns* **1**, 100038–100038 (2020).

124. Dlasková, A. *et al.* 3D super-resolution microscopy reflects mitochondrial cristae alternations and mtDNA nucleoid size and distribution. *Biochim. Biophys. Acta BBA - Bioenerg.* **1859**, 829–844 (2018).

125. Andronov, L., Orlov, I., Lutz, Y., Vonesch, J.-L. & Klaholz, B. P. ClusterViSu, a method for clustering of protein complexes by Voronoi tessellation in super-resolution microscopy. *Sci. Rep.* **6**, 24084 (2016).

126. Levet, F. *et al.* SR-Tesseler: a method to segment and quantify localization-based super-resolution microscopy data. *Nat. Methods* **12**, 1065–1071 (2015).

127. Hadipour-Lakmehsari, S. *et al.* Nanoscale reorganization of sarcoplasmic reticulum in pressure-overload cardiac hypertrophy visualized by dSTORM. *Sci. Rep.* **9**, 7867 (2019).

128. Wu, J.-Q., McCormick, C. D. & Pollard, T. D. Chapter 9: Counting proteins in living cells by quantitative fluorescence microscopy with internal standards. *Methods Cell Biol.* **89**, 253–273 (2008).

129. Nichols, M. G. & Hallworth, R. The Single-Molecule Approach to Membrane Protein Stoichiometry. *Methods Mol. Biol. Clifton NJ* **1427**, 189–199 (2016).

130. Finan, K., Raulf, A. & Heilemann, M. A set of homo-oligomeric standards allows accurate protein counting. *Angew. Chem. Int. Ed Engl.* **54**, 12049–12052 (2015).

131. Murray, J. M. An icosahedral virus as a fluorescent calibration standard: a method for counting protein molecules in cells by fluorescence microscopy. *J. Microsc.* **267**, 193–213 (2017).

132. Ulbrich, M. H. & Isacoff, E. Y. Subunit counting in membrane-bound proteins. *Nat. Methods* **4**, 319–321 (2007).

133. Gru$\upbeta$mayer, K. S., Yserentant, K. & Herten, D.-P. Photons in - numbers out: perspectives in quantitative fluorescence microscopy for in situ protein counting. *Methods Appl. Fluoresc.* **7**, 012003 (2019).

134. Bryan, J. S., Sgouralis, I. & Pressé, S. *Enumerating High Numbers of Fluorophores from Photobleaching Experiments: a Bayesian Nonparametrics Approach.* 2020.09.28.317057 https://www.biorxiv.org/content/10.1101/2020.09.28.317057v1 (2020) doi:10.1101/2020.09.28.317057.

135. Garry, J., Li, Y., Shew, B., Gradinaru, C. C. & Rutenberg, A. D. Bayesian counting of photobleaching steps with physical priors. *J. Chem. Phys.* **152**, 024110 (2020).

136. Hummert, J., Yserentant, K., Fink, T., Euchner, J. & Herten, D.-P. *Photobleaching step analysis for robust determination of protein complex stoichiometries.* 2020.08.26.268086 https://www.biorxiv.org/content/10.1101/2020.08.26.268086v1 (2020) doi:10.1101/2020.08.26.268086.

137. Xu, J. *et al.* Automated Stoichiometry Analysis of Single-Molecule Fluorescence Imaging Traces via Deep Learning. *J. Am. Chem. Soc.* **141**, 6976–6985 (2019).

138. Durisic, N., Laparra-Cuervo, L., Sandoval-Álvarez, Á., Borbely, J. S. & Lakadamyali, M. Single-molecule evaluation of fluorescent protein photoactivation efficiency using an in vivo nanotemplate. *Nat. Methods* **11**, 156–162 (2014).

139. Platzer, R. *et al.* Unscrambling fluorophore blinking for comprehensive cluster detection via photoactivated localization microscopy. *Nat. Commun.* **11**, 4993 (2020).

140. Hummert, J., Tashev, S. A. & Herten, D.-P. An update on molecular counting in fluorescence microscopy. *Int. J. Biochem. Cell Biol.* **135**, 105978 (2021).

141. Schmied, J. J. *et al.* DNA origami–based standards for quantitative fluorescence microscopy. *Nat. Protoc.* **9**, 1367–1391 (2014).

142. Scheckenbach, M., Bauer, J., Zähringer, J., Selbach, F. & Tinnefeld, P. DNA origami nanorulers and emerging reference structures. *APL Mater.* **8**, 110902 (2020).

143. Zanacchi, F. C. *et al.* A DNA origami platform for quantifying protein copy number in super-resolution. *Nat. Methods* **14**, 789–792 (2017).

144. Zanacchi, F. C. *et al.* DNA Origami offers a versatile method for quantifying protein copy-number in super-resolution. *Nat. Methods* **14**, 789–792 (2017).

145. Sharonov, A. & Hochstrasser, R. M. Wide-field subdiffraction imaging by accumulated binding of diffusing probes. *Proc. Natl. Acad. Sci.* **103**, 18911–18916 (2006).

146. Jungmann, R. *et al.* Multiplexed 3D cellular super-resolution imaging with DNA-PAINT and Exchange-PAINT. *Nat. Methods* **11**, 313–318 (2014).

147. Jungmann, R. *et al.* Quantitative super-resolution imaging with qPAINT. *Nat. Methods* **13**, 439–442 (2016).

148. Lagache, T., Lang, G., Sauvonnet, N. & Olivo-Marin, J.-C. Analysis of the Spatial Organization of Molecules with Robust Statistics. *PLOS ONE* **8**, e80914 (2013).

149. Lagache, T., Sauvonnet, N., Danglot, L. & Olivo-Marin, J.-C. Statistical analysis of molecule colocalization in bioimaging. *Cytometry A* **87**, 568–579 (2015).

150. Getis, A. & Franklin, J. Second-Order Neighborhood Analysis of Mapped Point Patterns. *Ecology* **68**, 473–477 (1987).

151. Malkusch, S. *et al.* Coordinate-based colocalization analysis of single-molecule localization microscopy data. *Histochem. Cell Biol.* **137**, 1–10 (2012).

152. Rossy, J., Cohen, E., Gaus, K. & Owen, D. M. Method for co-cluster analysis in multichannel single-molecule localisation data. *Histochem. Cell Biol.* **141**, 605–612 (2014).

153. Levet, F. *et al.* A tessellation-based colocalization analysis approach for single-molecule localization microscopy. *Nat. Commun.* **10**, 2379 (2019).

154. Arista-Romero, M., Pujals, S. & Albertazzi, L. Towards a Quantitative Single Particle Characterization by Super Resolution Microscopy: From Virus Structures to Antivirals Design. *Front. Bioeng. Biotechnol.* **9**, (2021).

155. Chojnacki, J. & Eggeling, C. Super-resolution fluorescence microscopy studies of human immunodeficiency virus. *Retrovirology* **15**, 41–41 (2018).

156. Hemelaar, J. The origin and diversity of the HIV-1 pandemic. *Trends Mol. Med.* **18**, 182–192 (2012).

157. Saha, M. & Bhattacharya, S. A Brief Overview on HIV Infection, Diagnosis and Treatment. *Curr. Top. Med. Chem.* **19**, 2739–2741 (2019).

158. Weiss, R. A. How does HIV cause AIDS? *Science* **260**, 1273–1279 (1993).

159. Moore, J. P., Kitchen, S. G., Pugach, P. & Zack, J. A. The CCR5 and CXCR4 coreceptors--central to understanding the transmission and pathogenesis of human immunodeficiency virus type 1 infection. *AIDS Res. Hum. Retroviruses* **20**, 111–126 (2004).

160. Connor, R. I., Sheridan, K. E., Ceradini, D., Choe, S. & Landau, N. R. Change in Coreceptor Use Correlates with Disease Progression in HIV-1–Infected Individuals. *J. Exp. Med.* **185**, 621–628 (1997).

161. Orloff, G. M., Kennedy, M. S., Dawson, C. & McDougal, J. S. HIV-1 binding to CD4 T cells does not induce a Ca2+ influx or lead to activation of protein kinases. *AIDS Res. Hum. Retroviruses* **7**, 587–593 (1991).

162. Goodsell, D. S. Illustrations of the HIV life cycle. *Curr. Top. Microbiol. Immunol.* **389**, 243–252 (2015).

163. Brügger, B. *et al.* The HIV lipidome: A raft with an unusual composition. *Proc. Natl. Acad. Sci.* **103**, 2641–2646 (2006).

164. Carlson, L.-A. *et al.* Three-dimensional analysis of budding sites and released virus suggests a revised model for HIV-1 morphogenesis. *Cell Host Microbe* **4**, 592–599 (2008).

165. Chertova, E. *et al.* Envelope Glycoprotein Incorporation, Not Shedding of Surface Envelope Glycoprotein (gp120/SU), Is the Primary Determinant of SU Content of Purified Human Immunodeficiency Virus Type 1 and Simian Immunodeficiency Virus. *J. Virol.* **76**, 5315–5325 (2002).

166. Zhu, P. *et al.* Electron tomography analysis of envelope glycoprotein trimers on HIV and simian immunodeficiency virus virions. *Proc. Natl. Acad. Sci. U. S. A.* **100**, 15812–15817 (2003).

167. Chojnacki, J. *et al.* Maturation-Dependent HIV-1 Surface Protein Redistribution Revealed by Fluorescence Nanoscopy. *Science* (2012) doi:10.1126/science.1226359.

168. Turner, B. G. & Summers, M. F. Structural biology of HIV11Edited by P. E. Wright. *J. Mol. Biol.* **285**, 1–32 (1999).

169. Hartley, O., Klasse, P. J., Sattentau, Q. J. & Moore, J. P. V3: HIV's switch-hitter. *AIDS Res. Hum. Retroviruses* **21**, 171–189 (2005).

170. Chen, B. Molecular Mechanism of HIV-1 Entry. *Trends Microbiol.* **27**, 878–891 (2019).

171. Pancera, M. *et al.* Structure of HIV-1 gp120 with gp41-interactive region reveals layered envelope architecture and basis of conformational mobility. *Proc. Natl. Acad. Sci. U. S. A.* **107**, 1166–1171 (2010).

172. Merk, A. & Subramaniam, S. HIV-1 envelope glycoprotein structure. *Curr. Opin. Struct. Biol.* **23**, 268–276 (2013).

173. Dev, J. *et al.* Structural basis for membrane anchoring of HIV-1 envelope spike. *Science* **353**, 172–175 (2016).

174. Murakami, T. & Ono, A. HIV-1 entry: Duels between Env and host antiviral transmembrane proteins on the surface of virus particles. *Curr. Opin. Virol.* **50**, 59–68 (2021).

175. Johnson, W. E. & Desrosiers, R. C. Viral Persistence: HIV's Strategies of Immune System Evasion. *Annu. Rev. Med.* **53**, 499–518 (2002).

176. Wang, H. *et al.* Cryo-EM structure of a CD4-bound open HIV-1 envelope trimer reveals structural rearrangements of the gp120 V1V2 loop. *Proc. Natl. Acad. Sci.* **113**, E7151–E7158 (2016).

177. Ozorowski, G. *et al.* Open and closed structures reveal allostery and pliability in the HIV-1 envelope spike. *Nature* **547**, 360–363 (2017).

178. Julien, J.-P. *et al.* Crystal Structure of a Soluble Cleaved HIV-1 Envelope Trimer. *Science* (2013) doi:10.1126/science.1245625.

179. Liu, J., Bartesaghi, A., Borgnia, M. J., Sapiro, G. & Subramaniam, S. Molecular architecture of native HIV-1 gp120 trimers. *Nature* **455**, 109–113 (2008).

180. Harris, A. *et al.* Trimeric HIV-1 glycoprotein gp140 immunogens and native HIV-1 envelope glycoproteins display the same closed and open quaternary molecular architectures. *Proc. Natl. Acad. Sci.* **108**, 11440–11445 (2011).

181. Tran, E. E. H. *et al.* Structural Mechanism of Trimeric HIV-1 Envelope Glycoprotein Activation. *PLOS Pathog.* **8**, e1002797 (2012).

182. Lee, J. H., Ozorowski, G. & Ward, A. B. Cryo-EM structure of a native, fully glycosylated, cleaved HIV-1 envelope trimer. *Science* (2016) doi:10.1126/science.aad2450.

183. Lee, B., Sharron, M., Montaner, L. J., Weissman, D. & Doms, R. W. Quantification of CD4, CCR5, and CXCR4 levels on lymphocyte subsets, dendritic cells, and differentially conditioned monocyte-derived macrophages. *Proc. Natl. Acad. Sci. U. S. A.* **96**, 5215–5220 (1999).

184. Viard, M. *et al.* Role of Cholesterol in Human Immunodeficiency Virus Type 1 Envelope Protein-Mediated Fusion with Host Cells. *J. Virol.* **76**, 11584–11595 (2002).

185. Maddon, P. J. *et al.* The T4 gene encodes the AIDS virus receptor and is expressed in the immune system and the brain. *Cell* **47**, 333–348 (1986).

186. Ryu, S.-E. *et al.* Crystal structure of an HIV-binding recombinant fragment of human CD4. *Nature* **348**, 419–426 (1990).

187. Lasky, L. A. *et al.* Delineation of a region of the human immunodeficiency virus type 1 gp120 glycoprotein critical for interaction with the CD4 receptor. *Cell* **50**, 975–985 (1987).

188. Moebius, U. *et al.* Human immunodeficiency virus gp120 binding C'C" ridge of CD4 domain 1 is also involved in interaction with class II major histocompatibility complex molecules. *Proc. Natl. Acad. Sci. U. S. A.* **89**, 12008–12012 (1992).

189. Arthos, J. *et al.* Identification of the residues in human CD4 critical for the binding of HIV. *Cell* **57**, 469–481 (1989).

190. Kwong, P. D. *et al.* Molecular characteristics of recombinant human CD4 as deduced from polymorphic crystals. *Proc. Natl. Acad. Sci. U. S. A.* **87**, 6423–6427 (1990).

191. Pelchen-Matthews, A., Armes, J. E., Griffiths, G. & Marsh, M. Differential endocytosis of CD4 in lymphocytic and nonlymphocytic cells. *J. Exp. Med.* **173**, 575–587 (1991).

192. Roh, K. H., Lillemeier, B. F., Wang, F. & Davis, M. M. The coreceptor CD4 is expressed in distinct nanoclusters and does not colocalize with T-cell receptor and active protein tyrosine kinase p56lck. *Proc. Natl. Acad. Sci. U. S. A.* **112**, E1604–E1613 (2015).

193. Černý, J., Stockinger, H. & Hořejší, V. Noncovalent associations of T lymphocyte surface proteins. *Eur. J. Immunol.* **26**, 2335–2343 (1996).

194. Parolini, I., Sargiacomo, M., Lisanti, M. & Peschle, C. Signal transduction and glycophosphatidylinositol-linked proteins (lyn, lck, CD4, CD45, G proteins, and CD55) selectively localize in Triton- insoluble plasma membrane domains of human leukemic cell lines and normal granulocytes. *Blood* **87**, 3783–3794 (1996).

195. Parolini, I. *et al.* Phorbol Ester-induced Disruption of the CD4-Lck Complex Occurs within a Detergent-resistant Microdomain of the Plasma Membrane: INVOLVEMENT OF THE TRANSLOCATION OF ACTIVATED PROTEIN KINASE C ISOFORMS *. *J. Biol. Chem.* **274**, 14176–14187 (1999).

196. König, R., Shen, X. & Germain, R. N. Involvement of both major histocompatibility complex class II alpha and beta chains in CD4 function indicates a role for ordered oligomerization in T cell activation. *J. Exp. Med.* **182**, 779–787 (1995).

197. Sakihama, T., Smolyar, A. & Reinherz, E. L. Oligomerization of CD4 is required for stable binding to class II major histocompatibility complex proteins but not for interaction with human immunodeficiency virus gp120. *Proc. Natl. Acad. Sci. U. S. A.* **92**, 6444–6448 (1995).

198. Lynch, G. W., Sloane, A. J., Raso, V., Lai, A. & Cunningham, A. L. Direct evidence for native CD4 oligomers in lymphoid and monocytoid cells. *Eur. J. Immunol.* **29**, 2590–2602 (1999).

199. Matthias, L. J., Azimi, I., Tabrett, C. A. & Hogg, P. J. Reduced Monomeric CD4 Is the Preferred Receptor for HIV. *J. Biol. Chem.* **285**, 40793–40799 (2010).

200. Cerutti, N., Killick, M., Jugnarain, V., Papathanasopoulos, M. & Capovilla, A. Disulfide Reduction in CD4 Domain 1 or 2 Is Essential for Interaction with HIV Glycoprotein 120 (gp120), which Impairs Thioredoxin-driven CD4 Dimerization *. *J. Biol. Chem.* **289**, 10455–10465 (2014).

201. Matthias, L. J. *et al.* Disulfide exchange in domain 2 of CD4 is required for entry of HIV-1. *Nat. Immunol.* **3**, 727–732 (2002).

202. Kwong, P. D. *et al.* Structure of an HIV gp120 envelope glycoprotein in complex with the CD4 receptor and a neutralizing human antibody. *Nature* **393**, 648–659 (1998).

203. Chen, B. *et al.* Structure of an unliganded simian immunodeficiency virus gp120 core. *Nature* **433**, 834–841 (2005).

204. Chan, D. C., Fass, D., Berger, J. M. & Kim, P. S. Core structure of gp41 from the HIV envelope glycoprotein. *Cell* **89**, 263–273 (1997).

205. Weissenhorn, W., Dessen, A., Harrison, S. C., Skehel, J. J. & Wiley, D. C. Atomic structure of the ectodomain from HIV-1 gp41. *Nature* **387**, 426–430 (1997).

206. Melikyan, G. B. Common principles and intermediates of viral protein-mediated fusion: the HIV-1 paradigm. *Retrovirology* **5**, 111 (2008).

207. Su, X., Wang, Q., Wen, Y., Jiang, S. & Lu, L. Protein- and Peptide-Based Virus Inactivators: Inactivating Viruses Before Their Entry Into Cells. *Front. Microbiol.* **11**, 1063 (2020).

208. Sougrat, R. *et al.* Electron Tomography of the Contact between T Cells and SIV/HIV-1: Implications for Viral Entry. *PLOS Pathog.* **3**, e63 (2007).

209. Pereira, C. F., Rossy, J., Owen, D. M., Mak, J. & Gaus, K. HIV taken by STORM: Super-resolution fluorescence microscopy of a viral infection. *Virol. J.* **9**, 84 (2012).

210. Pham, S. *et al.* Cryo-electron microscopy and single molecule fluorescent microscopy detect CD4 receptor induced HIV size expansion prior to cell entry. *Virology* **486**, 121–133 (2015).

211. Iliopoulou, M. *et al.* A dynamic three-step mechanism drives the HIV-1 pre-fusion reaction. *Nat. Struct. Mol. Biol.* **25**, 814–822 (2018).

212. Rizzuto, C. D. *et al.* A conserved HIV gp120 glycoprotein structure involved in chemokine receptor binding. *Science* **280**, 1949–1953 (1998).

213. Huang, C. *et al.* Structures of the CCR5 N Terminus and of a Tyrosine-Sulfated Antibody with HIV-1 gp120 and CD4. *Science* (2007) doi:10.1126/science.1145373.

214. Liu, Q. *et al.* Quaternary contact in the initial interaction of CD4 with the HIV-1 envelope trimer. *Nat. Struct. Mol. Biol.* **24**, 370–378 (2017).

215. Ma, X. *et al.* HIV-1 Env trimer opens through an asymmetric intermediate in which individual protomers adopt distinct conformations. *eLife* **7**, e34271 (2018).

216. Campbell, S. M., Crowe, S. M. & Mak, J. Virion-associated cholesterol is critical for the maintenance of HIV-1 structure and infectivity. *AIDS* **16**, 2253–2261 (2002).

217. Guyader, M., Kiyokawa, E., Abrami, L., Turelli, P. & Trono, D. Role for Human Immunodeficiency Virus Type 1 Membrane Cholesterol in Viral Internalization. *J. Virol.* (2002) doi:10.1128/JVI.76.20.10356-10364.2002.

218. Ablan, S. *et al.* The role of cholesterol and sphingolipids in chemokine receptor function and HIV-1 envelope glycoprotein-mediated fusion. *Virol. J.* **3**, 104 (2006).

219. Yi, L., Fang, J., Isik, N., Chim, J. & Jin, T. HIV gp120-induced interaction between CD4 and CCR5 requires cholesterol-rich microenvironments revealed by live cell fluorescence resonance energy transfer imaging. *J. Biol. Chem.* **281**, 35446–35453 (2006).

220. Campbell, S. M., Crowe, S. M. & Mak, J. Lipid rafts and HIV-1: from viral entry to assembly of progeny virions. *J. Clin. Virol.* **22**, 217–227 (2001).

221. Jacobson, K., Mouritsen, O. G. & Anderson, R. G. W. Lipid rafts: at a crossroad between cell biology and physics. *Nat. Cell Biol.* **9**, 7–14 (2007).

222. Yang, S.-T. *et al.* HIV virions sense plasma membrane heterogeneity for cell entry. *Sci. Adv.* (2017) doi:10.1126/sciadv.1700338.

223. Layne, S. P., Merges, M. J., Dembo, M., Spouge, J. L. & Nara, P. L. HIV requires multiple gp120 molecules for CD4-mediated infection. *Nature* **346**, 277–279 (1990).

224. Ovesný, M., Křížek, P., Borkovec, J., Švindrych, Z. & Hagen, G. M. ThunderSTORM: A comprehensive ImageJ plug-in for PALM and STORM data analysis and super-resolution imaging. *Bioinformatics* **30**, 2389–2390 (2014).

225. Schindelin, J. *et al.* Fiji: An open-source platform for biological-image analysis. *Nat. Methods* **9**, 676–682 (2012).

226. Pageon, S. V., Nicovich, P. R., Mollazade, M., Tabarin, T. & Gaus, K. Clus-DoC: A combined cluster detection and colocalization analysis for single-molecule localization microscopy data. *Mol. Biol. Cell* **27**, 3627–3636 (2016).

227. Sieben, C., Sezgin, E., Eggeling, C. & Manley, S. Influenza A viruses use multivalent sialic acid clusters for cell binding and receptor activation. *PLOS Pathog.* **16**, e1008656–e1008656 (2020).

228. Sahl, S. J., Hell, S. W. & Jakobs, S. Fluorescence nanoscopy in cell biology. *Nat. Rev. Mol. Cell Biol.* **18**, 685–701 (2017).

229. Bunnell, S. C. *et al.* T cell receptor ligation induces the formation of dynamically regulated signaling assemblies. *J. Cell Biol.* **158**, 1263–1275 (2002).

230. Kumar, R. *et al.* Increased sensitivity of antigen-experienced T cells through the enrichment of oligomeric T cell receptor complexes. *Immunity* **35**, 375–387 (2011).

231. Schamel, W. W. A. *et al.* Coexistence of multivalent and monovalent TCRs explains high sensitivity and wide range of response. *J. Exp. Med.* **202**, 493–503 (2005).

232. James, J. R. *et al.* Single-molecule level analysis of the subunit composition of the T cell receptor on live T cells. *Proc. Natl. Acad. Sci. U. S. A.* **104**, 17662–17667 (2007).

233. Zhang, Y. *et al.* Quantitating morphological changes in biological samples during scanning electron microscopy sample preparation with correlative super-resolution microscopy. *PLOS ONE* **12**, e0176839 (2017).

234. Small, J. V. Organization of actin in the leading edge of cultured cells: influence of osmium tetroxide and dehydration on the ultrastructure of actin meshworks. *J. Cell Biol.* **91**, 695–705 (1981).

235. Tanaka, K. A. K. *et al.* Membrane molecules mobile even after chemical fixation. *Nat. Methods* **7**, 865–866 (2010).

236. Dempsey, G. T. Chapter 24 - A User's Guide to Localization-Based Super-Resolution Fluorescence Imaging. in *Methods in Cell Biology* (eds. Sluder, G. & Wolf, D. E.) vol. 114 561–592 (Academic Press, 2013).

237. Fujiwara, K. Techniques for localizing contractile proteins with fluorescent antibodies. *Curr. Top. Dev. Biol.* **14**, 271–296 (1980).

238. Robinson, R. W. & Snyder, J. A. An innovative fixative for cytoskeletal components allows high resolution in colocalization studies using immunofluorescence techniques. *Histochem. Cell Biol.* **122**, 1–5 (2004).

239. Leyton-Puig, D. *et al.* PFA fixation enables artifact-free super-resolution imaging of the actin cytoskeleton and associated proteins. *Biol. Open* **5**, 1001–1009 (2016).

240. Tagliaferro, P., Tandler, C. J., Ramos, A. J., Pecci Saavedra, J. & Brusco, A. Immunofluorescence and glutaraldehyde fixation. A new procedure based on the Schiff-quenching method. *J. Neurosci. Methods* **77**, 191–197 (1997).

241. Whelan, D. R. & Bell, T. D. M. Image artifacts in Single Molecule Localization Microscopy: why optimization of sample preparation protocols matters. *Sci. Rep.* **5**, 7924 (2015).

242. Stanly, T. A. *et al.* Critical importance of appropriate fixation conditions for faithful imaging of receptor microclusters. *Biol. Open* **5**, 1343–1350 (2016).

243. Heuser, J. E. & Kirschner, M. W. Filament organization revealed in platinum replicas of freeze-dried cytoskeletons. *J. Cell Biol.* **86**, 212–234 (1980).

244. Pereira, P. M. *et al.* Fix Your Membrane Receptor Imaging: Actin Cytoskeleton and CD4 Membrane Organization Disruption by Chemical Fixation. *Front. Immunol.* **10**, 675–675 (2019).

245. Oliver, C. & Jamur, M. C. Immunocytochemical methods and protocols. *Methods Mol. Biol. Clifton NJ* **588**, iv–v (2010).

246. Lehmann, M. *et al.* Quantitative Multicolor Super-Resolution Microscopy Reveals Tetherin HIV-1 Interaction. *PLoS Pathog.* **7**, e1002456 (2011).

247. Bittel, A. M. *et al.* Methodology for Quantitative Characterization of Fluorophore Photoswitching to Predict Superresolution Microscopy Image Quality. *Sci. Rep.* **6**, 29687 (2016).

248. Peters, R. *et al.* Development of 2-colour and 3D SMLM data analysis methods for fibrous spatial point patterns. *J. Phys. Appl. Phys.* **52**, 014005 (2018).

249. Rubin-Delanchy, P. *et al.* Bayesian cluster identification in single-molecule localization microscopy data. *Nat. Methods* **12**, 1072–1076 (2015).

250. Griffié, J., Boelen, L., Burn, G., Cope, A. P. & Owen, D. M. Topographic prominence as a method for cluster identification in single-molecule localisation data. *J. Biophotonics* **8**, 925–934 (2015).

251. Pageon, S. V. *et al.* Functional role of T-cell receptor nanoclusters in signal initiation and antigen discrimination. *Proc. Natl. Acad. Sci. U. S. A.* **113**, E5454–E5463 (2016).

252. Peters, R., Griffié, J., Burn, G. L., Williamson, D. J. & Owen, D. M. Quantitative fibre analysis of single-molecule localization microscopy data. *Sci. Rep.* **8**, 10418 (2018).

253. Hu, Y. S., Cang, H. & Lillemeier, B. F. Superresolution imaging reveals nanometer- and micrometer-scale spatial distributions of T-cell receptors in lymph nodes. *Proc. Natl. Acad. Sci. U. S. A.* **113**, 7201–7206 (2016).

254. Patel, L., Williamson, D., Owen, D. M. & Cohen, E. A. K. Blinking statistics and molecular counting in direct stochastic reconstruction microscopy (dSTORM). *Bioinformatics* (2021) doi:10.1093/bioinformatics/btab136.

255. Patel, L. *et al.* A hidden Markov model approach to characterizing the photo-switching behavior of fluorophores. *Ann. Appl. Stat.* **13**, 1397–1429 (2019).

256. Bock, H. *et al.* Two-color far-field fluorescence nanoscopy based on photoswitchable emitters. *Appl. Phys. B* **88**, 161–165 (2007).

257. Linde, S. van de *et al.* Multicolor photoswitching microscopy for subdiffraction-resolution fluorescence imaging. *Photochem. Photobiol. Sci.* **8**, 465–469 (2009).

258. Niekamp, S. *et al.* High accuracy measurements of nanometer-scale distances between fluorophores at the single-molecule level. *bioRxiv* 234740 (2018) doi:10.1101/234740.

259. Laine, R. F. *et al.* NanoJ: a high-performance open-source super-resolution microscopy toolbox. *J. Phys. Appl. Phys.* **52**, 163001 (2019).

260. Ioannides, C. G., Freedman, R. S. & Platsoucas, C. D. OKT4 monoclonal antibody-induced activation of an autoreactive T-cell clone. *Cell. Immunol.* **123**, 244–252 (1989).

261. Schindelin, J. *et al.* Fiji: An open-source platform for biological-image analysis. *Nat. Methods* **9**, 676–682 (2012).

262. Grewe, C., Beck, A. & Gelderblom, H. R. HIV: early virus-cell interactions. *J. Acquir. Immune Defic. Syndr.* **3**, 965–974 (1990).

263. Jones, D. M. & Padilla-Parra, S. Imaging real-time HIV-1 virion fusion with FRET-based biosensors. *Sci. Rep.* **5**, 13449 (2015).

264. Koch, P. *et al.* Visualizing fusion of pseudotyped HIV-1 particles in real time by live cell microscopy. *Retrovirology* **6**, 84 (2009).

265. Markosyan, R. M., Cohen, F. S. & Melikyan, G. B. Time-resolved imaging of HIV-1 Env-mediated lipid and content mixing between a single virion and cell membrane. *Mol. Biol. Cell* **16**, 5502–5513 (2005).

266. Singer, I. I. *et al.* CCR5, CXCR4, and CD4 Are Clustered and Closely Apposed on Microvilli of Human Macrophages and T Cells. *J. Virol.* **75**, 3779–3790 (2001).

267. Foti, M., Phelouzat, M.-A., Holm, Å., Rasmusson, B. J. & Carpentier, J.-L. p56Lck anchors CD4 to distinct microdomains on microvilli. *Proc. Natl. Acad. Sci.* **99**, 2008–2013 (2002).

268. Mazia, D., Schatten, G. & Sale, W. Adhesion of cells to surfaces coated with polylysine: Applications to electron microscopy. *J. Cell Biol.* **66**, 198–200 (1975).

269. Groves, J. T. & Dustin, M. L. Supported planar bilayers in studies on immune cell adhesion and communication. *J. Immunol. Methods* **278**, 19–32 (2003).

270. Santos, A. M. *et al.* Capturing resting T cells: The perils of PLL correspondence. *Nat. Immunol.* **19**, 203–205 (2018).

271. Nieves, D. J. *et al. A framework for evaluating the performance of SMLM cluster analysis algorithms.* http://biorxiv.org/lookup/doi/10.1101/2021.06.19.449098 (2021) doi:10.1101/2021.06.19.449098.

272. Poncelet, P. *et al.* Surface CD4 density remains constant on lymphocytes of HIV-infected patients in the progression of disease. *Res. Immunol.* **142**, 291–298 (1991).

273. Lynch, G. W. *et al.* Marked differences in the structures and protein associations of lymphocyte and monocyte CD4: Resolution of a novel CD4 isoform. *Immunol. Cell Biol.* **84**, 154–165 (2006).

274. Xiao, X. *et al.* Constitutive cell surface association between CD4 and CCR5. *Proc. Natl. Acad. Sci.* **96**, 7496–7501 (1999).

275. Baker, A. M. *et al.* CD4 interacts constitutively with multiple CCR5 at the plasma membrane of living cells: A fluorescence recovery after photobleaching at variable radii approach. *J. Biol. Chem.* **282**, 35163–35168 (2007).

276. Gaibelet, G. *et al.* CD4 and CCR5 Constitutively Interact at the Plasma Membrane of Living Cells: A CONFOCAL FLUORESCENCE RESONANCE ENERGY TRANSFER-BASED APPROACH*. *J. Biol. Chem.* **281**, 37921–37929 (2006).

277. Grove, J. *et al.* Flat clathrin lattices: stable features of the plasma membrane. *Mol. Biol. Cell* **25**, 3581–3594 (2014).

278. Dalgleish, A. G. *et al.* The CD4 (T4) antigen is an essential component of the receptor for the AIDS retrovirus. *Nature* **312**, 763–767 (1984).

279. Berger, E. A., Murphy, P. M. & Farber, J. M. Chemokine receptors as HIV-1 coreceptors: roles in viral entry, tropism, and disease. *Annu. Rev. Immunol.* **17**, 657–700 (1999).

280. Wilen, C. B., Tilton, J. C. & Doms, R. W. HIV: Cell binding and entry. *Cold Spring Harb. Perspect. Med.* **2**, (2012).

281. Gallaher, W. R. Detection of a fusion peptide sequence in the transmembrane protein of human immunodeficiency virus. *Cell* **50**, 327–328 (1987).

282. Gallaher, W. R., Ball, J. M., Garry, R. F., Griffin, M. C. & Montelaro, R. C. A General Model for the Transmembrane Proteins of HIV and Other Retroviruses. *AIDS Res. Hum. Retroviruses* **5**, 431–440 (1989).

283. Zhu, P. *et al.* Distribution and three-dimensional structure of AIDS virus envelope spikes. *Nature* **441**, 847–852 (2006).

284. Brandenberg, O. F., Magnus, C., Rusert, P., Regoes, R. R. & Trkola, A. Different Infectivity of HIV-1 Strains Is Linked to Number of Envelope Trimers Required for Entry. *PLoS Pathog.* **11**, e1004595–e1004595 (2015).

285. DeSantis, M. C., Kim, J. H., Song, H., Klasse, P. J. & Cheng, W. Quantitative Correlation between Infectivity and Gp120 Density on HIV-1 Virions Revealed by Optical Trapping Virometry*. *J. Biol. Chem.* **291**, 13088–13097 (2016).

286. Klasse, P. J. The molecular basis of HIV entry. *Cell. Microbiol.* **14**, 1183–1192 (2012).

287. Brandenberg, O. F., Magnus, C., Regoes, R. R. & Trkola, A. The HIV-1 Entry Process: A Stoichiometric View. *Trends Microbiol.* **23**, 763–774 (2015).

288. Klasse, P. J. Modeling how many envelope glycoprotein trimers per virion participate in human immunodeficiency virus infectivity and its neutralization by antibody. *Virology* **369**, 245–262 (2007).

289. Magnus, C., Rusert, P., Bonhoeffer, S., Trkola, A. & Regoes, R. R. Estimating the stoichiometry of human immunodeficiency virus entry. *J. Virol.* **83**, 1523–1531 (2009).

290. Chojnacki, J. *et al.* Maturation-dependent HIV-1 surface protein redistribution revealed by fluorescence nanoscopy. *Science* **338**, 524–528 (2012).

291. Chojnacki, J. *et al.* Envelope glycoprotein mobility on HIV-1 particles depends on the virus maturation state. *Nat. Commun.* **8**, 545 (2017).

292. Jolly, C., Kashefi, K., Hollinshead, M. & Sattentau, Q. J. HIV-1 Cell to Cell Transfer across an Env-induced, Actin-dependent Synapse. *J. Exp. Med.* **199**, 283–293 (2004).

293. Jiménez-Baranda, S. *et al.* Filamin-A regulates actin-dependent clustering of HIV receptors. *Nat. Cell Biol.* **9**, 838–846 (2007).

294. Yoder, A. *et al.* HIV Envelope-CXCR4 Signaling Activates Cofilin to Overcome Cortical Actin Restriction in Resting CD4 T Cells. *Cell* **134**, 782–792 (2008).

295. Barrero-Villar, M. *et al.* Moesin is required for HIV-1-induced CD4-CXCR4 interaction, F-actin redistribution, membrane fusion and viral infection in lymphocytes. *J. Cell Sci.* **122**, 103–113 (2009).

296. Vorster, P. J. *et al.* LIM Kinase 1 Modulates Cortical Actin and CXCR4 Cycling and Is Activated by HIV-1 to Initiate Viral Infection*. *J. Biol. Chem.* **286**, 12554–12564 (2011).

297. Gordón-Alonso, M. *et al.* The PDZ-adaptor protein syntenin-1 regulates HIV-1 entry. *Mol. Biol. Cell* **23**, 2253–2263 (2012).

298. Gordón-Alonso, M. *et al.* Actin-binding Protein Drebrin Regulates HIV-1-triggered Actin Polymerization and Viral Infection*. *J. Biol. Chem.* **288**, 28382–28397 (2013).

299. García-Expósito, L. *et al.* Gelsolin activity controls efficient early HIV-1 infection. *Retrovirology* **10**, 39–39 (2013).

300. Herold, N. *et al.* HIV-1 Entry in SupT1-R5, CEM-ss, and Primary CD4+ T Cells Occurs at the Plasma Membrane and Does Not Require Endocytosis. *J. Virol.* **88**, 13956–13970 (2014).

301. Pontow, S. E., Heyden, N. V., Wei, S. & Ratner, L. Actin Cytoskeletal Reorganizations and Coreceptor-Mediated Activation of Rac during Human Immunodeficiency Virus-Induced Cell Fusion. *J. Virol.* **78**, 7138–7147 (2004).

302. Martin, N. *et al.* Virological Synapse-Mediated Spread of Human Immunodeficiency Virus Type 1 between T Cells Is Sensitive to Entry Inhibition. *J. Virol.* **84**, 3516–3527 (2010).

303. Frey, S. *et al.* Temperature dependence of cell-cell fusion induced by the envelope glycoprotein of human immunodeficiency virus type 1. *J. Virol.* **69**, 1462–1472 (1995).

304. Henderson, H. I. & Hope, T. J. The temperature arrested intermediate of virus-cell fusion is a functional step in HIV infection. *Virol. J.* **3**, 1–7 (2006).

305. Melikyan, G. B., Markosyan, R. M., Roth, M. G. & Cohen, F. S. A Point Mutation in the Transmembrane Domain of the Hemagglutinin of Influenza Virus Stabilizes a Hemifusion Intermediate That Can Transit to Fusion. *Mol. Biol. Cell* **11**, 3765–3775 (2000).

306. Llorente García, I. & Marsh, M. A biophysical perspective on receptor-mediated virus entry with a focus on HIV. *Biochim. Biophys. Acta - Biomembr.* **1862**, 183158–183158 (2020).

307. Klasse, P. J. *et al.* CD4-Chemokine Receptor Hybrids in Human Immunodeficiency Virus Type 1 Infection. *J. Virol.* **73**, 7453–7466 (1999).

308. Ito, Y. *et al.* Number of infection events per cell during HIV-1 cell-free infection. *Sci. Rep.* **7**, 6559 (2017).

309. Brégnard, C., Pacini, G., Danos, O. & Basmaciogullari, S. Suboptimal Provirus Expression Explains Apparent Nonrandom Cell Coinfection with HIV-1. *J. Virol.* **86**, 8810–8820 (2012).

310. Jung, A. *et al.* Multiply infected spleen cells in HIV patients. *Nature* **418**, 144–144 (2002).

311. Dixit, N. M. & Perelson, A. S. Multiplicity of Human Immunodeficiency Virus Infections in Lymphoid Tissue. *J. Virol.* **78**, 8942–8945 (2004).

312. Dang, Q. *et al.* Nonrandom HIV-1 infection and double infection via direct and cell-mediated pathways. *Proc. Natl. Acad. Sci. U. S. A.* **101**, 632–637 (2004).

313. Arthos, J. *et al.* HIV-1 envelope protein binds to and signals through integrin α4β7, the gut mucosal homing receptor for peripheral T cells. *Nat. Immunol.* **9**, 301–309 (2008).

314. Cicala, C. *et al.* The integrin α4β7 forms a complex with cell-surface CD4 and defines a T-cell subset that is highly susceptible to infection by HIV-1. *Proc. Natl. Acad. Sci. U. S. A.* **106**, 20877–20882 (2009).

315. Saphire, A. C. S., Bobardt, M. D., Zhang, Z., David, G. & Gallay, P. A. Syndecans Serve as Attachment Receptors for Human Immunodeficiency Virus Type 1 on Macrophages. *J. Virol.* **75**, 9187–9200 (2001).

316. Geijtenbeek, T. B. H. *et al.* DC-SIGN, a dendritic cell-specific HIV-1-binding protein that enhances trans-infection of T cells. *Cell* **100**, 587–597 (2000).

317. Iyengar, S., Hildreth, J. E. K. & Schwartz, D. H. Actin-Dependent Receptor Colocalization Required for Human Immunodeficiency Virus Entry into Host Cells. *J. Virol.* **72**, 5251–5255 (1998).

318. Jong, Y.-J. I., Harmon, S. K. & O'Malley, K. L. GPCR signalling from within the cell. *Br. J. Pharmacol.* **175**, 4026–4035 (2018).

319. Lucera, M. B. *et al.* HIV signaling through CD4 and CCR5 activates Rho family GTPases that are required for optimal infection of primary CD4+ T cells. *Retrovirology* **14**, 4–4 (2017).

320. Amara, A. *et al.* G Protein-Dependent CCR5 Signaling Is Not Required for Efficient Infection of Primary T Lymphocytes and Macrophages by R5 Human Immunodeficiency Virus Type 1 Isolates. *J. Virol.* **77**, 2550–2558 (2003).

321. Veillette, A., Bookman, M. A., Horak, E. M. & Bolen, J. B. The CD4 and CD8 T cell surface antigens are associated with the internal membrane tyrosine-protein kinase p56lck. *Cell* **55**, 301–308 (1988).

322. Pelchen-Matthews, A., Boulet, I., Littman, D., Fagard, R. & Marsh, M. The protein tyrosine kinase p56lck inhibits CD4 endocytosis by preventing entry of CD4 into coated pits. *J. Cell Biol.* **117**, 279–290 (1992).

323. Schwarzenbacher, M. *et al.* Micropatterning for quantitative analysis of protein-protein interactions in living cells. *Nat. Methods* **5**, 1053–1060 (2008).

324. Vasiliver-Shamis, G., Cho, M. W., Hioe, C. E. & Dustin, M. L. Human Immunodeficiency Virus Type 1 Envelope gp120-Induced Partial T-Cell Receptor Signaling Creates an F-Actin-Depleted Zone in the Virological Synapse. *J. Virol.* **83**, 11341–11355 (2009).

325. Sharma, C. P. & Goldmann, W. H. Phosphorylation of actin-binding protein (ABP-280; filamin) by tyrosine kinase p56lck modulates actin filament cross-linking. *Cell Biol. Int.* **28**, 935–941 (2004).

326. Ballek, O. *et al.* TCR Triggering Induces the Formation of Lck–RACK1–Actinin-1 Multiprotein Network Affecting Lck Redistribution. *Front. Immunol.* **7**, (2016).

327. Filipp, D., Ballek, O. & Manning, J. Lck, Membrane Microdomains, and TCR Triggering Machinery: Defining the New Rules of Engagement. *Front. Immunol.* **3**, (2012).

328. Ostergaard, H. L., Lou, O., Arendt, C. W. & Berg, N. N. Paxillin Phosphorylation and Association with Lck and Pyk2 in Anti-CD3- or Anti-CD45-stimulated T Cells *. *J. Biol. Chem.* **273**, 5692–5696 (1998).

329. Chojnacki, J. *et al.* Envelope glycoprotein mobility on HIV-1 particles depends on the virus maturation state. *Nat. Commun.* **8**, (2017).

330. Chojnacki, J. & Eggeling, C. Super-resolution fluorescence microscopy studies of human immunodeficiency virus. *Retrovirology* **15**, 41–41 (2018).

331. Roy, N. H., Chan, J., Lambelé, M. & Thali, M. Clustering and Mobility of HIV-1 Env at Viral Assembly Sites Predict Its Propensity To Induce Cell-Cell Fusion. *J. Virol.* **87**, 7516–7525 (2013).

332. Sauter, M. M. *et al.* An internalization signal in the simian immunodeficiency virus transmembrane protein cytoplasmic domain modulates expression of envelope glycoproteins on the cell surface. *J. Cell Biol.* **132**, 795–811 (1996).

333. Pitcher, C., Höning, S., Fingerhut, A., Bowers, K. & Marsh, M. Cluster of differentiation antigen 4 (CD4) endocytosis and adaptor complex binding require activation of the CD4 endocytosis signal by serine phosphorylation. *Mol. Biol. Cell* **10**, 677–691 (1999).

334. Pelchen-Matthews, A., Parsons, I. J. & Marsh, M. Phorbol Ester-induced Downregulation of CD4 is a Multistep Process Involving Dissociation from p56 lck, Increased Association with Clathrin-coated Pits, and Altered Endosomal Sorting. *J. Exp. Med.* **178**, 1209–1222 (1993).

335. Dietrich, J., Kastrup, J., Nielsen, B. L., Ødum, N. & Geisler, C. Regulation and function of the CD3γ/DxxxLL motif: A binding site for adaptor protein-1 and adaptor protein-2 in vitro. *J. Cell Biol.* **138**, 271–281 (1997).

336. Platt, E. J., Wehrly, K., Kuhmann, S. E., Chesebro, B. & Kabat, D. Effects of CCR5 and CD4 cell surface concentrations on infections by macrophagetropic isolates of human immunodeficiency virus type 1. *J. Virol.* **72**, 2855–2864 (1998).

337. Reynes, J. *et al.* CD4+ T cell surface CCR5 density as a determining factor of virus load in persons infected with human immunodeficiency virus type 1. *J. Infect. Dis.* **181**, 927–932 (2000).

338. Structural organization of authentic, mature HIV-1 virions and cores. *EMBO J.* **22**, 1707–1715 (2003).

339. Pope, M. & Haase, A. T. Transmission, acute HIV-1 infection and the quest for strategies to prevent infection. *Nat. Med.* **9**, 847–852 (2003).

340. Poveda, E., Briz, V., Quiñones-Mateu, M. & Soriano, V. HIV tropism: diagnostic tools and implications for disease progression and treatment with entry inhibitors. *AIDS* **20**, 1359–1367 (2006).

341. Steffens, C. M. & Hope, T. J. Localization of CD4 and CCR5 in living cells. *J. Virol.* **77**, 4985–4991 (2003).

342. Steffens, C. M. & Hope, T. J. Mobility of the Human Immunodeficiency Virus (HIV) Receptor CD4 and Coreceptor CCR5 in Living Cells: Implications for HIV Fusion and Entry Events. *J. Virol.* **78**, 9573–9578 (2004).

343. Gautier, A. *et al.* An Engineered Protein Tag for Multiprotein Labeling in Living Cells. *Chem. Biol.* **15**, 128–136 (2008).

344. Keppler, A. *et al.* A general method for the covalent labeling of fusion proteins with small molecules in vivo. *Nat. Biotechnol.* **21**, 86–89 (2003).

345. Los, G. V. *et al.* HaloTag: A Novel Protein Labeling Technology for Cell Imaging and Protein Analysis. *ACS Chem. Biol.* **3**, 373–382 (2008).

346. Nieves, D. J. *et al.* tagPAINT: covalent labelling of genetically encoded protein tags for DNA-PAINT imaging. *R. Soc. Open Sci.* **6**, 191268.

347. Francis, A. C., Marin, M., Shi, J., Aiken, C. & Melikyan, G. B. Time-Resolved Imaging of Single HIV-1 Uncoating In Vitro and in Living Cells. *PLoS Pathog.* **12**, e1005709 (2016).

348. Yoo, S. *et al.* Molecular recognition in the HIV-1 capsid/cyclophilin A complex. *J. Mol. Biol.* **269**, 780–795 (1997).

349. Braaten, D., Ansari, H. & Luban, J. The hydrophobic pocket of cyclophilin is the binding site for the human immunodeficiency virus type 1 Gag polyprotein. *J. Virol.* **71**, 2107–2113 (1997).

350. Luban, J., Bossolt, K. L., Franke, E. K., Kalpana, G. V. & Goff, S. P. Human immunodeficiency virus type 1 Gag protein binds to cyclophilins A and B. *Cell* **73**, 1067–1078 (1993).

351. Javanbakht, H. *et al.* The Ability of Multimerized Cyclophilin A to Restrict Retrovirus Infection. *Virology* **367**, 19–29 (2007).

352. Francis, A. C. & Melikyan, G. B. Live-Cell Imaging of Early Steps of Single HIV-1 Infection. *Viruses* **10**, 275 (2018).

353. Andrews, N. L. *et al.* Actin restricts FcεRI diffusion and facilitates antigen-induced receptor immobilisation. *Nat. Cell Biol.* **10**, 955–963 (2008).

354. Hoffmann, M. *et al.* SARS-CoV-2 Cell Entry Depends on ACE2 and TMPRSS2 and Is Blocked by a Clinically Proven Protease Inhibitor. *Cell* **181**, 271-280.e8 (2020).

355. Murgolo, N. *et al.* SARS-CoV-2 tropism, entry, replication, and propagation: Considerations for drug discovery and development. *PLOS Pathog.* **17**, e1009225 (2021).

356. Wrapp, D. *et al.* Cryo-EM structure of the 2019-nCoV spike in the prefusion conformation. *Science* **367**, 1260–1263 (2020).

357. Yang, N. & Shen, H.-M. Targeting the Endocytic Pathway and Autophagy Process as a Novel Therapeutic Strategy in COVID-19. *Int. J. Biol. Sci.* **16**, 1724–1731 (2020).